STABILITY OF ION CHAINS IN A CRYOGENIC SURFACE-ELECTRODE ION TRAP

A Thesis
Presented to
The Academic Faculty

by

Grahame Vittorini

In Partial Fulfillment
of the Requirements for the Degree
Doctor of Philosophy in the
School of Physics

Georgia Institute of Technology
December 2013

STABILITY OF ION CHAINS IN A CRYOGENIC SURFACE-ELECTRODE ION TRAP

Approved by:

Professor Kenneth R. Brown, Advisor
Schools of Chemistry and Biochemistry, Computational Science and Engineering, and Physics
Georgia Institute of Technology

Professor Michael S. Chapman
School of Physics
Georgia Institute of Technology

Professor T. A. Brian Kennedy
School of Physics
Georgia Institute of Technology

Professor Alex Kuzmich
School of Physics
Georgia Institute of Technology

Prof. Andrew Zangwill
School of Physics
Georgia Institute of Technology

Date Approved: August 15, 2013

Oh, you know... strikes and gutters, ups and downs.

- The Dude, The Big Lebowski

ACKNOWLEDGEMENTS

There are many people to recognize but first and foremost is Ken Brown. He has been my mentor, friend, and rival all rolled into one. I appreciate the opportunity he gave me and everything he invested as well as his sincerity and empathy. I look forward to interacting with him for years to come.

Charlie Doret who taught me much about cryogenics, working with my hands, and performing experiments. His friendship and healthy board game collection were also greatly appreciated.

James Goeders who was a fantastic friend, commiserator, and labmate. I still sort of hate him for Oliver though.

Dick Slusher and later Alexa Harter who supported me throughout my graduate career and provided me with a fantastic environment to do experiments in.

Every member of the Quantum Information System group at GTRI but most importantly Jason Amini for his deep knowledge of everything related to ion trapping and his willingness to share, Curtis Volin for making sure the lab ran smoothly and we always had what we needed, and Kenton Brown for being unintentionally motivational.

All the members of Brown Lab both past and present. Specifically, Ricardo Viteri, the postdoc I did not truly appreciate until he was gone, Yatis Dodia for the verbal sparring, Craig Clark who taught me something about hard work, Yu Tomita for the Japanese lessons, True Merrill for his focus, Mauricio Gutiérrez for his corn rows (que me dice, mae), Chingiz Kabytayev for his quiet but sharp sense of humor, JB Khanyile for his trolling, and Rick Shu for keeping me on my toes. Also, all the poor, poor undergrads and first year grad students who I hope I have not traumatized too badly.

Ken Wright who has had to put up with me in Brown Lab, then GTRI, and soon at UMD. Sorry, man.

Aaron Buikema and Karl Burkhardt, undergraduates who taught me as much as I hope

I taught them.

The fantastic physics professors who have helped me along the way including Ken Cecire, Eric Christy, Anne Cox, Harry Ellis, Eduardo Fernandez, Brian Kennedy, Stephen Weppner, and Andrew Zangwill.

My parents for each teaching me how to live life in their own way. My American grandparents for fostering a love of learning and science. My English grandparents for doing the same thing from 3800 miles away while being my biggest cheerleaders and making Eckerd happen. The rest of my family and friends for everything.

Finally, that rascal Hayley Borck!

TABLE OF CONTENTS

LIST OF TABLES

LIST OF FIGURES

SUMMARY

Cold, trapped atomic ions have enabled the investigation of fundamental physics and generated a rich field of applications. Foremost among these is quantum computation which has recently driven the development of the sophisticated, scalable surface-electrode trap. Despite the many advantages of surface-electrode traps, the typically smaller ion-electrode distance, d, in these traps results in an increased ion heating rate ($\propto d^{-4}$) and a decreased trap well-depth ($\propto d^{-2}$). These shortcomings can be simultaneously addressed by installing the trap into a cryogenic environment. With this in mind, a closed-cycle, cryogenic ion trapping apparatus that maintains excellent vacuum, is highly modular, has increased optical access, and uses a simple vibration isolation system has been developed.

Single ions are trapped and used to characterize system properties such as the motion of the vibration isolation stage. In order to compare this system to a similar room temperature apparatus, the ion trapping lifetime and heating rate are determined. A single ion also serves as a sensitive electric field probe that is used to measure and compensate stray electric fields across the trap.

Due to the long dark ion lifetimes in this system, it is well-suited to probing the stability of small, linear ion crystals. Linear ion crystals of arbitrary length are built in an automated fashion using transport waveforms and the scaling of dark lifetime with ion number for $N \leq 6$ is investigated. These data are then used to consider the relevance of various loss channels.

CHAPTER I

INTRODUCTION

Trapped ion systems can be engineered to provide nearly perfect two-level quantum dynamics. Because of this, trapped ions sit at the forefront of quantum computation and simulation. Currently, meaningful quantum computation can only be done with $N \leq 6$ ions [1]. In order to scale up to larger qubit numbers as well as create advanced multi-ion interactions for quantum simulation, novel, high-spatial resolution electrode geometries are necessary. These requirements can be met by traps of the surface-electrode variety [2]. However, the reduced size of surface-electrode traps results in a smaller well-depth as well as an increased ion heating rate. Each of these issues has individual solutions yet both can be addressed by a cryogenic ion trap [3, 4]. This thesis details the creation and characterization of such a cryogenic surface-electrode ion trapping apparatus. Additionally, this system can be used to explore the scaling of ion dark lifetime with ion number in the small linear ion crystals known as ion chains. Before going further, a brief introduction to trapped ions, ion crystals and chains, surface-electrode traps, and cryogenics is in order.

1.1 Trapped Ions

The non-magnetic quadrupole mass filter, the basis for the Paul trap [5], was introduced in 1953 [6][1]. With little modification, it has been highly successful and has found such diverse applications as the guiding of charged particle beams and mass spectrometry [8]. Charged particles of appropriate mass-to-charge ratio experience stable oscillations due to the radio frequency (RF) quadrupole field and thus either pass through the mass filter unperturbed or can be guided. Particles outside this range have unstable trajectories and are lost due to collisions with the trap electrodes. With the addition of a static trapping voltage perpendicular to the plane of the quadrupole field, charged particles can be confined

[1] The Paul trap itself was also introduced by Paul and Steinwedel in their 1953 patent for the non-magnetic quadrupole mass filter. For more information, see Ref. [7].

in all three spatial dimensions [9].

Another variety of ion trap, known as the Penning trap, replaces the RF electric field with a magnetic field. Novel experiments such as the first laser cooled ions [10], storage of anti-protons and positrons for anti-hydrogen production [11], and the quantum simulation of 2D Ising interactions [12] have all been performed in Penning traps.

The development of ion trapping technology and techniques from the 1970s until the mid-1990s was largely driven by the desire for reduced uncertainty in spectroscopic and precision measurements such as frequency standards. First-order Doppler shifts are mitigated by trapping ions; however, the removal of Doppler broadening and second-order shifts due to micromotion requires cooling of a single ion to its motional ground state. This is possible by using Doppler [10] and resolved sideband laser cooling [13]. When multiple ions are trapped in a traditional 3D Paul trap, no single ion sits at the RF null and thus all ions experience increased micromotion and level shifts. The linear Paul trap was developed to address this issue by allowing the trapping of multiple ions along a linear RF null [14]. This geometry allows more ions to be trapped for a given Doppler shift magnitude resulting in decreased shot noise.

In 1982, quantum computation was introduced as well as the simulation of quantum systems by quantum systems [15]. In 1994, Shor's algorithm for factoring [16] was introduced and just a year later, a proposal for quantum computation with cold, trapped ions [17] followed. This spurred significant trap and technique development. The desire for increased two-qubit gate speeds ($\propto 1/d^2$) has resulted in significant progress in the miniaturization of traps.

The accomplishments of the ion trap community have resulted in the award of two Nobel prizes. Hans Dehmelt and Wolfgang Paul received a portion of the prize in 1989 "for the development of the ion trap technique" and half of the prize was awarded to David Wineland in 2012 "for ground-breaking experimental methods that enable measuring and manipulation of individual quantum systems." Trapped ions now stand at the forefront of quantum computation [18], quantum simulation [19], remote entanglement [20], and the field of frequency standards [21].

1.2 Crystals and Chains

Much can be gained from scaling up this exquisitely controllable quantum system to chains or large Coulomb crystals. Most obviously, an increase in fundamental quantum elements is beneficial for quantum computation [1] and simulation [19]. Furthermore, ion chains have been used to investigate entanglement of up to 14 ions in a single trap [22]. Increased ion numbers result in reduced shot noise and more sensitive detection of directly probed atomic levels [23, 24]. Such precision measurements have also been used to put an upper limit on the temporal variation of the fine structure constant [21].

It is possible to cool an entire ionic ensemble by only directly cooling a subset of ions. The remaining ions are sympathetically cooled via inter-ion Coulomb interactions [25–27]. Ions that lack closed-cycle cooling transitions can be co-trapped and both direct and indirect spectroscopy performed. Sympathetic cooling allows the generation of translationally cold and spatially confined molecular ions [27]. This has given birth to an entire field of cold quantum chemistry and enabled the creation of cold molecular ion sources [28], the investigation of cold chemical reactions [29, 30], and the testing of fundamental constant variations using ultracold molecules [31]. The field of precision measurement has also benefited from sympathetic cooling as it has enabled the development of Quantum Logic Spectroscopy [32] to sensitively probe ions that are technically difficult to laser cool or lack a suitable cooling cycle [33].

1.3 Surface-electrode Trap

Performing quantum mechanical calculations or simulations of an N-qubit system on a classical computer requires the storage of 2^N real numbers. Because of this exponential scaling, a quantum computer of even modest size, say N$\sim$100 qubits, outstrips the storage capacity of a classical computer [34]. However, the current cutting edge of quantum computation with trapped ions consists of the manipulation of a handful of ions in a laboratory setting [1, 18]. Due to the unfavorable scaling of gate speeds with ion number and spacing, a Coulomb crystal stored in a single trap is limited to tens of ions [35]. To reach the next order of magnitude, novel approaches such as the Quantum Charge Coupled Device

(QCCD) [36] and remote entanglement of qubits [37] must be utilized.

The QCCD, essentially a series of locally interconnected ion traps, requires multiple trapping regions, the ability to transport ions, and junctions between trapping regions. It is difficult to meet such requirements with micromachined, linear Paul traps. Instead, traps can be fabricated with a planar, surface-electrode geometry [2], enabling the use of traditional, repeatable microfabrication techniques to produce small, scalable traps with the novel, high spatial resolution electrode geometries necessary for ion transport [38, 39] and reordering [40, 41]. The mapping of the linear Paul trap to a surface-electrode geometry is possible through finite element analysis as well as analytical methods [42].

Despite these advantages, surface-electrode traps suffer from decreased well-depth and increased anomalous heating [4, 43] due to their reduced size. As the trap electrodes are now constrained to a plane, an ion can more easily escape perpendicular to the trap surface. The reduced well-depth compromises ion lifetime due to collisions with background gas molecules which transfer significant kinetic energy and may cause charge-exchange or chemical reactions [44]. Therefore it is paramount to achieve excellent vacuum. The use of high speed pumps near the ions, such as titanium sublimation pumps or non-evaporable getters, decreases the local pressure while the use of heavier ions reduces the effect of collisions. Anomalous heating, believed to be due to patch potentials on the trap electrodes [43] and a major source of decoherence during the execution of quantum gates, is also exacerbated in surface-electrode traps. More recent efforts have focused on improving surface quality through ablation with a high power Nd:YAG laser [45] and argon ion milling [46]; the former achieved a heating rate reduction of two, whereas the latter provided a two order-of-magnitude improvement.

1.4 Cryogenics

It has been recognized for some time that placing an ion trap into a cryogenic environment significantly reduces the background gas pressure mitigating most loss channels [3]. Cryogenics can also be leveraged to reduce ion trap heating rates [4]; typical reductions of one to two orders-of-magnitude have been observed [47, 48]. Even a relatively simple cryogenic ion

trapping apparatus should be superior to a room temperature system in these key areas.

There are many other vacuum-related advantages to a cryogenic system. In contrast to a room temperature system, high temperature baking of the vacuum chamber to remove adsorbates is not necessary. This reduces experimental downtime following trap installation or replacement. Cryopumping rates are sufficiently high that bulky, stock CF vacuum hardware is unnecessary to achieve ultra-high vacuum, simplifying chamber design and increasing customizability. Reduced outgassing at cryogenic temperatures permits the use of a wide range of materials not appropriate for use in room temperature ultra-high vacuum chambers.

For a surface-electrode trap containing a string of ions in a single potential well, a cryogenic environment is especially helpful. An increased number of ions means a larger collisional cross-section, larger Coulomb self-energy, and unfavorable scaling for many sources of ion heating. These issues are further compounded by the reduced well-depth and high secular frequencies of surface-electrode traps resulting in reduced ion lifetime with ion number. The reduction in background gas pressure and ion heating rate provided by a cryogenic environment should ease the investigation and characterization of such loss and may allow the identity of the primary loss channel to be determined.

1.5 Organization of the Thesis

This thesis describes the design, construction, and characterization of a cryogenic surface-electrode ion trapping system. This system is used to investigate dark lifetime scaling with ion number for linear chains with $N \leq 6$ ions. In Chapter 2, the design goals and implementation specifics for the cryogenic chamber are detailed. A few necessary experimental basics and the results of the characterization of the system with a single ion can be found in Chapter 3. Chapter 4 discusses the experimental framework necessary for chain experiments, ion heating and loss mechanisms, and dark lifetime scaling. Chapter 5 concludes this work.

CHAPTER II

THE APPARATUS

2.1 Cryogenesis

The core of a cryogenic system of any kind is the cryostat which generates the cold environment. In previous cryogenic ion trapping experiments, either a bath cryostat or closed-cycle cryocooler has been utilized [3, 4, 49–54][2]. Several alternative cryostat designs such as pumped He-4 systems, He-3 systems, and dilution refrigerators remain unutilized by ion trappers due to their reduced cooling power per dollar, additional complexity, and increased initial and operational costs. An excellent general reference for cryogenics can be found in Ref. [55].

2.1.1 Bath Cryostat

The simplest bath cryostat consists of a cryogenic dewar with a coldplate in direct contact with the dewar's liquid cryogen reservoir. An ion trap can be directly mounted to the coldplate and its temperature maintained through the evaporation of the cryogen. Typical atmospheric pressure cryogens are liquid nitrogen (LN_2) at 77 K and liquid helium-4 (LHe) at 4.2 K. More sophisticated systems will use LN_2 or superinsulation to thermally decouple the LHe reservoir from the laboratory environment.

Bath cryostats are typically characterized by the volume of liquid cryogen they can hold which determines the total heat that can be absorbed. However, as long as the reservoir contains liquid, the coldplate temperature will stay constant. The reservoir's volume is quite important as it determines the maximum amount of time the experiment can be kept cold. Since these systems contain no moving parts, they typically exhibit very little motion beyond that due to the boiling of the cryogen and environmental noise that may couple in at the narrow reservoir necks. This motion is usually $\sim$10 μm for a large cryostat but can

[2]With the exception of Ref. [4] in which the trap electrodes alone were cooled by a liquid nitrogen reservoir.

be reduced to sub-micron levels through the use of appropriate passive stabilization of the dewar [56]. Smaller cryostats have decreased vibration due to their compact size but hold less cryogens and thus experimental times are reduced.

The relatively simple design of bath cryostats significantly reduces the initial cost of the system; however, liquid cryogens must be purchased on a regular basis which adds significant operational costs. As of 2009, the cost of LHe, including overhead, for the Doyle group at Harvard was $10/liter [57] and the price has been increasing due to increased worldwide demand. With this lower limit on price in mind, the annual cost for LHe to run a typical bath cryostat ion trapping system as found in Ref. [50] at a 50% duty cycle would be ∼$7700, a significant portion of the initial cost.

2.1.2 Closed-cycle Cryocooler

A closed-cycle cryocooler utilizes a heat pump with high pressure helium-4 gas as the working fluid to generate cryogenic temperatures. A review of such systems can be found in Ref. [58]. Mechanical work is used to compress the working fluid and its subsequent isothermal expansion while in thermal contact with a coldplate provides the useful cooling power. There are two main types of cryocooler, those of the Gifford-McMahon (GM) design which contains an oscillating piston within the cold-head, and those of the Pulse Tube (PT) design which use pressure waves within the helium gas in lieu of moving parts. A typical system has two coldplates, one at 40-60 K with tens of watts of cooling power and one at ∼4 K with approximately 1 W or less of cooling power.

The term closed-cycle is used as helium is not lost from the system due to normal operation. For this reason, it is not necessary to purchase liquid cryogens or perform regular helium refills, significantly reducing the operational cost of such a system and almost completely eliminating down time.

Though these systems grant freedom from the liquid cryogen refill cycle, they have many demons of their own. First among these are intrinsic mechanical vibrations of tens of microns at the second stage originating from the helium compressor, the rotating valve between the cold-head and the compressor, and the flow of pressurized helium through

the cold-head itself. In addition, GM cryocoolers are subject to vibrations due to the piston within the cold-head. These vibrations usually occur at ∼1 Hz but can be reduced through the use of passive methods such as a helium exchange gas or active methods such as piezoactuators. The initial cost of closed-cycle systems is much higher due to their additional mechanical complexity and increases with the inclusion of a vibration-isolation system. Due to the lack of a cryogen reservoir, as the heat load on the coldplate increases the steady-state temperature of the coldplate will also increase which may be undesirable for some experiments.

2.2 Implementation

Only a handful of low temperature radio frequency (RF) Paul trapping systems have been built, in part because antithetical design considerations make most off-the-shelf cryostats poorly suited to ion trapping. Liquid helium based systems [3, 49–51] are expensive and impractical to operate due to the large heat loads contributed by oven-based ion sources, the multitude of electrical connections required for trap control, and the radio frequency trap drive. Closed-cycle systems [50, 52–54] eliminate cryogen use but have required expensive helium gas heat exchangers to reduce vibration to a level appropriate for high-fidelity gate operations and high-resolution imaging. Finally, laser cooling and trapped ion fluorescence collection require optical access from many directions and over large solid angles, complicating radiation shielding of the interior of any cryostat.

The apparatus detailed in this work attempts to address these conflicting requirements. The cryostat utilizes a standard commercial cryocooler and a simple vibration isolation assembly, providing increased cooling power at reduced cost relative to helium heat exchangers. The vacuum enclosure and 50 K radiation shield are highly modular, facilitating rapid turnaround (<24 hours from breaking vacuum to retrapping ions) while adding flexibility for future modifications to incorporate new trap designs or to change laser access. This design demonstrates that excellent vacuum can be achieved without any 4 K enclosure by differentially pumping the interior of the 50 K shield with charcoal getters. By eliminating this extra layer of shielding, laser access in the trap plane is improved and fluorescence

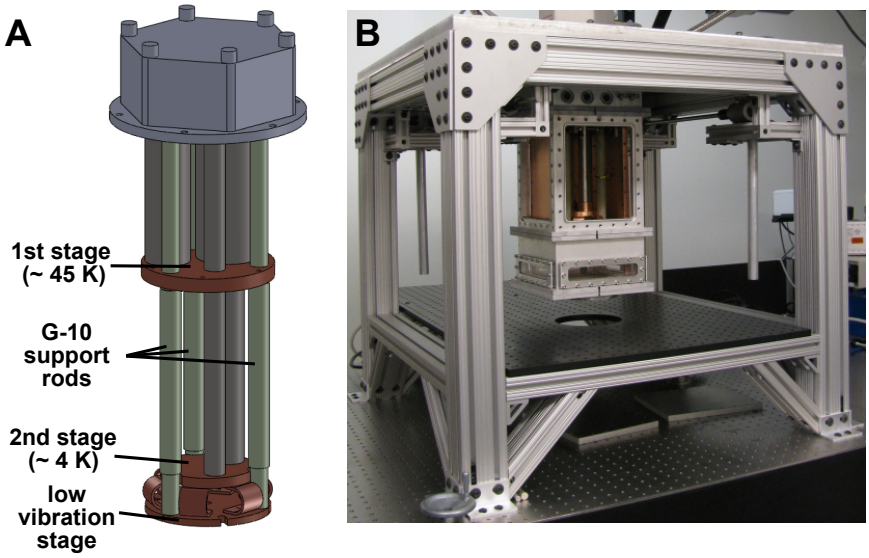

Figure 2.1: (a) The Cryomech PT407 cryocooler, with low vibration stage (remote motor and helium reservoirs not shown). Ion traps are anchored to the low-vibration stage, which is thermally linked to the 4 K second stage of the cryocooler. (b) The cryostat (with side panels removed) and superstructure.

collection over a large solid angle (NA 0.4) is possible without requiring in-vacuum optics.

The core of the experimental apparatus is a pulse-tube cryocooler (Cryomech PT407; Fig. 2.1a). This two-stage cryocooler is specified to provide 0.6 (22) W of cooling power at 4.2 (55) K and achieves a base temperature of 2.8 K with no applied heat load. The reduced vibration model of the PT407, for which the cold-head motor and helium reservoirs are mechanically isolated by flexible gas lines, is used. Additional vibration reduction features of the PT407 will be discussed later.

The cold-head is attached to an aluminum mounting plate which sits on a rigid superstructure made of extruded aluminium framing pieces (Fig. 2.1b). These framing pieces have a strong, hollow interior that can be filled with leadshot to decrease the resonant vibrational frequency. During operation the mounting plate is rigidly attached to the superstructure; however, four 100 kg capacity screwjacks (Joyce-Dayton WJ250) allow the mounting plate and cold-head to be raised by up to 30 cm to provide access to the sample stage during trap installation.

2.2.1 Vacuum Enclosure

Nearly all surfaces become effective cryopumps when cooled to cryogenic temperatures. Cryopumping may be enhanced by incorporating large surface area adsorbents (getters of activated charcoal, zeolites, or metal sinters) [55], leading to pumping speeds orders of magnitude larger than those achievable in room temperature vacuum systems. As outgassing is also negligible at low temperatures, differential pumping is adequate to achieve exceptional vacuum inside a cryostat even while relaxing the requirements on the vacuum enclosure.

With this in mind, the outer vacuum can (OVC) is designed to emphasize modularity, ease-of-assembly, and optical access. In lieu of the stainless steel ConFlat (CF) components used in some other systems [50, 52, 54], the OVC is aluminum with viton O-ring seals. This simplifies machining, reduces weight, and eliminates magnetic materials. The enclosure is composed of three sections (Fig. 2.2), each made from a length of extruded 20 $\times$ 20 cm square tubing with a 1.25 cm wall thickness (Metals Depot T38812). This square extrusion allows for more tightly-packed feedthroughs and larger windows than would be possible with a cylindrical geometry. To simplify construction, vacuum seals are formed via O-ring grooves cut directly into the end face of each section of extrusion, eliminating the need for any vacuum-tight welds. Flanges welded to the outside of each section at the top and bottom accomodate bolts for assembly.

The top section of the enclosure forms a short collar containing electrical and vacuum feedthroughs, while the bottom and middle sections may be removed to provide access to the ion trap and the region between the cryocooler stages, respectively. Interfaces between the sections are approximately matched to the heights of the first and second stages of the cryocooler, allowing piece-wise disassembly to access critical components without ever breaking electrical connections routed from the upper feedthrough collar. The design also incorporates removable side panels on all blank faces of the OVC. These panels afford rapid entry to the vacuum space and also increase modularity; a single panel may be changed or replaced (for example, to add additional electrical feedthroughs) without modifying other parts. Three such panels are mounted on the upper OVC, while the fourth (fixed) face contains electrical feedthroughs. Four large panels on the middle OVC open to the remainder

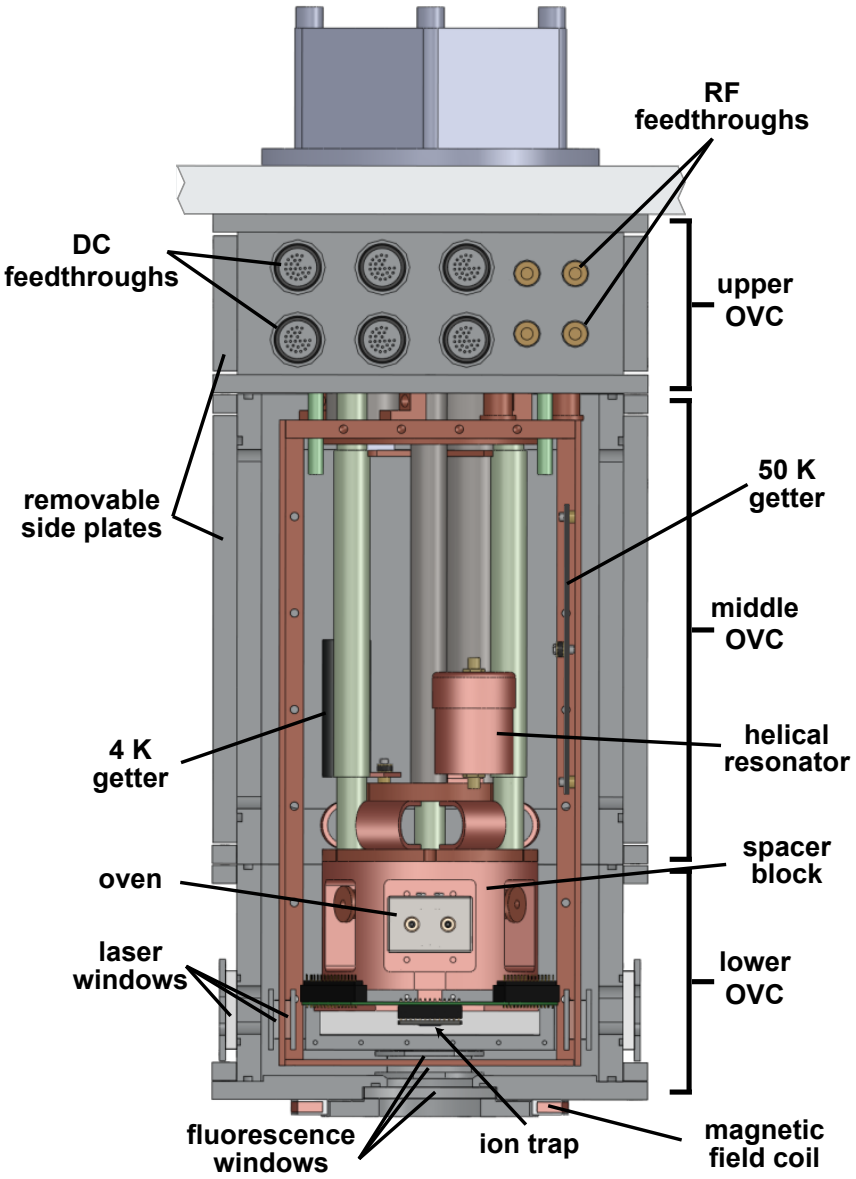

Figure 2.2: Section view of the cryostat including the cold-head, vacuum enclosure, radiation shield, and trap.

of the vacuum space.

Prior to cooling the system, an initial vacuum is created. The primary purpose of the initial vacuum is to avoid condensation of water vapor on the cold-head as well as excessive loading of the cryopumping surfaces with atmospheric gases. One of the upper OVC panels is made of type 304 stainless steel and has a KF40 and a KF25 half nipple welded in place. The pumping system is attached to the KF40 half nipple and consists of a manual KF-sealed angle valve, a pressure gauge (Lesker 910 Series), a residual gas analyzer (Stanford Research Systems RGA 100), a turbomolecular pump (Leybold Turbovac 50), and a rotary vane backing pump (Oerlikon Trivac D2,5 E). The gauge ensures adequate vacuum has been achieved to operate the residual gas analyzer which is used to helium leak test the vacuum enclosure. Another pressure gauge (Balzars PKR 251), to monitor the chamber pressure, and a pressure relief valve, to avoid overpressuring of the system during warmup, are attached to the KF25 half nipple.

2.2.2 Radiation Shield and Differential Pumping

Within the vacuum enclosure a radiation shield made of 3 mm thick copper is suspended from the aluminum mounting plate by four threaded G-10 rods. This layer is thermally anchored via stranded copper wire (Cooner Wire) to the first stage of the cryocooler, reaching a temperature of 50 K when cold. As with the vacuum enclosure, the heat shield is modular, consisting of side panels (OFHC, alloy C10100) mounted to corner posts (alloy C11000). Sub-panels on the front and back of the radiation shield are matched to the side ports of the middle OVC to further simplify interior access.

In addition to reducing the blackbody heat load, the radiation shield impedes gas flow between the room temperature vacuum enclosure and the cold interior, allowing the interior to be differentially cryopumped to ultra-high vacuum. To increase pumping speed three getters inside the shield are utilized - one anchored to the shield itself, a second on the 4 K stage of the cryocooler, and the third mounted to the fan-out PCB at $\sim$4 K. All three are made from activated charcoal (Calgon Carbon) epoxied to copper plates via Stycast 2850FT epoxy. Nichrome resistive heaters attached to the first two sorbs may be used to

speed the desorption of water during initial room temperature pumpout or to regenerate the getters when the system is cold. The heater mounted to the 4 K stage sorb is sufficient to raise the temperature of the sorb on the fan-out PCB.

2.2.3 Vibration Isolation

Despite the fact that all of the cryocooler's moving parts are mechanically divorced from the cold-head, residual vibration of the low temperature components remains due to the periodic motion of pressurized helium in the thin-walled stainless steel pulse tubes, as well as their differential thermal contraction. To reduce the motion of the ion trap, the trap is mechanically isolated from the 4 K stage of the cryocooler by mounting it to an auxiliary sample stage (Fig. 2.1a). This stage is formed from a copper mounting plate that is mechanically anchored to the stainless steel room temperature flange of the cold-head via three G-10 rods, thus rigidly attaching it to the stiff aluminum mounting plate and superstructure. The G10 rods are thermally anchored to the cryocooler's first stage by flexible copper braids, while six stacked copper foil bridges anchor the copper plate to the 4 K stage. A massive (~ 5 kg) cylindrical copper block (OFHC, alloy C10100) is anchored to the copper mounting plate. Its large size increases the thermal mass of the system to dampen temperature fluctuations while also reducing the amplitude of any remaining vibration; this spacer block may be modified or replaced to incorporate different trap designs.

2.2.4 Optical Access

Five windows located on the lower OVC provide optical access to the ion trap. Large rectangular windows (Esco Products) on the side faces of the OVC allow lasers to be aligned across the trap's surface. Such rectangular windows permit laser entry from almost any direction in the trap plane, offering greater flexibility for laser alignment than commodity components such as CF flanged spherical octagons. A set of windows at 50 K matched to those on the OVC let light through the radiation shield. Two windows are used on each panel of the shield, sandwiched against the inside and outside faces (Fig. 2.2), allowing the outer window to thermally shield the inner one. The large aspect ratio of the windows is particularly advantageous, providing wide-angle laser access while maintaining a small

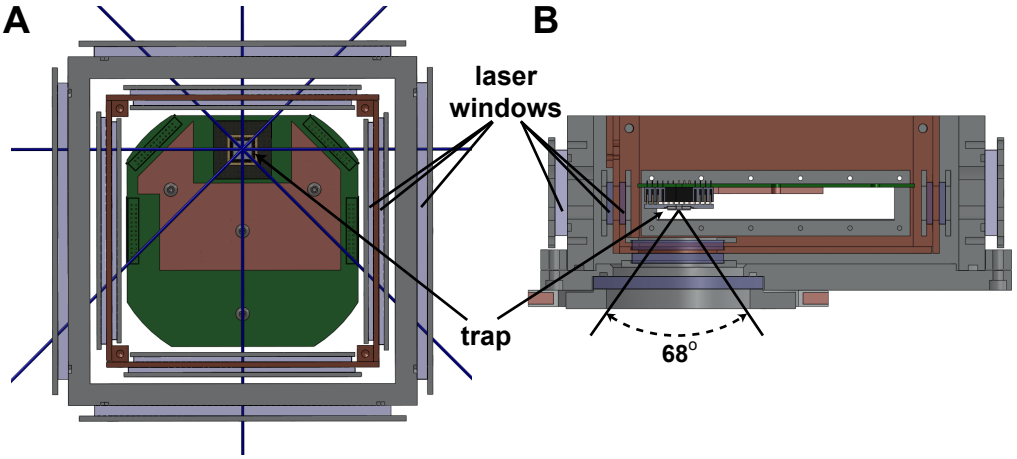

Figure 2.3: Cross-sections showing optical access to the trap. (a) Side view. (b) Bottom view, with typical laser paths indicated.

distance between the windows' centers and their heat sunk perimeter. To ensure access along key diagonal beam paths (which would otherwise be blocked by the corners of the square OVC), the trap is shifted off-center in the cryostat (Fig. 2.3a). All side windows are made of BK7 and W anti-reflection coated at 400 and 800 nm, reducing reflection to $< 1\%$ per face at all laser wavelengths. Note these windows are not optically flat. An optical breadboard mounted to the extruded aluminum superstructure holds optics for aligning lasers across the trap.

Ion fluorescence is collected through an additional stack of circular windows located directly underneath the ion trap, V-coated at 397 nm for detection of Ca^+ fluorescence. The 300 K window (6.25 cm clear aperture) is recessed into the OVC bottom plate to mimimize the distance between room temperature light collection optics and the ion trap, allowing for light collection over a large solid angle of nearly 2 sr (Fig. 2.3b). As such, efficient fluorescence collection is feasible without the use of in-vacuum optics. Instead, $\sim 4\%$ of the ions' fluorescence is collected using a home-built NA 0.4 lens. The lens is attached to the OVC bottom via a 2-axis translation stage (OWIS KT150) (Fig. 2.4), so that the optical axis of the imaging system can be carefully aligned to the trapped ions to eliminate vignetting and minimize coma. The collected fluorescence is divided between a CCD camera (Princeton Instruments Cascade 1K) and a photo multiplier tube (PMT;

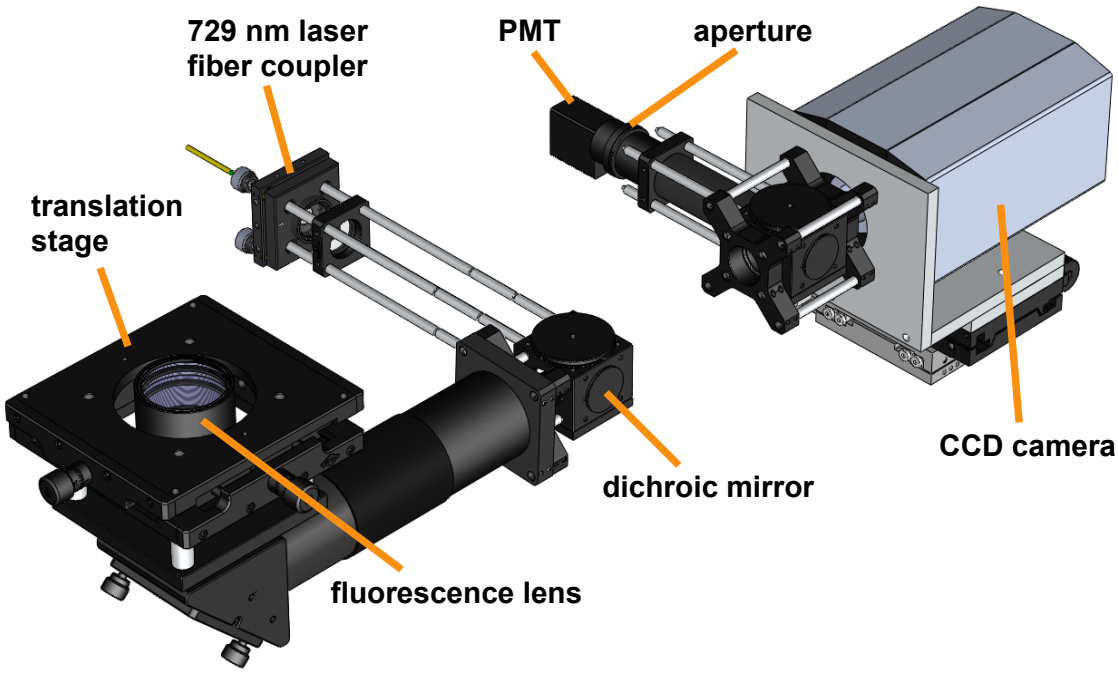

Figure 2.4: The fluorescence optics and detectors. The translation stage mounts directly to the OVC fluorescence window compression plate and is supported from below. The CCD camera is mounted to the optical table. The 729 nm laser beam path used for $\hat{y}$ micromotion compensation (Sec. 3.5) is also illustrated.

Hamamatsu H10682-210) by a 50/50 beamsplitter. The back focus is separately controlled by adjusting the camera position along the optical axis. An aperture in the PMT optical path is placed at the back focus to minimize the detection of scattered laser light.

2.2.5 Electrical Components and Connections

The cryostat is outfitted to accept traps affixed to commercial 100-pin ceramic-pin-grid-array (CPGA) chip carriers, standardizing the installation of traps with varying electrode layouts. Carriers are mounted in a 100-pin socket soldered to a fan-out PCB (Fig. 2.5) made of FR-4 laminate, with each pin filtered by a 33 nF capacitor to ground. The capacitors are made of NP0 ceramic and show a negligible temperature dependence during cooldown to 4 K. One pin in each quadrant is grounded at the socket, while the remaining twenty-four pins are routed to a shrouded rectangular header on the perimeter of the

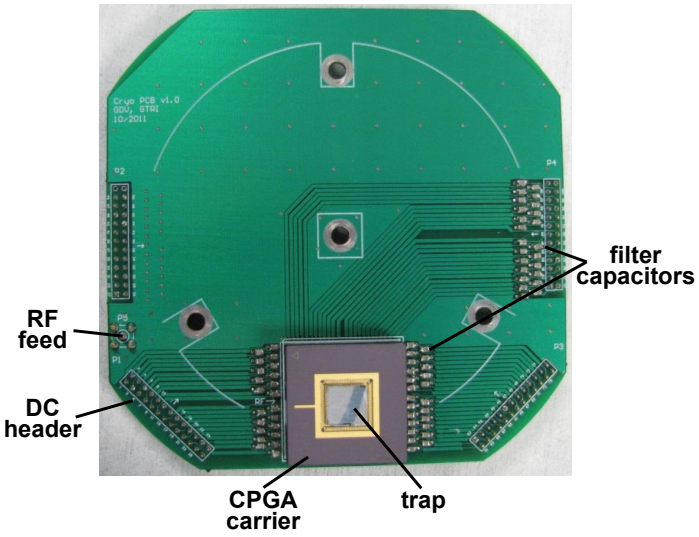

Figure 2.5: The trap socket (with trap installed) and fan-out PCB used to couple DC and RF voltages to the trap electrodes.

PCB. These headers are fed via wiring from 24-pin O-ring sealed electrical feedthroughs (Fischer DBPE 105 A093-89) in the upper OVC. 36 AWG quad-twist phosphor-bronze wire (Lakeshore WQT-36), heat sunk to the cryocooler's first stage, carries direct current (DC) voltages to a secondary heat sink at 4 K. Here the wiring transitions to 32 AWG copper, allowing the DC connections to help heat sink the CPGA and individual trap electrodes. Two additional 24-pin feedthroughs provide wiring, also heat sunk to the first stage, for thermometers (Lakeshore DT-670B1-CU), heaters, the neutral atom oven source, and any future electrical accessories. Each section of wiring is wrapped around a copper bobbin and then mechanically and thermally bonded to the bobbin using epoxy (Stycast 2850 FT). The bobbin is then mounted to one of the coldplates. This modularity allows sections of the wiring to be replaced or repaired without removing the entire wire bundle. The DC voltages are supplied through a room temperature third-order lowpass Butterworth filter which has a cutoff frequency of 40 kHz when combined with the wire resistance and the PCB filter capacitance. Detailed electrical mappings for the trap, socket and PCB can be found in Appendix A; similar mappings can be found in Appendix B for the DC as well as thermometry wire bundles.

The upper OVC also features four SMA feedthroughs (Pasternack PE9184) for introducing RF signals. Low thermal conductivity stainless steel coaxial cables (Lakeshore CC-SS) carry signals to panel-mount bulkhead SMA connectors attached to the radiation shield, heat sinking the cables at 50 K. Signals continue from this point via stranded copper coaxial cable (Lakeshore CC-SC). Two lines connect to the trap's RF electrodes via a compact inductively-coupled helical resonator [59]. One line feeds the RF drive voltage, while the second is an optional DC bias voltage (usually grounded). The resonator is constructed from a 2.65" length of 2" copper pipe (alloy C12200), designed for a resonant frequency of approximately 50 MHz when loaded by the PCB, socket, and trap, with quality factors of 90 (350) at 300 (4) K, respectively. One of the remaining two RF lines is connected to an antenna used to monitor applied RF voltages, and the second to a copper ground screen mounted over the trap that shields stray electric fields and can be driven for secular mode frequency measurements.

2.2.6 Oven

Ion traps are commonly loaded by photoionizing atoms from a flux of neutrals sourced by a resistively heated oven [3, 39–41, 45, 60, 61]. Depending on the species this can require temperatures well in excess of 1000 K, thus ovens impose a significant thermal load (typically several watts) when energized. Other methods, such as laser ablation [50] or transfer from a magneto-optical trap (MOT) [52], offer alternatives with lower heat loads more appropriate for a cryogenic environment. However, laser ablation requires an additional pulsed laser and lacks the species-selectivity of photoionization unless used carefully in a regime of low pulse energy [62], and for many experiments the efficient trap loading offered by a MOT does not merit the increase in experimental complexity. Fortunately, suitable thermal shielding and heat sinking can mitigate the degree to which an oven source heats the ion trap, making ovens a viable option in cryocooler-based systems for which there is no concern over liquid helium boiloff.

For this apparatus, the oven is designed for use with backside-loaded ion traps and thus is situated behind the trap mounting socket. This puts the oven above the trap, so a

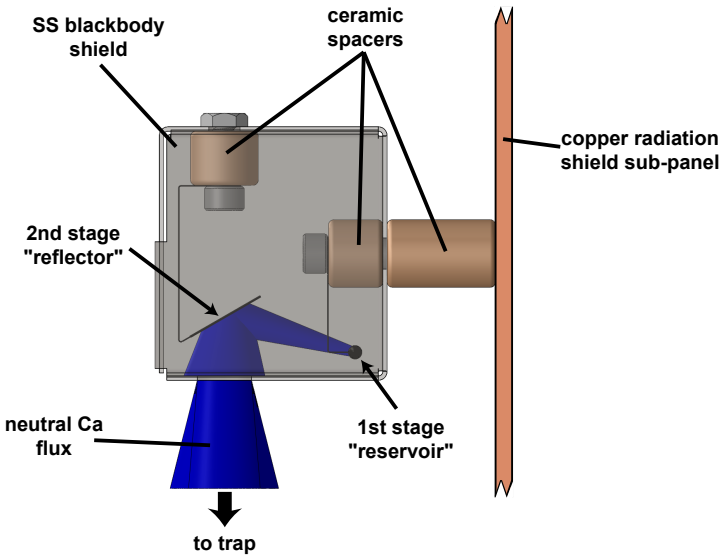

Figure 2.6: The two-stage oven. The second stage can be prepared by applying current to the reservoir. Applying current to the second stage then projects calcium flux onto the trap without risking oxide dust or fragments falling to the trap below.

two-stage design similar to Ref. [60] (Fig. 2.6) is used to minimize the chance of oxide and dust falling from the oven onto the trap below where it can obstruct the loading slot. In this design, a first stage reservoir of calcium metal is resistively heated, producing a flux directed *away* from the trap. A second stage reflector, also resistively heated, redirects this flux towards the trap loading slot. For reduced power consumption and thus heating of the surrounding environment, the second stage can be heated independently once coated. The source is made from stainless steel (SS) capillary tube (125 μm wall thickness, 3 mm OD), filled with calcium metal and crimped/spot-welded on each end to short lengths of 125 μm diameter SS wire. A small slit cut circumferentially allows neutral flux to escape towards the second stage – a small square of 50 μm thick SS foil spot welded to SS leads. Both oven stages are anchored to ceramic posts inside a SS sheet metal box which shields emitted blackbody radiation and helps with differential pumping. This box is mounted to a subpanel on the copper radiation shield, dissipating the heat load to the cryocooler's first stage while minimally heating the ion trap. This panel may be easily removed and the oven stored elsewhere to minimize oxidation of the calcium metal when the cryostat is opened. In use the first stage is driven with 2 A to coat the second stage and then deenergized

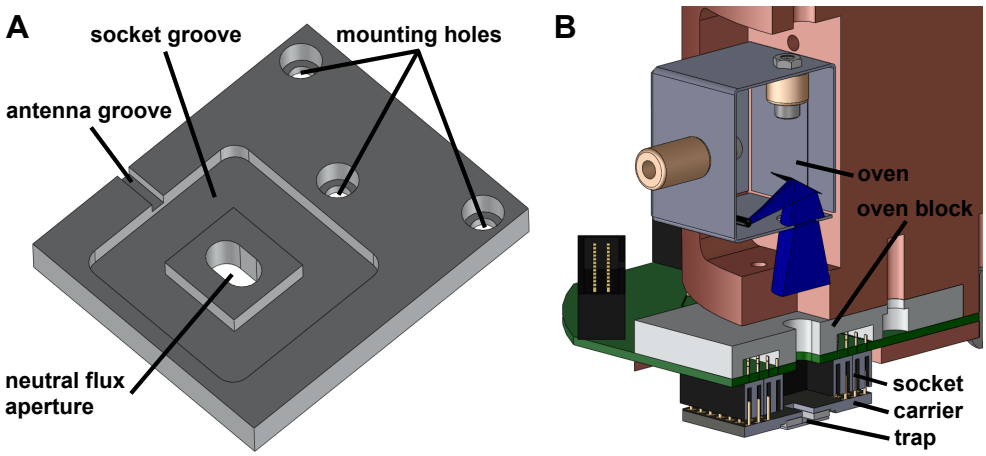

Figure 2.7: (a) The oven block. The socket groove is a milled region that protects the socket pins and carrier from being coated by neutral flux as it passes through the neutral flux aperture. The aperture also collimates the beam of neutral particles. The raised central region around the aperture provides additional thermal contact between the PCB and spacer block just below the socket. The antenna groove mechanically stabilizes the antenna used to monitor the trap RF voltage. (b) A section view of the copper spacer block, oven, and trap with the oven block installed.

resulting in a total power dissipation of 1.9 W. The second stage is then supplied with 1.3 A to load single ions, dissipating a total power of 1.4 W.

One danger of backside-loaded surface-electrode ion traps is that a film of metallic neutrals can form on the back of the trap carrier. Depending on the flux path, this can cause carrier pins to short circuit to each other, the RF line, or ground. Though some of these issue can be mitigated with clever electronic waveform design, issues such as the RF pin shorting to ground renders trapping impossible and must be avoided at all costs. To protect against this, an oven block (Fig. 2.7) is used which obstructs line-of-sight between the oven and socket pins. The oven block sits between the PCB and the spacer block and is mechanically anchored to the latter. Additionally, the oven block stiffens the PCB directly below the socket greatly easing the trap installation process.

CHAPTER III

CHARACTERIZATION OF THE APPARATUS

3.1 Experimental Fundamentals

3.1.1 Ion Trapping

The fundamentals of ion trapping as well as a wealth of other trapped ion related information can be found in Refs. [44, 63, 64]. Briefly, charged particles such as ions can be spatially confined within a macroscopic linear Paul trap (Fig. 3.1) through the combination of a DC harmonic potential along the trap axis and a radial RF pseudopotential. Axially, confined particles undergo simple harmonic motion; however, radial motion is governed by the Mathieu equations [65]. The radial motion can be decomposed into simple harmonic motion at the secular frequency and micromotion, a component that oscillates at the RF frequency. Due to the close similarity between the secular motion within the ion trap and that of a 3D anisotroptic harmonic oscillator, a quantum mechanical treatment due to Glauber allows the ion motion to be expressed in the basis of harmonic oscillator Fock states, $|n\rangle$ [66]. The expectation value of the motional state of the ion in the Fock basis provides the average number, $\bar{n}$, of vibrational quanta, known as phonons, for a specific secular mode. In the case of trapped ions, the Fock states are not energy eigenstates as they only account for the secular motion and not the micromotion; however, $\bar{n}$ is proportional to the averaged energy of the ion over a single RF drive period.

As mentioned in Chapter 1, the linear Paul trap can be transformed to a planar geometry [2]. For the experiments described in this thesis, a Georgia Tech Research Institute (GTRI) Gen IIc surface-electrode ion trap is used (Fig. 3.2) [67][3]. This aluminum-on-SiO_2 trap features a small loading slot, 60 μm ion height, and forty-four DC electrodes that allow for the fine tuning of control potentials. The trap is epoxied (EPO-TEK H21D) to an

[3]This manual actually refers to the Gen II which has the ion trapping region off-center. The Gen IIc is very similar other than this gross change in geometry and the addition of two long radial control electrodes parallel to the RF electrodes. The majority of the information in the manual is applicable to the Gen IIc.

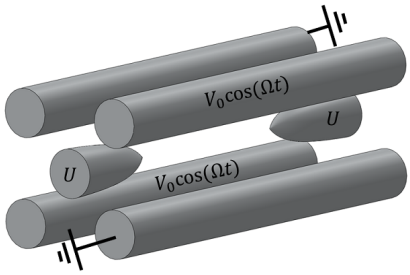

Figure 3.1: A macroscopic linear Paul trap. A voltage U is applied to the endcaps to axially confine ions within a harmonic potential. Two diagonally-opposed rods are grounded and an RF voltage $V_0 \cos(\Omega t)$ is applied to the other two. This voltage configuration generates an oscillating quadrupolar electric field for radial confinement.

alumina spacer mounted on a ceramic pin grid array (CPGA) carrier. Electrical connections to each electrode are made by two 25 μm diameter 99% Al/1% Si wirebonds; these wirebonds are also the primary thermal anchoring for the trap. Additional trap details can be found in Appendix A. DC voltages are supplied to the trap by a PXI chassis (National Instruments PXI-1045) containing thirteen 8-channel digital-to-analog converter (DAC) cards (National Instruments PXI-6713). One DAC card is used for uniform triggering of DC voltage changes across the chassis and the remaining cards are used to provide 96 analog output voltages. The RF drive is provided by an analog RF signal generator (Hewlett Packard E4420B), amplified (Minicircuits ZHL-5W-1), and fed to the helical resonator. A voltage variable attenuator (Minicircuits ZX73-2500-S+) prior to the amplifier allows for active stabilization of the RF power.

3.1.2 Ca^+ Production and State Detection

The energy level diagram for Ca II is presented in Fig. 3.3. Ions of $^{40}Ca^+$ are produced above the surface of the trap by photoionization of neutral calcium flux from the resistively heated oven [61]. Doppler cooling on the $S_{1/2} \rightarrow P_{1/2}$ transition at 397 nm, with a repump laser tuned to the $D_{3/2} \rightarrow P_{1/2}$ transition at 866 nm, is used to reduce the ion temperature to $T \sim$1 mK [68, 69]. For typical trap frequencies, this places the ion firmly within the Lamb-Dicke regime and thus the ion is well localized and appears as a single spot. During Doppler cooling, 397 nm ion fluorescence is continuously imaged onto the CCD camera to provide a wide field of view and single ion resolution; this fluorescence is also directed

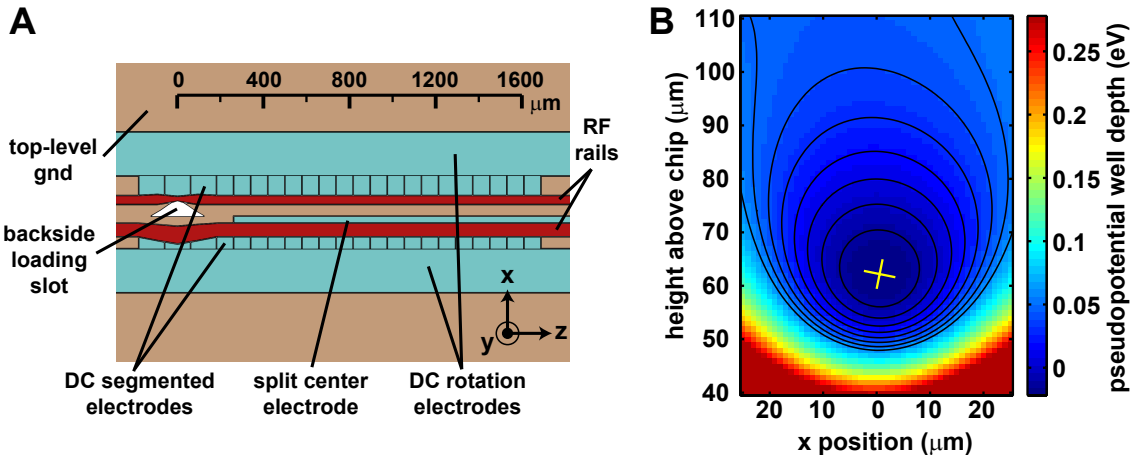

Figure 3.2: The surface-electrode ion trap. (a) A top-down cartoon of the planar trap. (b) A color plot of a typical total pseudopotential used in experiments with an overlay of equipsuedopotential curves. A DC quadrupole has been added to the RF pseudopotential in order to lift the degeneracy of the radial secular modes as well as rotate the secular axes. A trapped ion's radial motion can be decomposed along the secular axes which are represented by the yellow cross at the pseudopoential null; the axis associated with the upper radial mode is 12° from vertical and the axis associated with the lower radial mode is 12° from horizontal. A number of equipsuedopotential curves have been omitted for clarity.

to the PMT for high speed, high fidelity single ion state detection. A narrow bandpass fluorescence filter (Semrock FF01-395/11-25) is placed just before the beamsplitter so that only 397 nm light is detected.

The ion is also probed on the $S_{1/2} \rightarrow D_{5/2}$ quadrupole transition at 729 nm to take advantage of the narrow linewidth, $\Gamma = 2\pi \times 0.21$ Hz. As $^{40}Ca^{+}$ lacks nuclear spin, both energy levels are Zeeman manifolds and the degeneracies may be lifted through the application of a magnetic field. A 3 gauss magnetic field is used to split the transitions between these manifolds by several MHz. Typically, spectroscopy is performed on the $S_{1/2}, m_j = -1/2 \rightarrow D_{5/2}, m_j = -5/2$ transition and initialize the system to the $S_{1/2}, m_j = -1/2$ level via optical pumping on the $S_{1/2}, m_j = 1/2 \rightarrow D_{5/2}, m_j = -3/2$ and the $D_{5/2} \rightarrow P_{3/2}$ transition at 854 nm.

Spectroscopy is performed in a discrete manner to allow very short interrogation times. A typical spectroscopic cycle consists of a 729 nm laser pulse of fixed intensity and time

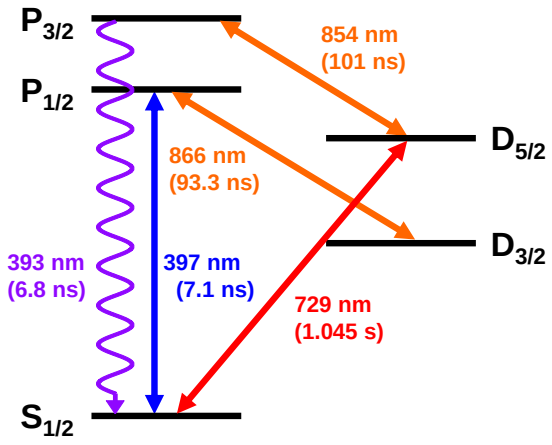

Figure 3.3: Ca II energy level diagram. This includes all relevant Ca II energy levels, transitions, wavelengths, and lifetimes used in these experiments. The solid lines represent driven transitions and the wavy line represents a non-driven transition that proceeds only via spontaneous emission. Adapted from Ref. [70].

followed by application of the 397 nm and 866 nm lasers for a period during which ion fluorescence is collected. State determination is possible via the electron shelving method [71]. If the 729 nm laser pulse excites the ion to the $D_{5/2}$ manifold, the single valence electron will be considered "shelved" and the ion will not scatter any 397 nm light. Alternatively, if the ion is not excited by the 729 nm pulse, it will stay in the ground state and scatter many 397 nm photons during the detection step. Following state detection, the ion is then reinitialized to the ground state through a single pulse of the 854 nm laser. For a given 729 nm laser frequency, this cycle is repeated 400 times and the resulting data are used to calculate the probability of excitation.

As the ion's internal transitions are oscillatory in nature, they are modulated by the ion motion resulting in the appearance of frequency sidebands according to the Fourier transform of the motion [72]. The sidebands can be used for sensitive detection of the ion's motion, an advantage that will be exploited while characterizing this system.

3.1.3 Laser Stabilization and Experimental Control

The 397, 423, 854, and 866 nm lasers are frequency stabilized by locking them to a stabilized HeNe laser via a low finesse, $\mathcal{F} < 100$, transfer cavity [73]. The 729 nm laser is frequency

stabilized and linewidth narrowed via the Pound-Drever-Hall method [74] to a high finesse, $\mathcal{F} \sim 10,000$, ultra-low expansion cavity. A 377 nm laser diode is used for the second step of photoionization. All lasers except the 377 nm laser are external cavity diode lasers (Toptica DL100). The 423 nm laser consists of a 846 nm external cavity diode laser followed by a second-harmonic generation stage.

Frequency control of the 423 and 866 nm lasers is possible by adjusting the external cavity length via a piezoelectric element. The 397, 729, and 854 nm lasers are each double passed through an acousto-optical modulator (AOM; Brimrose TEM-200-50) for fast (10 ns rise time) amplitude, frequency, and phase control of the laser beam. A collection of USB controlled frequency sources (Vaunix LGS-251) and TTL controlled RF switches (Minicircuits ZASWA-2-50DR+) control the 397 nm laser AOM. A direct digital synthesizer (DDS; Analog Devices 9910/PCBZ) is the source for the 729 nm laser AOM. To reach the powers necessary to drive the AOMs these sources are amplified (Minicircuits ZHL-1-2W).

Experimental control is provided by a field programmable gate array (FPGA; Sparkfun DEV-08458) which can output TTL pulses, serially communicate with the direct digital synthesizer, and receive serial input signals such as provided by the PMT. Data collection and computer control of the entire experiment is performed using Wavemetrics Igor Pro v. 6.2.1.0. The FPGA is programmed using high-level Igor code which is compiled into a low-level "pulse program" and transferred from the experimental control computer to the FPGA through a USB connection.

3.2 Cooldown and Trap Temperature

Prior to cooling the cryostat, a turbopump is used to pump on the system while the charcoal getters are gently heated ($\sim$ 320 K), emptying them of adsorbed water vapor. Pumping overnight brings the chamber pressure to approximately 5×10^{-5} mbar. Energizing the cryocooler then rapidly cools the interior of the cryostat; the ion trap temperature drops below 10 K within five hours, with temperatures fully equilibrating ($T_{\mathrm{trap}} = 5.5$ K) in approximately twelve hours. Once cold, cryopumping reduces the chamber pressure outside of the copper radiation shield to approximately 5×10^{-7} mbar, with lower pressures inside

the differentially pumped volume.

During normal operation, the RF electrodes on the trap are driven at $\Omega_{RF} \sim 2\pi \times$ 50 MHz to create the trapping pseudopotential. Based on the increase in temperature of the cryocooler's second stage, a typical RF drive of 70 V_{RMS} dissipates approximately 100 mW among the resonator, PCB, CPGA carrier, and trap. Thermometry mounted on the top ground plane of a diagnostic trap indicated that application of this RF drive warmed the trap by approximately 6 K (Fig. 3.4), dominated by a thermal gradient between the CPGA carrier and the low-vibration coldplate. The trap and CPGA carrier are thermally anchored via the DC electrical connections. At the time of the trap temperature measurement, the DC feeds were heatsunk via the phospher-bronze DC wiring only, approximately 15 cm distant. Since then, a copper heatsink has been added to the fan-out PCB, thermally anchoring 72 of the DC traces adjacent to the trap mounting socket. This should reduce the thermal gradient between the CPGA and cold-plate, dropping the trap temperature to $\sim$ 8 K under normal operating conditions. Energizing the oven warms the trap by an additional $\sim$ 1 K due primarily to blackbody radiation. No thermometry is mounted on the trap during normal operation. However, temperatures are monitored at the socket, PCB ground plane, spacer block, 4 K and 50 K getters, and the cryocooler's second stage.

The presence of heating due to the RF drive is a constant of routine trap operation; however, heating of the trap, PCB, and spacer block due to energizing the oven is not. The heat load due to the energized oven will outstrip the cooling power of a typical cryocooler as evidenced here. The increased temperature may result in an increased local vapor pressure of gases such as H_2 in the trapping region and thus an increased neutral-ion collision rate. In cases where this must be avoided, the use of a helium exchange gas vibration isolation system may be beneficial due to liquid helium condensing on the cold plate and acting as a thermal capacitance. The downside to this approach is the reduced total cooling power of most helium exchange gas equipped cryocoolers.

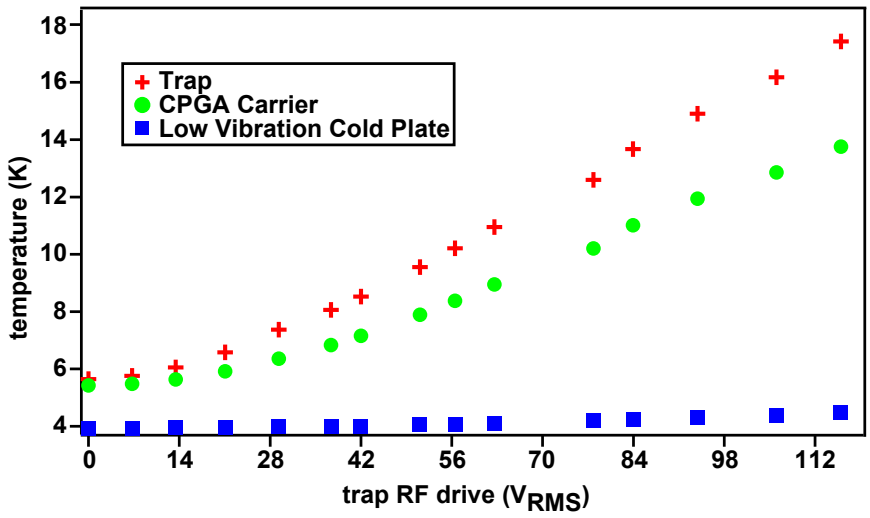

Figure 3.4: Thermal performance as a function of RF drive voltage. Trap temperatures are measured on the top ground plane at the periphery of the trap chip; thermal modeling suggests that the RF electrodes are 10-20 K higher in temperature.

3.3 Vacuum and Trapping Lifetime

Despite the poor vacuum in the room temperature region outside of the copper radiation shield, the vacuum around the ion trap is excellent. The 50 K wall temperature of the radiation shield suppresses line-of-sight outgassing toward the ion trap, so the gas load is dominated by flow from the 300 K exterior of the cryostat through small gaps in the shield. Fortunately, all gases with non-negligible vapor pressures at 50 K have binding energies on charcoal exceeding 100 K [75] and are effectively adsorption pumped onto the cryocooler's second stage and the 4 K charcoal getter.

To measure the quality of the vacuum, the lifetime of single $^{40}Ca^{+}$ ions in the trap is determined. As the Doppler-cooled ions survive in the trap for many hours, the lifetime of the ion in the absence of cooling light is instead measured. After cooling the ion, the 397 nm laser is blocked for successively longer intervals and ion survival is verified after each interval via fluorescence measurement. The trap is reloaded each time an ion is lost and data collection commences after a pause to ensure that the oven has cooled and the system returned to its steady-state conditions. The experiment is repeated many times to obtain ample statistics and error bars are generated with the Beta distribution. A half-life of

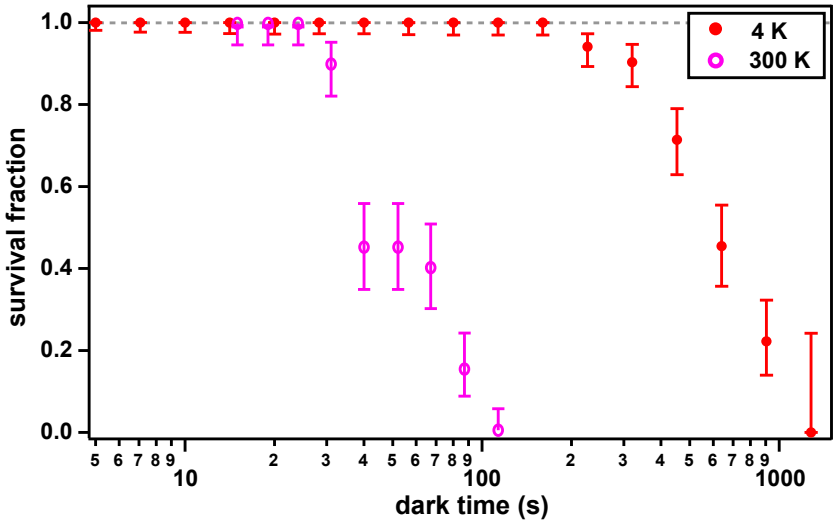

Figure 3.5: Single ion lifetime in the absence of Doppler cooling in a harmonic ($\omega_z = 2\pi \times 1$ MHz) well with calculated trap depth 100 meV axially and 32 meV radially. Room temperature data are from Ref. [39].

approximately 600 s (Fig. 3.5) is found for a radial well-depth of 32 meV, significantly longer than the 45 second lifetime measured in a room temperature experiment at 10^{-11} mbar [39].

3.4 Vibration

One significant drawback of closed-cycle cryocoolers is vibration induced by the motion of helium gas through the cold-head. For ion trapping this motion leads to blurring of ion fluorescence images as well as phase noise on qubit rotations. These vibrations are reduced in the cryogenic apparatus due to the mechanical decoupling of the low-vibration stage. However, some vibration remains due to minute deformations of the cold-head's SS top flange which are transmitted down the G-10 support rods of the low-vibration assembly to the isolated coldplate [76]. This residual vibration can be quantified by focusing a laser beam past a razor blade mounted on the low vibration stage and measuring the time variation of the transmitted laser power. With an appropriate focus and a suitable mapping of the detector signal to beam position, sub-micron measurement of the blade position is possible (Fig. 3.6a,b).

The position of the ion can also be directly measured as a function of the motional cycle of the cryocooler by imaging ion fluorescence onto the CCD camera. Using a full-bridge

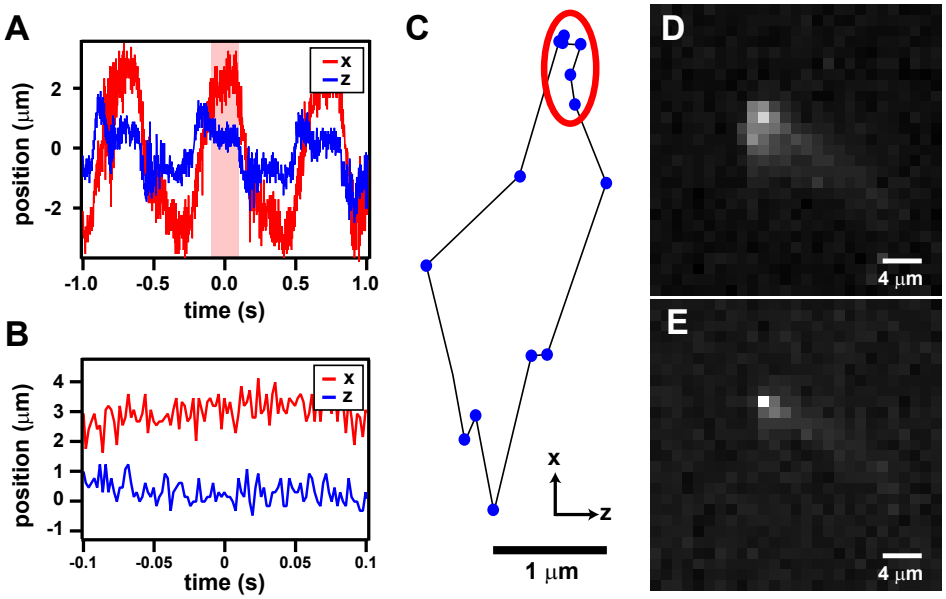

Figure 3.6: Motion of the low-vibration stage. (a, b) Cryostat vibration in the plane of the ion trap as measured using a razor blade, with directions matching the trap axes indicated in Fig. 3.2a. (b) shows the shaded region from (a). High frequency noise is due to detection electronics and motion is negligible along $\hat{z}$. (c) Ion motion mapped by triggered CCD fluorescence images. Each point is separated in time by 50 ms. The circled cluster of points approximately matches the shaded region in (a). (d, e) Fluorescence images of the ion averaged over one cycle of the cryocooler vibration or triggered during the low-motion window, respectively. The "comet tail" extending down and to the right is due to optical aberration rather than vibrations.

strain gauge sensor, a TTL trigger signal is generated with which the illumination of the ion can be referenced to the motional cycle. The sensor is mounted to a cantilever which bends due to motion of the flex line between the cold-head and remote motor. Details of the trigger circuit can be found in Appendix C. By fitting a Gaussian to the CCD image and extracting the ion's position, it is possible to map out the ion motion (Fig. 3.6c). These data agree with the razor blade measurements; both methods indicate a total motion of approximately 4.5 μm peak-to-peak parallel to the trap surface. Measurements with the razor blade indicate motion of <1 μm peak-to-peak perpendicular to the trap plane. However, by triggering experimental data acquisition to coincide with a low-motion window of the cryostat's motional cycle, the effective vibration can be reduced to <1 μm (Fig. 3.6d,e). This value represents a significant improvement over the 12 μm peak-to-peak motion of the PT407 without vibration isolation [76] or the $\sim$15 μm peak-to-peak motion of a large, unstabilized bath cryostat [56]. However, it is considerably larger than the $<$106 nm motion reported for a closed cycle system using a helium-gas heat exchanger [50]. Further vibration reduction is possible if the isolated coldplate were anchored to the stiff aluminum mounting plate instead of the room temperature flange of the cryostat as discussed in Appendix D.

3.5 Measurement and Compensation of Stray Electric Fields

Despite careful surface-electrode trap fabrication, trapped ions often experience forces due to stray electric fields originating from charging and contamination of the trap and surrounding environment. These fields can cause excess micromotion, reducing Doppler cooling efficiency and possibly increased ion heating rates [63]. It is thus important that these fields be characterized and controlled; following measurement, stray fields can be cancelled through the application of suitable potentials to the trap electrodes.

Two primary methods are utilized to determine the presence of stray electric fields. For the $\hat{z}$ direction, the combination of a stray electric field and the harmonic trapping potential results in a first order shift of the position of the harmonic well minimum, $\Delta z_{min} = eE_z/m\omega^2$, where e is the electron charge, E_z is the stray field, m is the ion mass, and ω is the axial secular frequency [39]. A typical single location stray field scan consists of

measuring the ion position on the CCD at three different axial well strengths. The CCD pixel resolution and fluorescence stack magnification limit the minimum detectable stray field value to 5-10 V/m. With smoothing of the CCD image, subpixel resolution makes it possible to detect fields of only a few V/m.

Along the radial directions ($\hat{x}$ and $\hat{y}$), a stray field will displace the ion from the RF null. The ion will then sample regions of higher RF field strength resulting in an increase in micromotion amplitude. Micromotion sidebands can be measured on a given ion transition to determine the necessary compensation field [72]. For the $\hat{x}$ direction, the 397 nm transition is used as the natural linewidth of 22 MHz allows the micromotion sidebands at $\sim$50 MHz to be detected. Typically, the laser frequency is set to $\omega_l = \omega_0 - \omega_{RF}$, where ω_0 is the unmodulated transition frequency, and the compensation field swept until the fluorescence detected by the PMT is minimized. Fields can typically be nulled to $<$10 V/m.

However, in surface-electrode traps it is more challenging to minimize micromotion along $\hat{y}$. This requires that there be overlap between the probe laser's propagation direction and the y-axis, leading to unacceptable levels of light scatter and charging of dielectrics by the blue fluorescence lasers generally used. Two principle alternatives have been developed for measuring $\hat{y}$ micromotion: orienting the infrared repumping lasers along this direction [45] and parametrically exciting the ion [77, 78]. Here a third alternative is presented: monitoring micromotion sidebands on the 729 nm transition, for which surface charging effects are negligible [79, 80]. The 729 nm laser is aligned onto the ion by projecting it backwards down the fluorescence collection optics via a dichroic mirror (Semrock FF670-SDi01-25x36). As this aligns the beam along $\hat{y}$, micromotion in this direction may be easily minimized by monitoring first- and second-order micromotion sidebands and adjusting applied compensation fields (Fig. 3.7).

3.6 Ion Heating

Along with improved vacuum, reduced ion heating rates are the dominant motivation for cryogenic ion trapping systems. These rates can be determined using Doppler recooling [81] and secular motional sidebands [43, 82]; the latter is implemented here. As the secular

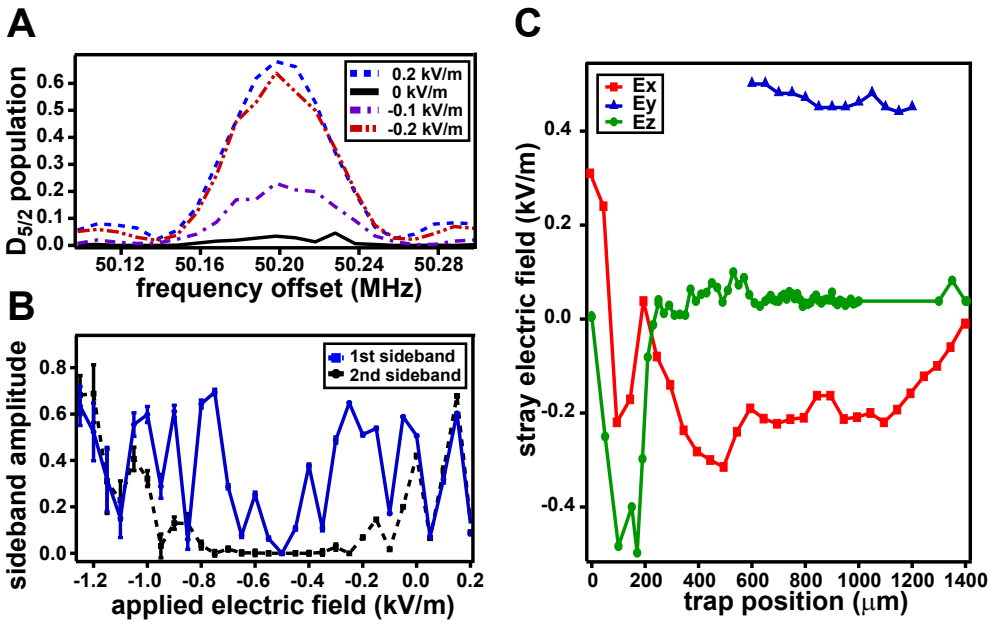

Figure 3.7: Compensation of stray electric fields. (a) Micromotion sidebands may be probed perpendicular to the trap plane using a laser tuned to the $S_{1/2} \rightarrow D_{5/2}$ transition at 729 nm. (b) Stray electric fields are compensated when both the first- and second-order sidebands are simultaneously minimized. (c) Measured stray electric fields in three dimensions.

frequencies are <10 MHz, these sidebands cannot be resolved on the 397 nm transition and thus the 729 nm transition must be probed instead.

Spectroscopy is performed on the $S_{1/2}, m_j = -1/2 \rightarrow D_{5/2}, m_j = -5/2$ transition which consists of a carrier and k^{th}-order secular motional sidebands (Fig. 3.8). The carrier represents a pure electronic transition with no change in motional state, $|n\rangle \rightarrow |n\rangle$, at $\omega = \omega_0$. The sideband transitions represent Jaynes-Cumming interactions in which there is a change in electronic state as well as a change in motional state. A *red* sideband represents an electronic excitation and a lowering of the motional state, $|n\rangle \rightarrow |n-k\rangle$, at $\omega_{rsb} = \omega_0 - k\omega_{sec}$. A *blue* sideband represents an electronic excitation and a raising of the motional state, $|n\rangle \rightarrow |n+k\rangle$, at $\omega_{bsb} = \omega_0 + k\omega_{sec}$.

When the ion is in a thermal motional state, the probability of exciting a k^{th}-order sideband is proportional to the average number of phonons in a given secular mode such that $P^k_{rsb} \propto (\bar{n})^k$ and $P^k_{bsb} \propto (\bar{n}+1)^k$. The ratio of the red and blue k^{th}-order sideband

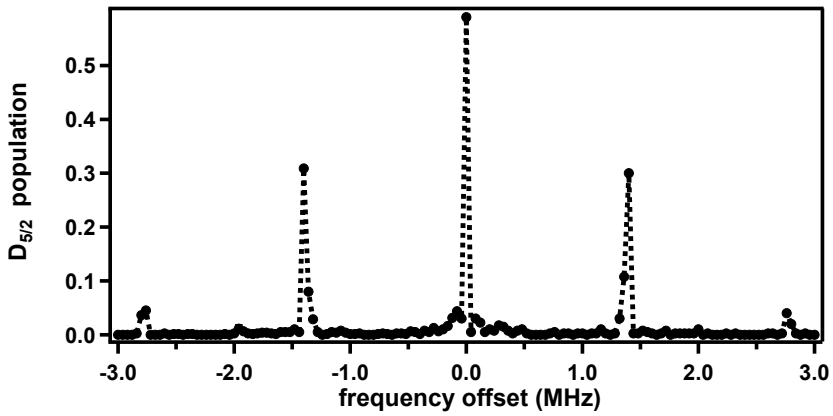

Figure 3.8: A typical sideband scan across the $S_{1/2}, m_j = -1/2 \rightarrow D_{5/2}, m_j = -5/2$ transition centered on the carrier. The first- and second-order axial secular motional sidebands ($\omega_z = 2\pi \times 1.37$ MHz) are evident. Note that the red and blue sidebands are approximately the same height; this is due to the ion having a large number of axial motional quanta.

heights, $r_k = P^k_{bsb}/P^k_{rsb}$ can be used to determine the average phonon number:

$$\bar{n} = \frac{1}{(r_k)^{1/k} - 1} \tag{3.1}$$

For maximum sensitivity, the k^{th}-order sidebands for which $k \sim n$ should be probed [43] and the blue sideband height maximized, that is a π-pulse should be applied on the blue sideband, through the appropriate choice of laser pulse amplitude and duration.

In order to determine the ion heating rate via this method, the ion is first initialized in the motional ground state through resolved sideband cooling [82]. Briefly, a 729 nm laser pulse is used to drive the red sideband followed by an 854 nm laser pulse and spontaneous emission of a 393 nm photon. This cycle is repeated with increasing 729 nm pulse time until the mode of interest has $\bar{n} < 0.05$. Following motional initialization, all laser light is extinguished and the ion motional state is allowed to evolve for a set period of time. The average phonon number is then calculated from Eq. 3.1.

The heating rate of a single trapped ion from the ground state is determined for all three secular modes $\omega_z = 2\pi \times 1.38$ MHz, $\omega_{r_1} = 2\pi \times 4.64$ MHz, $\omega_{r_2} = 2\pi \times 5.46$ MHz, to be 41(3), 24(3), and 110(3) quanta/sec, respectively (Fig. 3.9). As similar measurements elsewhere indicate that heating rates scale as ω^{-2} [43], it seems likely that the RF trap drive is inadequately filtered by the helical resonator. This would predominantly increase heating of the radial modes and thus the axial heating rate is taken as an upper bound on the trap's

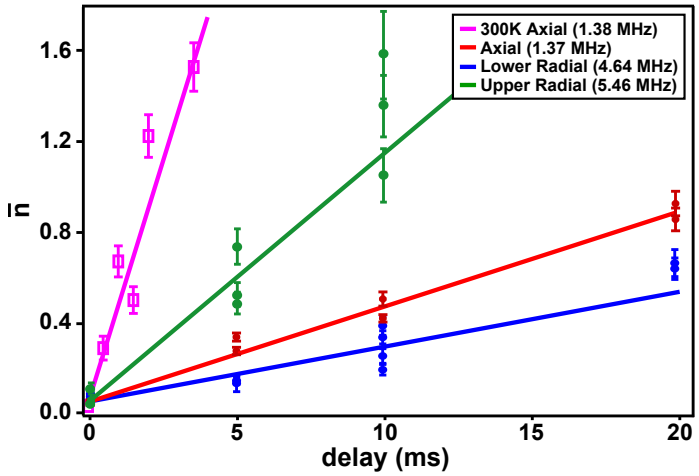

Figure 3.9: Ion heating. Fitted heating rates are 41(3), 24(3), and 110(3) quanta/sec for the axial, lower radial, and upper radial secular modes, respectively. The axial heating rate for an identical room-temperature trap is 410(40) quanta/s and the data can be found in Ref. [39].

spectral noise density, $S_E(\omega) < 3.8(3) \times 10^{-13}$ V^2/m^2 Hz, a reduction of approximately an order of magnitude over an identical trap measured at room temperature [39].

CHAPTER IV

CHAINS

4.1 Experimental Fundamentals

4.1.1 Transport

In order to implement the QCCD architecture, transport of single ions along the trap axis is necessary. The incorporation of junctions allows for the reordering of ion chains and the complex interconnection of various trapping zones [36]. A detailed consideration of one- and two-dimensional transport can be found in Ref. [83]. Briefly, in a linear Paul trap the RF pseudopotential "tube" confines ions in the radial direction and exhibits no $\hat{z}$ dependence due to the cylindrical symmetry of the RF electrodes. Confinement along $\hat{z}$ is provided by DC electrodes along the trap axis. By adjusting the voltages on the DC electrodes, it is possible to change the location of the axial potential minimum. Ideally, the null is moved over many secular motional cycles to minimize excitation of the ion motional modes. This excitation is caused by the acceleration of the well during transport [83]. Transport over only a few secular motional cycles, known as diabatic or fast transport, has also been demonstrated with minimal secular mode excitation [84, 85]. Transport through junctions, including turning, is more difficult, requires many more electrodes and results in greater heating of the ion [38].

In a linear trap, where chain reordering is typically difficult[4] and transport is one-dimensional, there are two main transport operations: linear transport and split/merge. During linear transport, a minimal set of DC electrodes (three per side when the ion is centered over an electrode and four per side as the ion moves between two electrodes) are used to create a harmonic potential. The ion sits at the minimum of this harmonic potential which is then translated (Fig. 4.1a).

A split/merge operation is more complicated and is typically spatially and temporally

[4]Though achievable as in Ref. [86] where they show deterministic reordering of a two ion chain using DC electric fields in a surface-electrode ion trap and propose the same in a three-dimensional linear ion trap.

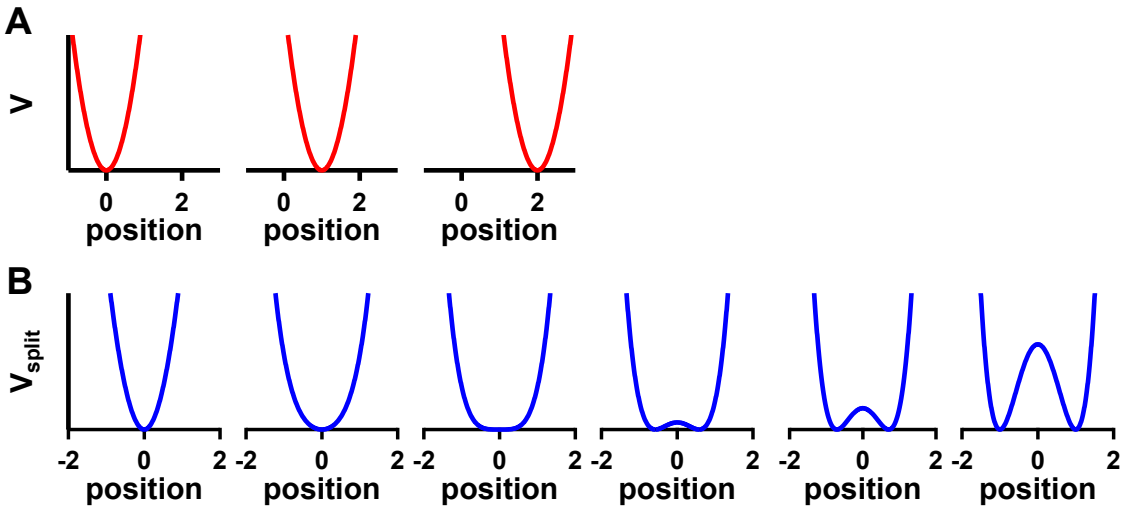

Figure 4.1: Basic one-dimensional transport potentials. Transport proceeds from left to right. (a) Linear transport. The ion experiences a potential of the form $V \propto (z - z_0)^2$. (b) Split/merge. The potential V_{split} (Eq. 4.1) is applied with $E_0 = 0$.

symmetric [87]. The following time-dependent potential is applied to two ions separated by a distance $2z$:

$$V_{split}(0, 0, \pm z, t) = V(t) - E_0 z + \alpha(t) z^2 + \beta(t) z^4 \tag{4.1}$$

The electric field, E_0, is used to tilt V_{split} such that a deterministic number of ions goes into each well upon splitting and V is a general offset. The ions also experience their normal Coulomb repulsion, $V_{coul} = e^2/8\pi\epsilon_0 z$. At the beginning of a split operation, the ions are in the same harmonic well such that $\alpha(t_0) > 0$ and $\beta(t_0) = 0$. The potentials are then ramped such that $\dot{\alpha}(t) < 0$ and $\dot{\beta}(t) > 0$ which weakens the harmonic potential confining the two ions, replaces it with the quartic potential, and then uses the now negative harmonic as a wedge to split the two ions (Fig. 4.1b). $V(t)$ is used to maintain a constant potential minimum value as the wedge is applied. The final values of these coefficients are $\alpha(t_f) < 0$, $\beta(t_f) > 0$, and $V(t_f) \geq 0$. At this point, two harmonic potentials with little overlap and centered on the individual ions can replace V_{split} and the ions can be individually transported away from each other if desired. The split procedure is performed in reverse to merge two harmonic wells.

For maximum flexibility during transport operations, it is desirable to have cooling light available at all potential trap positions. For this reason, the 866 nm repumper is aligned

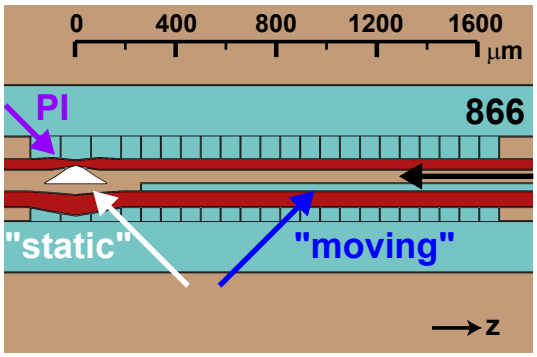

Figure 4.2: Laser beam orientation. The orientation and position of all laser beams (except those of the 729 nm laser) are indicated with respect to the trap. The "moving" beam can translate along the entire length of the trap while maintaining the same orientation. The copropogating photoionization lasers are labeled PI.

along the trap axis. However, this arrangement is inappropriate for the 397 nm Doppler cooling beam due to poor overlap with the ion's radial secular motional axes. Instead, a "moving" beam is aligned at a 45° angle with respect to the trap axis and a computer controlled, voice coil actuated mirror (Optics In Motion OIM101) is used to steer the beam along the entire length of the trap. A single analog output channel from one of the DAC boards provides the control voltage for the mirror. One additional 397 nm beam, which is referred to as the "static" beam, is aligned over the loading slot and perpendicular to the "moving" beam (Fig. 4.2). Movement of the fluorescence detectors is also desirable as the CCD camera's view width is only 710 μm and the PMT's view width is only 30 μm. The two detectors sit on a common stage and their position perpendicular to the optical axis, and thus along the trap axis, is determined by a motorized micrometer (Newport LTA-HS) with a computer controlled driver (Newport ESP300).

Throughout the rest of this chapter, various z positions will be referenced. These positions are labeled in Fig. 4.2 and more finely in Fig. A.1. The "moving" beam mirror is calibrated such that a command to move the laser to a given position will center the laser on a single ion at that position. For detector movement, the PMT aperture will be centered on the image of a single ion at that position.

4.1.2 Chain Building

Chain building in a three-dimensional linear Paul trap is straightforward as neutral flux from the oven can typically reach the entire trapping region. Thus ion loading continues at a given location until a sufficient number of ions have been trapped. However, deposition of neutral atoms may result in increased heating rates [43] and stray electric fields and field gradients [88]. For surface-electrode traps, the decreased ion-electrode distance exacerbates this issue and the reduced spacing between electrodes can result in unintended shorting. To combat this, most surface-electrode ion traps are backside-loaded [39]. The oven is situated behind the trap substrate and neutral flux is delivered through a hole which pierces the trap substrate. No neutral flux is directly incident on the trap. Though the loading slot can be extended along the entire length of the trap, this increases ion sensitivity to stray electric field sources behind the loading slot such as the trap substrate. For this reason, the Gen IIc surface-electrode trap has a small (240 μm) loading slot.

Since ions can only be initially trapped above the loading slot where ion heating and stability are typically worse, it is necessary to transport them away for experimentation. To automate this process, a procedure known as remote loading is used to load an ion at $z_0 = 0$ μm and transport it to $z_{rl} > z_0$. Initially, the "static" beam, the "moving" beam, and the 866 nm beam are unblocked. The "moving" beam and PMT are static during the entire remote loading process and located at z_{rl}. The oven is energized for a warmup period during which the photoionization lasers are blocked to reduce charging of the trap. Following the warmup period, a harmonic well is generated at z_0 and the photoionization lasers unblocked. After a brief wait time, the harmonic well is transported to z_{rl} and the PMT counts read out. If the counts exceed some threshold value, then an ion has been trapped at z_0 and transported to z_{rl}. If the PMT counts do not exceed the threshold value, then the harmonic well is returned to z_0 and the process is repeated excluding the warmup period. If an ion is not loaded within a predetermined number of attempts, the remote loading process will be aborted. Once an ion is trapped, the photoionization lasers are blocked and the oven turned off. Since both the "moving" beam and detectors are translatable, there are various approaches to remote loading; however, this method maximizes later chain loading success

in this system.

By combining single ion remote loading with a second static harmonic well for chain storage and the split/merge operation, it is possible to build ion chains of arbitrary length. There are now four relevant positions along the trap axis: z_0, where single ions are loaded from; z_{rl}, where single ions are loaded to; z_m, the merge point for the split/merge operation; and z_c where the chain is stored. In general, $z_0 < z_{rl} < z_m < z_c$ and a spatially symmetric split/merge operation is used resulting in $z_c - z_m = z_m - z_{rl}$. During chain building, typical values are $z_0 = 0$ μm, $z_{rl} = 851.5$ μm, $z_m = 930.5$ μm, and $z_c = 1009.5$ μm.

Single ion remote loading proceeds as normal except there is an additional static harmonic well at z_c with $\omega_z = 2\pi \times 500$ kHz, the single ion harmonic well adiabatically relaxes to match this well axial frequency at z_{rl}, and the "moving" beam is no longer static. When the single ion harmonic well is at z_0 (z_{rl}), the "moving" beam is aligned with z_c (z_{rl}). This arrangement allows the chain stored at z_c to be cooled momentarily while waiting to load an ion at z_0. Once the single ion well has been translated to z_{rl}, the "moving" beam is used to detect if an ion has been trapped. This procedure repeats until a single ion is loaded. After transporting a single ion to z_{rl}, the split/merge operation proceeds, combining the single ion well with the chain storage well at z_m. During the merge process, the "moving" beam follows the single ion well. An electric "shim" field, E_0, as in Eq. 4.1, is then used to tilt the combined potential towards z_c. This field is maintained as the wells are split causing all ions to go in the chain storage well towards z_c. The "moving" beam follows the chain well during this process. Once the chain storage well is at z_c, the single ion well is instantly transported (i.e. in a single waveform update step) to z_0 and the "shim" field is turned off. The camera, which has a sufficiently large field of view to see z_{rl}, z_m and z_c, then detects the number of ions in the chain. If the chain does not contain a sufficient number of ions, the process is repeated starting at the single ion remote loading stage; otherwise, the chain building process is complete. The chain building process is aborted if there are more than a predetermined number of merge failures. A merge failure occurs when the detected ion number of a chain has decreased following a merge attempt.

4.1.3 Ion Number Detection

Repeatable chain building requires reliable ion number detection. Single ions can be detected using the PMT but this approach is not well-suited for determining ion number. The larger spatial extent of a chain requires a larger aperture at the image plane just prior to the PMT resulting in a significant increase in noisy, background counts. Instead, the CCD camera is used to take chain images which are then transferred to the control computer for image processing. The control computer sums the pixel intensities in $\hat{x}$ and the resulting histogram is analyzed in $\hat{z}$.

To lessen image transfer times, the initial image width is reduced in $\hat{z}$. Following transfer, a number of image processing steps are performed to increase the eventual histogram's quality, such as dynamically reducing the image width in $\hat{x}$ to increase the signal-to-noise ratio and smoothing the image to provide sub-pixel resolution. After generating the intensity histogram $I(z)$, the second and third derivatives are calculated (Fig. 4.3). The basic principle of the detection algorithm is that positions in $\hat{z}$ with a local minimum in curvature, that is maximally concave down, represent the location of ions. This should be clear from Fig. 4.3a where each ion lines up with a sharp peak in the histogram. In order to quantify this and avoid detection of small, erroneous peaks due to shot noise, the following criteria are employed:

1. $\frac{d^3I(z)}{dz^3} = 0$; a critical point in $\frac{d^2I(z)}{dz^2}$ exists
2. $\frac{d^2I(z)}{dz^2} < A\sigma_2$; the curvature is negative (concave down) and not due to noise
3. $I(z) > I_0$; the peak is above some desired intensity threshold

In criterion 2, σ_2 represents the standard deviation of $\frac{d^2I(z)}{dz^2}$. A and I_0 are varied to maximize the reliability of the ion number detection protocol with the constraints that $A < 0$ and $I_0 > 0$. Once the ion positions are determined, a sum of gaussians centered at each ion location is fit to I_z to provide visual feedback. Detection reliability can be further increased with a few adjustments to the protocol: transformation of the harmonic chain storage well into an anharmonic well with 10 μm inter-ion spacing just prior to detection, use of a

cylindrical lens to broaden the "moving" beam waist to 120 μm in $\hat{z}$ to ensure all ions ($N \leq 8$) in the chain are illuminated uniformly, summing of multiple frames of camera data to reduce shot noise, and triggering of the camera exposure to coincide with the low-motion window of the cryostat's motional cycle.

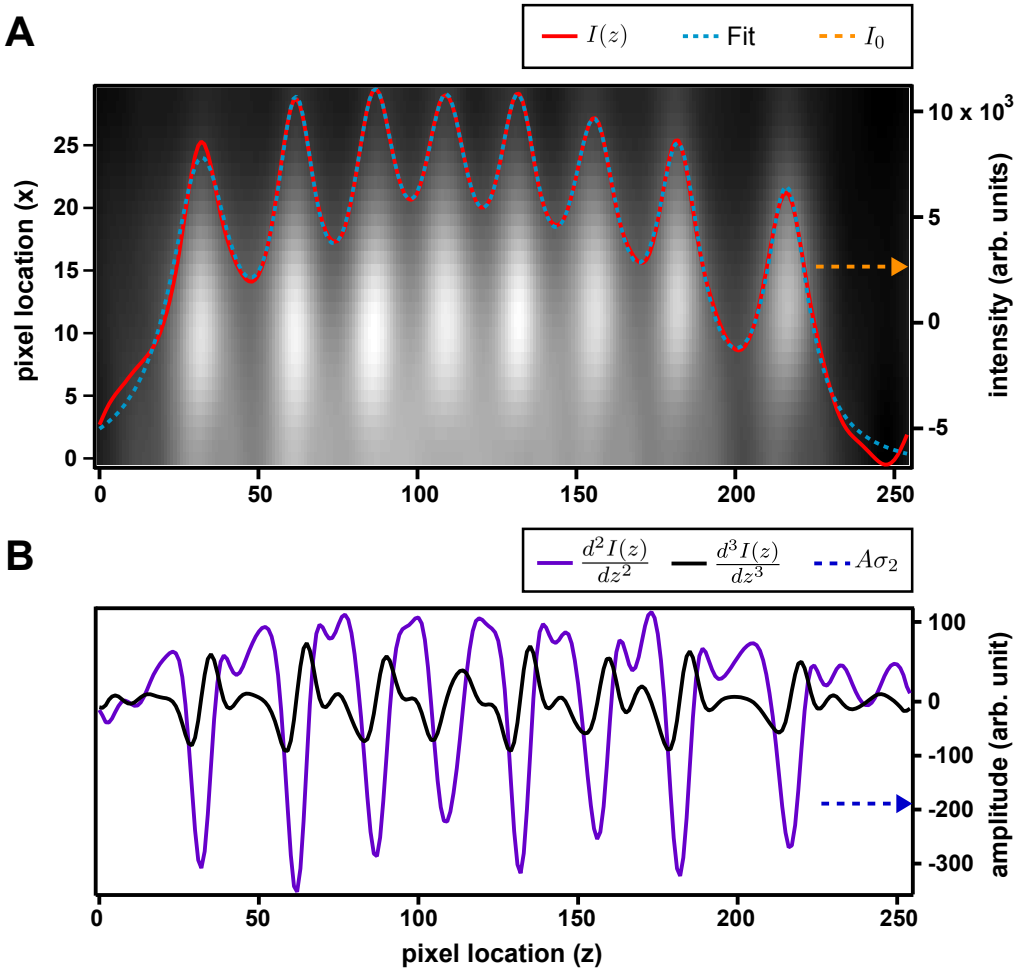

Figure 4.3: Ion number detection. (a) The image from the CCD camera following dynamic region of interest selection and smoothing. The intensity histogram, $I(z)$, and fit are overlaid while the histogram constraint, I_0, is labeled by an arrow on the right y-axis. The good agreement between $I(z)$ and the fit show that all 8 ions were unambiguously detected. (b) The histogram derivatives $\frac{d^2I(z)}{dz^2}$ and $\frac{d^3I(z)}{dz^3}$. The second derivative constraint, $A\sigma_2$, is labeled by an arrow on the right y-axis.

4.2 Trapping Lifetimes

In order to investigate the stability of ion chains in the trap, the method of Section 3.3 is used with some modifications. During loading, the chain building protocol is provided

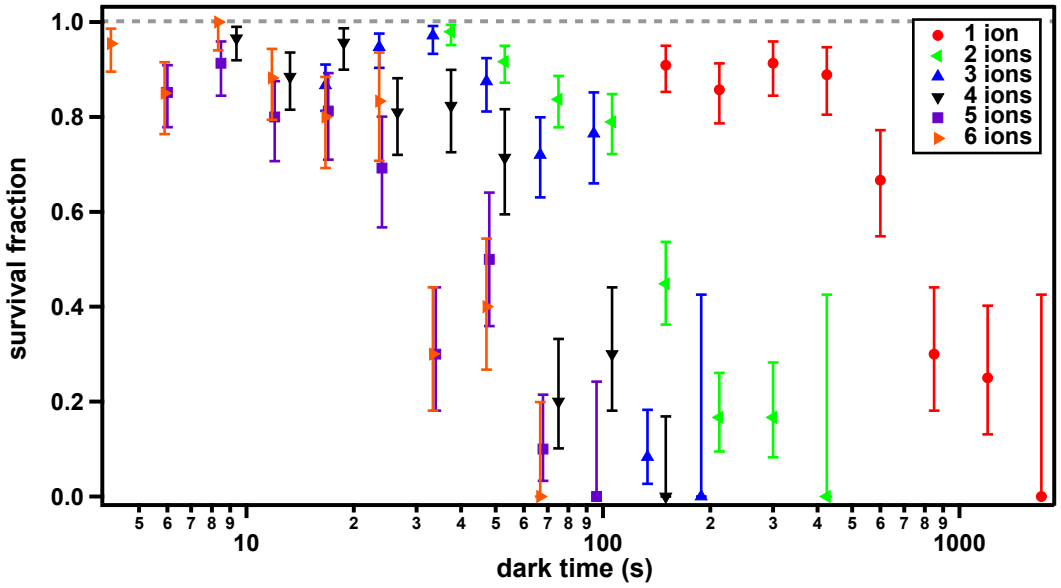

Figure 4.4: Chain lifetime in the absence of Doppler cooling in a harmonic ($\omega_z = 2\pi \times$ 500 kHz) well with calculated trap depth 25 meV axially and 32 meV radially.

with a desired ion number, N_0, and loading continues until $N \geq N_0$. The pause for oven cooldown is no longer temporally defined but instead dependent on the socket temperature. A loss of at least one ion counts as a failure. If any ions remain, the experiment continues from the shortest relevant dark time with the new ion number; otherwise, a chain with $N \geq N_0$ ions is built and the experiment continued. Using this modified procedure, data for chains that contain $N \leq 6$ ions are recorded (Fig. 4.4).

In order to quantify the chain trapping lifetimes, a simple collisional model is used. All collisions are assumed to share a common time constant, τ, and that exactly κ collisions are necessary to eject the ion, resulting in the following survival probability:

$$P(t) = (1 - (1 - e^{-t/\tau})^{\kappa}) \tag{4.2}$$

The exponential represents the chance of surviving a single collision and the exponentiated quantity represents the probability of ion loss given an exact number of collisions. Eq. 4.2 is used as a fitting function (Fig. 4.5a,b), the chain half-life, $t_{1/2}$, is calculated for each ion number, and 95% confidence bands are generated. The half-lives are determined to be 800, 200, 90, 60, 30, and 30 seconds for $1 \leq N \leq 6$ (Fig. 4.5c).

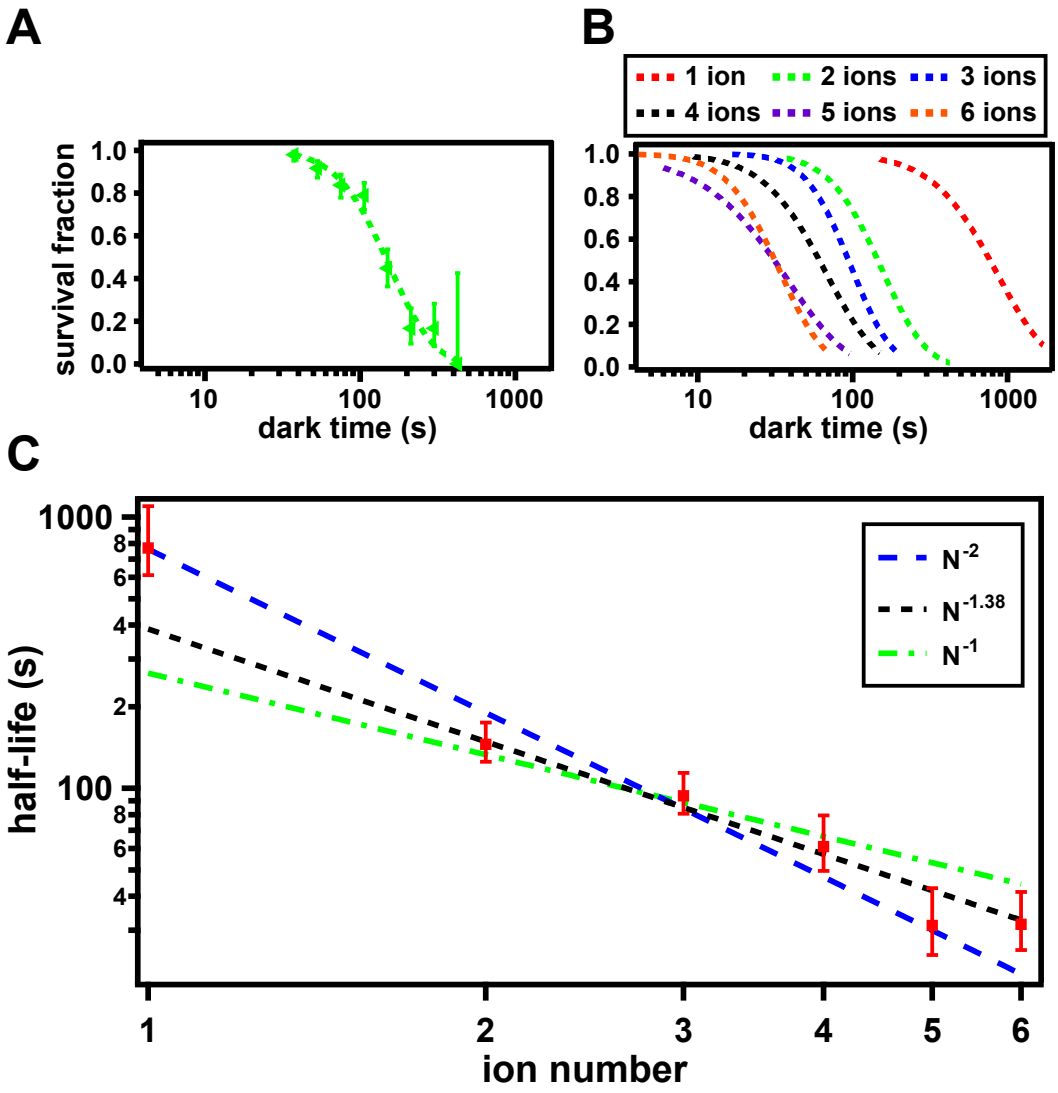

Figure 4.5: Chain half-life as a function of ion number. (a) An example fit of the $N = 2$ data using Eq. 4.2. (b) The fitted curves for $1 \leq N \leq 6$. (c) The resulting half-lives as a function of ion number. The data are fitted to a number of functions and details can be found in the text.

Table 4.1: Number of ions remaining following lifetime experiments.For the $N = 3$ (4) case, the remaining ion number was not always recorded such that only 187/205 (154/155) experiments are represented here. As the number of missing N' values is large for the $N = 3$ data, the percentage of failures with $N' = 1$ is not well known and thus not reported. Only a single data point is missing for $N = 4$, therefore the average of the two possible values, 44.4% and 47.2%, is reported.

Initial number	Remaining number N'							Percentage of failures
N	0	1	2	3	4	5	6	with $N' = 1$
1	29	107						
2	16	46	176					74.1
3	4	14	0	169				
4	16	16	0	3	119			45.8
5	22	16	0	0	3	91		39.0
6	17	8	0	0	0	3	99	28.6

4.3 Loss Channels

In order to better understand the lifetime data, four possible loss channels for both single ions and chains are considered with an eye to obtaining order-of-magnitude agreement with the data and appropriate scaling with N. These loss channels are oscillating electric fields and electric field gradients, inelastic ion-neutral collisions, elastic ion-neutral collisions, and elastic ion-ion collisions. The first three affect both single ions and chains while elastic ion-ion collisions are only relevant for $N > 1$. In light of this, the half-life data are fitted to a number of functions (Fig. 4.5c). If elastic ion-ion collisions are negligible, a fit of N^{-2} to all half-lives with a scale factor as the only free parameter may be a possibility. However, this seems unlikely and two fits are suggested for the $N > 1$ half-life data: N^{-1} with a scale factor as the only free parameter and $N^{-1.38(14)}$ where both the exponent and scale factor are free parameters. As a failure is defined as the loss of at least one ion, a scaling of N^{-1} might be expected as ions individually escape the trapping well; typically all or all but one ion are lost (Table 4.1) suggesting collective excitation and loss of the ions. For the $N > 4$ data, a single ion is occasionally lost during detection following the lifetime experiment. To better understand the behavior of an ensemble of N ions, a brief discussion of the one-component, nonneutral plasma and trap parameters will be useful.

4.3.1 Plasma and Trap Parameters

A neutral plasma consists of a collection of ionized atomic or molecular cores and unbound charges. Though the charges are unbound, they are not free due to the attractive potential of the cores. A one-component, nonneutral plasma can be formed if the attractive core potential is replaced by a collection of electric and/or magnetic fields such as in an ion trap. The nonneutral plasma can be characterized by the Coulomb coupling parameter which is the ratio of the electrostatic potential energy to the secular kinetic energy [89]:

$$\Gamma = \frac{1}{4\pi\epsilon_0}\frac{e^2}{a_{WS}k_B T_{sec}} = \frac{R_c}{a_{WS}} \tag{4.3}$$

The Wigner-Seitz radius, $a_{WS} = (3/4\pi\rho)^{1/3}$, represents the average inter-ion distance for a collection of ions of density ρ, T_{sec} is the temperature of the plasma due to secular motion, and the charge carriers are assumed to be singly ionized atoms. Alternatively, the Coulomb coupling parameter can be expressed in terms of the Landau length, R_c, which determines the characteristic length for ion-ion collisions within the plasma. An infinite, homogeneous plasma can exist in three distinct phases: a solid phase with long-range order and a crystalline structure ($\Gamma \gtrsim 173$), a liquid phase with a fluid-like local order ($1 < \Gamma \lesssim 173$), and a gas phase in which the ions only experience local interactions ($\Gamma < 1$) [90]. The Coulomb coupling parameter alone determines the time-independent order and can be used to compare the properties of plasmas with varying temperature and density.

For a finite nonneutral plasma of trapped ions, the ions form a Coulomb crystal in the solid phase. Upon heating, they transition to the liquid phase and are able to move more freely about their equilibrium positions. The ions enter the gas phase after sufficient heating and form a cloud where the individual ions are no longer localized to specific locations [91].

Plasmas of varying Γ can be generated by modifying experimental parameters. The ion density is dependent on the specifics of the trapping potential, number of ions, and the secular motional temperature. Modification of the laser cooling parameters will modify the initial secular motional temperature. The trapping potential is truly an RF pseudopotential and thus contains higher-order, non-harmonic terms that can directly couple the RF

electric field to the secular motion of the ions at specific trapping parameters [92]. When the resonance condition, $n_z\omega_z + n_{r1}\omega_{r1} + n_{r2}\omega_{r2} = \Omega_{RF}$, where n_z, n_{r1}, n_{r2} are integers, is satisfied, runaway heating can occur even during Doppler cooling. However, such resonances are easily avoided and not dependent on ion number so they should not contribute significantly to ion loss.

4.3.2 Oscillating Electric Fields and Field Gradients

Trapped ions couple strongly to electric fields and electric field gradients. An electric field resonantly drives ion motion at ω_{sec} by spatially shifting the potential minimum near the secular frequency. By modulating the effective trap spring constant, an electric field gradient parametrically drives ion motion at $2\omega_{sec}$. Wineland et al. [93] have calculated the dependence of the axial and radial center-of-mass heating rates on the electric field noise spectral density, $S_E(\omega)$, and electric field gradient noise spectral density, $S'_E(\omega)$ and found:

$$\dot{\bar{n}}_z = \frac{Ne^2}{4m\hbar\omega_z}\left[S_E(\omega_z) + \frac{\hbar}{4Nm\omega_z}S_{E'}(2\omega_z)\right] \tag{4.4a}$$

$$\begin{aligned}\dot{\bar{n}}_{rad} = &\frac{Ne^2}{4m\hbar\omega_{rad}}\left(S_E(\omega_{rad}) + \frac{\omega_{rad}^2}{2\Omega_{RF}^2}S_E(\Omega_{RF} \pm \omega_{rad})\right) \\ &+ \frac{e^2}{16m^2\omega_{rad}^2}\left(S_{E'}(2\omega_{rad}) + \frac{2\omega_{rad}^2}{\Omega_{RF}^2}S_{E'}(\Omega_{RF} \pm 2\omega_r ad)\right)\end{aligned} \tag{4.4b}$$

Though the two radial modes may have differing heating rates due to the secular motional frequency and axis orientation, their functional form is equivalent. The additional terms in Eq. 4.4b arise from noise on the RF drive coupling to the ion motion through fast oscillation of the radial potential. The single center-of-mass mode for each axis describes collective, in-phase motion of all ions. For all other motional modes, the ions undergo relative motion with respect to each other; therefore, they are insensitive to uniform electric field noise and only experience parametric excitation. Typically, the heating rate due to electric field gradients is insignificant compared to the heating rate due to electric field noise [93]. Due to these factors, the heating rate for each axis should be dominated by center-of-mass mode heating due to uniform electric field noise.

Comparison of the measured linear heating rates for a single ion (Fig. 3.9) to the well-depth gives trap lifetimes of 3.4, 17.8, and 119 hours for the upper radial, lower radial, and axial secular motional modes in the absence of Doppler cooling. These lifetimes are much longer than the observed half-life of 600 s for a single ion and 800 s for the $N = 1$ chain. Though the radial well-depths were identical for these two experiments, the axial well-depth was four times lower for the chain data. Since the half-life in the $N = 1$ chain case is not reduced by a factor of 4, heating of the axial modes by electric field and gradient noise is neglected as a possible loss channel.

By inspection, $\dot{\bar{n}}_{rad} \propto N$ does not match the observed chain half-life behavior for all N. In the absence of laser cooling and elastic ion-ion and ion-neutral collisions, the exchange of energy between motional modes is typically disallowed; however, anharmonicities of the radial trapping potential can couple the various radial motional modes. If the radial heating rate is dominated by the center-of-mass mode, the combination of elastic collisions and trap anharmonicites may allow redistribution of the ion secular energy across all $2N$ radial motional modes, reducing the perceived scaling of $t_{1/2}$ with N.

4.3.3 Inelastic ion-neutral collisions

Collisions of trapped ions with background neutral gas particles can result in both elastic and inelastic collisions. In the case of inelastic collisions, these can result in charge-exchange and chemical reactions. The potential composition of any background gas within the cryogenic vacuum volume must first be determined. As the walls within this volume are maintained at 50 K, the only compounds with appreciable vapor pressures[5] ($> 10^{-11}$ mbar) and thus a reasonable collision rate, are the constituents of atmospheric gas and the Noble gases.

In charge-exchange, $Ca^+ + M \rightarrow Ca + M^+$, where M is a neutral background gas particle. For charge-exchange to proceed, the ionization potential of the neutral species must be lower than the energy gained by the ion upon electron recombination [94]. It is clear from Table 4.2 that charge-exchange is forbidden for the selected species. The Noble gases all

[5]The vapor pressure of a compound is a gross overestimate of its partial pressure within the cryogenic vacuum volume; however, it allows easy identification of atomic and molecular species that may exist at appreciable partial pressures.

Table 4.2: Ionization potential (IP) of background gas species and potential chemical reactions with Ca^+.

Neutral	IP (eV)	Reaction	Reac. Ref.
Ca	6.1	-	-
H_2	15.4	$Ca^+ + H_2 \rightarrow CaH^+ + H$	[95]
N_2	15.6	-	-
O_2	12.1	$Ca^+ + O_2 \rightarrow CaO^+ + O$	[96]
H_2O	12.6	$Ca^+ + H_2O \rightarrow CaOH^+ + H$	[97]
CO_2	13.8	$Ca^+ + CO_2 \rightarrow CaO^+ + CO$	[97]
CH_4	12.6	-	-

have ionization potentials greater than 10 eV, prohibiting charge-exchange as well. For chemical reactions, only H_2, O_2, H_2O, and CO_2 are viable partners; however, all reactions are endothermic and have ∼eV energy barriers. As the lifetime data are taken in the absence of Doppler cooling, the ions are both in their electronic ground state and lack sufficient thermal energy to react.

4.3.4 Elastic Collisions

Elastic collisions between trapped ions and background neutrals can have either beneficial or deleterious effects depending on their relative mass and energy [98]. This process can be understood in the framework of Matheiu orbits and point collisions [99]. When the neutrals are much lighter or less energetic than the ion species, collisions cause small perturbations to the ion's Matheiu orbit and behave as a drag force on the secular motion. Helium buffer gas cooling of trapped ions is an excellent example of this behavior [100]. Alternatively, a much heavier or energetic neutral will cause a significant change in the ion's direction and velocity. This appears as a change in the phase of the Mathieu orbit allowing the RF trapping field to perform work on the ion and increase the secular motion [99]. For a constant background pressure of neutral particles, the ion-neutral collision rate is proportional to N. Ion-ion collisions can also occur though these *always* result in ion heating [99]. This heating is referred to as RF heating or micromotion interruption heating and is proportional to the density of ions within the trapping volume, the Coulomb logarithm, the Mathieu q parameter and the secular temperature [89].

As the N dependence of the chain half-life differs for $N > 0$ versus $N > 1$ data, it appears that elastic ion-ion collisions must play a role. For nonneutral plasmas in a macroscopic linear Paul trap, a rapid increase in temperature begins when the plasma transitions from the liquid to gas phase at $\Gamma \sim 1$ [89]. This transition corresponds to the ions having sufficient thermal energy that the Landau length is equal to the inter-ion distance; the sudden increase in ion-ion elastic collisions causes significant energy from the RF trapping fields to be transferred to the ions. This heating rate is abated by expansion of the Coulomb crystal into an ion cloud and evaporative cooling due to ion loss [89]. In the chain lifetime experiments, a single ion occasionally survives following a failure (Table 4.1) which may be attributed to the suppression of ion-ion heating following the loss of all other ions. For the $N = 2$ case, this effect seems to be heightened with 74% of failures resulting in a single ion remaining while for all other cases the probability of a single ion surviving decreases as N grows.

For small ion chains, the minimum inter-ion distance has been numerically determined to be [101]:

$$\Delta z_{min} = \left(\frac{1}{4\pi\epsilon_0} \frac{e^2}{m\omega_z^2} \right)^{1/3} \frac{2.018}{N^{0.559}} \tag{4.5}$$

By replacing a_{WS} from Eq. 4.3 with Δz_{min} and solving for T_{sec}, one finds the temperature of this phase change to be $T_{sec}(\Gamma = 1) = (2.29\ K)N^{0.559}$ for these experiments; the transition requires a higher temperature as ions are added to the plasma. An alternative definition of this temperature utilizes the ion number and trapping parameters [89]:

$$T_p = \frac{m\bar{\omega}^2}{4k_B} \left[\frac{3N}{4\pi} \frac{mR^4\Omega^2}{\epsilon_0 V_0^2} \right]^{2/3} \tag{4.6}$$

The trapping parameters include the RF drive voltage amplitude V_0, the angular frequency of the RF drive Ω_{RF}, and the effective radial ion-electrode distance R. The geometric mean of the three motional secular frequencies is $\bar{\omega}$. This definition results in $T_p = (1.64\ K)N^{2/3}$ which has a similar dependence to the previous expression. Though $T_{sec}(\Gamma = 1)$ and T_p for a few ions are both two orders-of-magnitude lower than the trap depth, it is unusual to observe ion clouds in small surface-electrode traps. In order to do so, constant loading of the trap is necessary [102]. This behavior supports the validity of rapid ion-ion heating and

loss following the transition from the liquid to the gas phase.

A combination of elastic ion-neutral and ion-ion collisions may explain the N dependence of the chain half-life data. While the plasma is in the strong coupling regime, $\Gamma \geq 1$, an ion-neutral collision may result in subsequent ion-ion collisions. Assuming both the ion-neutral collision rate and the change in temperature due to ion-ion collisions are proportional to N, the total change in temperature would be proportional to N^2. If the chain begins at the Doppler cooling limited temperature and is rapidly lost following the liquid to gas phase transition, then $t_{1/2} \propto T_{sec}(\Gamma = 1)/N^2 = N^{-1.441}$ or alternatively, $t_{1/2} \propto T_p/N^2 = N^{-4/3}$. These two expressions agree with the $N^{-1.38(14)}$ fit from Fig. 4.5c.

Heating due to electric field noise may be a suitable loss channel when the reduced temperature $T_{sec}(\Gamma = 1)$ is considered. Assuming no energy exchange between motional modes as in Sec. 4.3.2 and $N = 2$, this temperature is reached in 42, 217, and 442 seconds for the upper radial, lower radial, and axial motional modes. Though this appears promising, the scaling with N is not; the heating rate is proportional to N and $T_{sec}(\Gamma = 1) \propto N^{0.559}$, resulting in $t_{1/2} \propto N^{0.559}/N = N^{-0.441}$ which does not agree with the $N > 1$ fits.

4.4 Future Work

An inconvenient characteristic of the cryogenic system is the tendency for layers of material to cryosorb onto the laser and fluorescence windows. As discussed in Section D.3, this was sufficiently problematic that experiments had to be halted and the cryostat returned to room temperature so that all windows could be cleaned. Due to this interruption, the various loss channels could not be fully investigated.

In order to more accurately determine the chain half-lives, future experiments will require an increased number of trials per dark time and higher temporal resolution. To further map the scaling of chain lifetime with ion number, N could be extended to larger numbers. However, extension to arbitrary N is not possible due to the vanishing separation between chain lifetime curves as N increases, the finite single ion half-life, and technical limitations related to loading long chains in the Gen IIc surface-electrode trap. A reasonable goal would be to extend the data to $N = 10$. However, such expanded data collection will take

significant time and other experiments may elucidate the importance of the various loss channels.

Additional heating rate data for the three single ion secular motional modes should be collected. Though the axial secular motional mode's heating rate appears linear within the first 20 ms, both of the radial heating rates appear to have a higher order time dependence (Fig. 3.9). Taking heating rate data for longer delay times would allow a better characterization of the departure of these heating rates from linearity. If necessary, higher order secular motional sidebands or the Doppler recooling method should be used for heating rate determination at longer delay times. Note the Doppler recooling method will measure the total heating rate of all three modes. Since the single ion heating rates are only sensitive to electric field noise, electric field gradient noise, and ion-neutral collisions, they can provide baseline data for these loss channels. For example, the electric field noise density can be determined for a number of secular frequencies by adjusting trapping parameters. This determination is straightforward for the axial mode as the heating rate is dominated by noise at a single frequency. However, the heating of each radial mode is proportional to three frequencies. If noise is injected into the helical resonator input, the heating rate due to direct excitation of the ion's motion at ω_{rad} and due to the oscillation of the radial trapping potential at $\Omega_{RF} \pm \omega_{rad}$ can be more easily compared. Glancing collisions may be detectable by measuring heating during this time period using the sideband method.

Ion-neutral collisions can be investigated using single ion heating rates, the axial double well trapping potential, and multi-isotope chain reordering. As a head-on collision with a 4 K H_2 molecule will provide meV of energy to a trapped $^{40}Ca^+$, a collision should be detectable by a sudden increase in ion temperature. For example, an experimental cycle consisting of Doppler cooling an ion, allowing it to heat in the dark for 10 ms, and a Doppler recooling measurement can be utilized. As a typical Doppler recooling measurement is insensitive to a single phonon increase, no heating will be measured in the absence of a collision. However, if a head-on collision as previously described has taken place, the now higher ion temperature will result in obvious Doppler recooling. By repeating this experimental cycle, sufficiently energetic collisions can be detected and a collision rate calculated. Furthermore,

the temperature following the collision can be extracted from the Doppler recooling data and used to determine the average collision energy.

An axial double well potential could be used for the same purpose. This potential can be created by combining a quartic and quadratic potential as in the case of the split/merge transport operation (Fig. 4.1b). The height of the barrier between the wells can be carefully adjusted to detect collisions of varying energy. An experimental sequence would begin with an ion in the right well. The cooling lasers would then be extinguished for a short time during which a collision may take place. Following this dark time, the Doppler cooling lasers would be reapplied and the location of the ion determined. If a collision of sufficient energy has taken place, the ion has an equal chance of being in either well; otherwise, the ion will still be in the right well. By measuring the probability of finding the ion in the left well for a number of barrier heights, it should be possible to calculate the ion-neutral collision rate for a given collision energy.

The final method would utilize a two isotope, two ion chain consisting of a $^{40}Ca^{+}$ and a $^{44}Ca^{+}$ ion. The cooling lasers would be tuned to only cause the $^{40}Ca^{+}$ to fluoresce. During this experiment, the ions would be continuously Doppler cooled and the position of the bright ion monitored. Whenever an ion-neutral collision with energy greater than the equilibrium Coulomb repulsion energy takes place, the ions may swap position. By adjusting the axial secular frequency, the Coulomb repulsion energy and thus the collisional energy threshold can be modified. It should be possible to extract a collision energy dependent rate from these data.

If ion-neutral collisions are the dominant loss channel in the single ion case, a reduction in background gas pressure should improve the single ion half-life. As vacuum in a cryostat can vary across short distances due to localized pumping speeds, the heatsink on the fanout PCB has been converted into a charcoal getter. This sorb was not in place for the chain lifetime experiment. If future single ion lifetime measurements are increased following the installation of the getter, it may support ion-neutral collisions as the primary loss channel for single ions.

The heating rate of the various motional modes of an N ion chain are dependent on ion

number (Eq. 4.4) and experience ion-ion heating for $N > 1$. By investigating the heating rates for these chains, the relative contributions of electric field noise and elastic ion-ion collisions can be determined. It is assumed that electric field gradient noise heating will be minimal. The center-of-mass mode heating rate should be proportional to N whereas the relative modes should all have highly suppressed heating rates and no N dependence. The electric field noise density for the axial center-of-mass mode can be determined from the $N = 1$ data. If heating rate data are recorded for the $N = 2$ case, an increase in the center-of-mass mode heating by more than a factor of two may be a signature of heating due to ion-ion collisions. As the heating rate on the relative motional mode is expected to be low, any detected heating rate may also be due to ion-ion collisions. For electric field noise, $\dot{\bar{n}} \propto S_E(\omega)/\omega$. For a single ion, it has previously been shown that $\dot{\bar{n}} \propto \omega^{-2}$, and thus the electric field spectral density exhibits pink noise [43]. As the specifics of each ion trap as well as its RF and DC electronics differ, this electric field noise frequency spectrum dependence may not be universal. By comparing the frequency dependence of single ion and chain heating rates for a trap, it may be possible to detect ion-ion heating due to deviation of the chain data from the single ion data.

Extending such experiments to larger N would allow the N dependence of the various motional mode heating rates to be extracted. As the secular frequency of each axial motional mode differs by less than 2% for $N \leq 10$ [101], the electric field spectral noise density should be nearly constant. Comparison of a given motional mode's heating rate for a number of N values should allow the determination of heating effects that are not linearly dependent on N such as ion-ion or ion-neutral collisions.

Even if experiments are limited to small values of N such that there are not sufficient data to carefully determine the N dependence of the heating rates, the relative contributions of electric field noise, ion-ion elastic collisions, and ion-neutral elastic collisions may be determined. Electric field noise heating can be increased by applying an appropriate frequency voltage to a DC trap electrode, an auxiliary conductor, or the RF rails. The Butterworth filters on the DC voltage lines will strongly attenuate any injected noise above 40 kHz applied to a DC trap electrode, limiting the efficiency of this method. The only

conductor in close proximity to the ion trap is the copper ground screen. It is connected to an RF feedthrough on the upper OVC with no intermediate filtering. By applying an appropriate frequency signal to this screen, arbitrary electric field noise limited by the specifications of the in-vacuum coaxial cable could be injected. Coupling to motional modes perpendicular to the trap surface would be strongest. The final trap features useful for noise injection are the RF rails. As the helical resonator would filter out any direct excitation of ion motion, the RF drive signal would need to be modulated at the excitation frequency by a RF mixer or a directional coupler.

In order to increase the contribution of ion-ion heating, the Mathieu q of the trapping pseudopotential can be modified. The temperature increase of the plasma due to ion-ion elastic collisions is directly proportional to the average energy gained due to a collision, $\bar{\epsilon} \approx \frac{2}{3}(1+2q^{2.24})$ [89]. The only available method for changing q is varying the RF trapping voltage. There is evidence that increased q results in decreased stability of ion chains in this apparatus. For example, with $q = 0.266$ it is very difficult to build a $N = 7$ ion chain and single ions are occasionally ejected from the trap even in the presence of Doppler cooling. If q is relaxed to a value of 0.243, chains of up to $N = 8$ can be loaded without particular difficulty and Doppler cooled ions are rarely lost. As the energy gained in an ion-ion collision is only weakly dependent on q, the reduced chain stability may indicate the growth of some other loss channel such as rapid heating due to resonances as described in Section 4.3.1. Care must be taken when decreasing q as this will also lower the radial well-depth. The ion-ion heating is also proportional to the excess micromotion of the trapped ions. By intentionally applying a linear electric field along $\hat{x}$ or $\hat{y}$ and decompensating the ion, the contribution of ion-ion elastic collisions to the heating rates can be increased.

The contribution of ion-neutral collisions have been previously investigated for single ions in a room temperature trap and found to minimally affect ion heating [44]. However, the lack of secondary ion-ion interactions in a single ion system may explain this behavior. Repeating such an experiment with an ion chain may result in noticeable heating. As the vacuum space in this apparatus is cryopumped, there is no mechanical or electrical pumping system that can be easily switched off to raise the chamber pressure and thus increase the

rate of ion-neutral collisions. Instead, a leak valve with an attached capillary tube can be used to deliver any desired gas to the ion trap. This approach would allow precise control of gas species and flow but significant work would be required to incorporate such a setup into the cryogenic apparatus. There are two methods which do not require any modification to the system: energizing a heater attached to one of the getters to increase the temperature local to the ion trap or using the oven to provide a limited neutral calcium background flux. Heating the cryocooler's second stage, the spacer block, and the PCB will result in thermal desorption and thus an increased local background gas pressure.

CHAPTER V

CONCLUSION AND OUTLOOK

This work has detailed the design, construction, and characterization of a cryogenic surface-electrode ion trapping apparatus. The cryostat is a simple, modular system with excellent vacuum, large optical access, and rapid trap turnaround utilizing a commercial pulse tube cryocooler and an uncomplicated vibration isolation system. The system was characterized using single ions and order-of-magnitude improvements in ion heating rate and lifetime compared to an identical room-temperature surface-electrode ion trap were attained. These results demonstrate that two of the primary design goals, suppression of anomalous heating and reduction of the background gas pressure, have been achieved. Compensation of a single ion along all three spatial axes was demonstrated across the trap using a novel compensation method. An automated procedure employing transport waveforms enabled the building of small linear ion crystals. The system was then used to study the stability of these crystals for $N \leq 6$ by recording lifetime measurements in the absence of Doppler cooling and extracting half-lives. The N dependence of a number of possible ion loss channels have been considered.

5.1 Outlook

Despite the increased optical access provided by a custom cryostat, laser access to most surface-electrode traps is limited by wirebonds. For example, the Gen IIc is designed to allow laser access along the eight cardinal directions. Additionally, the typical dimensions of the trap die are much larger than the actual trapping region restricting the amount of angular deviation possible along these directions. To minimize scattered light off the edge of the trap, a typical 397 nm cooling beam is restricted to a 30 μm beam waist at the center of the trap die. To address these issues, GTRI and Honeywell International are currently collaborating on a full optical access ion trap utilizing a ball-grid-array (BGA). Wirebonding would no longer be necessary as through-the-wafer vias would connect the electrodes to the BGA while the large surface area capacitors of traditional design would be

replaced by trench capacitors. Previously, much of the trap die was necessary to incorporate these on-chip capacitors and route electrode traces to the perimeter for wirebonding. As this would now be superfluous, the BGA trap will be 1/3 of the length along the trap axis and 1/9 the width perpendicular to the trap axis allowing much more tightly focused beams with minimal scatter. The cryogenic system presented here would be uniquely suited to maximally utilize these trap features due to the wide-angle optical access and lens stack laser injection.

In the $^{40}Ca^{+}$ optical qubit, two of the most significant decoherence sources are ion heating and magnetic field fluctuations [64]. As the experimental region is surrounded by low temperature, high residual-resistivity-ratio copper, AC magnetic field noise should be reduced due to eddy current shielding [103]. A 65-fold suppression of such noise at 60 Hz has been measured in the cryogenic surface-electrode ion trap. Mitigation of both magnetic field noise and the ion heating rate is promising; however, the vibration of the system requires slow, triggered operation of the system and only allows a limited 300 ms window for experimentation. Despite these limitations, coherent quantum operations in the form of compensating pulse sequences on a single ion have been demonstrated [104]. Ideally, these same pulse sequences could be demonstrated with strings of 2 or 3 ions. Beyond that, the extension of coherent operations to arbitrary ion number chains within the system would be desirable. Currently, most quantum computation efforts in surface-electrode ion traps have taken place at cryogenic temperatures and with few ions [51, 105, 106]. Many cutting-edge quantum computation experiments still take place in macroscopic linear ion traps due to their vastly reduced ion heating rates and well-behaved dynamics. Achieving such operations in this system would be a lofty goal.

Another advantage provided by a cryogenic system is the reduction of blackbody radiation incident upon the trapped ion. At room temperature, electronic transitions cannot be driven by blackbody radiation due to the vanishing spectral density at the 10^{16} Hz frequencies of interest. For this reason, the blackbody radiation spectrum is of little concern for non-precision measurements with atomic ions. However, rotational ($10^{9} - 10^{10}$ Hz) and

vibrational ($10^{12} - 10^{14}$ Hz) transitions of molecular ions may be driven by room temperature blackbody radiation [107]. Such blackbody mediated transitions result in the molecular rovibrational population being distributed according to the ambient temperature. The translational energy of molecular ions can be reduced via sympathetic cooling by co-trapped atomic ions but the mismatch between the trapped ion secular frequencies ($10^4 - 10^6$ Hz) and the molecular ion internal transition frequencies results in rovibrationally hot ions [108]. There have been a number of proposals to cool the internal states of molecular ions with the ultimate goal of generating a molecular ion in the absolute ground state. Many of these rely on using molecular ions with large vibrational constants, such as low mass diatomic hydrides, that will be in the vibrational ground state at room temperature. Rotational cooling of sympathetically cooled molecular ions has been demonstrated with blackbody-mediated optical pumping [109, 110] but complete rovibrational ground state occupation has not been achieved. By performing such experiments in a cryogenic ion trap, the initial distribution of population amongst the rotational levels is much narrower which aids such optical cooling methods and may eliminate their necessity for certain molecular species. Direct laser cooling of specific molecular ions [111] requires preparation of the ion in a specific rotational state and a cryogenic environment can serve this purpose. Finally, coupling of the rotational and translational degrees of freedom of trapped molecular ions via frequency combs [112, 113] should allow rovibrational spectroscopy, state preparation, and cooling. Again, this technique is aided by occupation of the vibrational ground state and a reduced population distribution amongst the rotational levels. The extension of these techniques to heavier diatomic ions as well as polyatomic ions will surely benefit from the use of a cryogenic ion trap to limit population spread amongst rovibrational levels. The cryogenic ion trapping system detailed within this work can be adapted for such experiments due to its flexibility and modularity.

APPENDIX A

GEN IIC AUXILLIARY INFORMATION

The GTRI Gen II linear trap operational manual [67] is an excellent resource for information regarding the Gen II surface-electrode trap. Additional fabrication information as well as specific information about the Gen IIc derivative can be found in Doret *et al.* [39].

In the trapping region (Fig. A.1), there are 2 asymmetric RF electrodes, 44 segmented DC electrodes ($\#5-48$), a split center electrode ($\#3$), and 2 DC rotation electrodes ($\#2, 4$). The RF electrodes generate the pseudopotential for radial confinement. The spatial asymmetry of the electrodes perpendicular to the trap axis naturally rotates the RF quadrupole axes by $\sim 25°$.

The segmented DC electrodes can be utilized as long DC "rails" by applying a uniform voltage to all electrodes with even or odd labels. The combination of these DC "rails" with the DC rotation electrodes and electrode #3 allow the creation of arbitrary uniform, linear, and quadrupolar DC electric fields in $\hat{x}$ and $\hat{y}$ at the RF null. The quadrupolar DC electric field is of special interest as it can be used to rotate the secular motional axes of the trap.

Axial confinement is provided by application of voltages to the appropriate segmented DC electrodes. If an ion is to be confined at the center position of a DC electrode, then a minimal set of three electrodes is necessary to create the harmonic potential. Additional electrodes can be utilized to smooth the potential or introduce higher order terms. For transport along the trap axis, waveforms are indexed according to the position in μm from the center of the trap loading slot (Fig. A.1).

GTRI traps are packaged to meet the MUSIQC 48 pin wiring standard for planar ion traps. This standard accounts for 48 controls, the RF send, the RF return, and 2 control grounds to be transmitted through a 100-pin ceramic pin grid array (CPGA) carrier. The mapping between the Gen IIc trap's 47 DC electrodes and the CPGA pins $1-50$ can can be found in Table A.1 while the mapping to CPGA pins $51-100$ can be found in Table A.2.

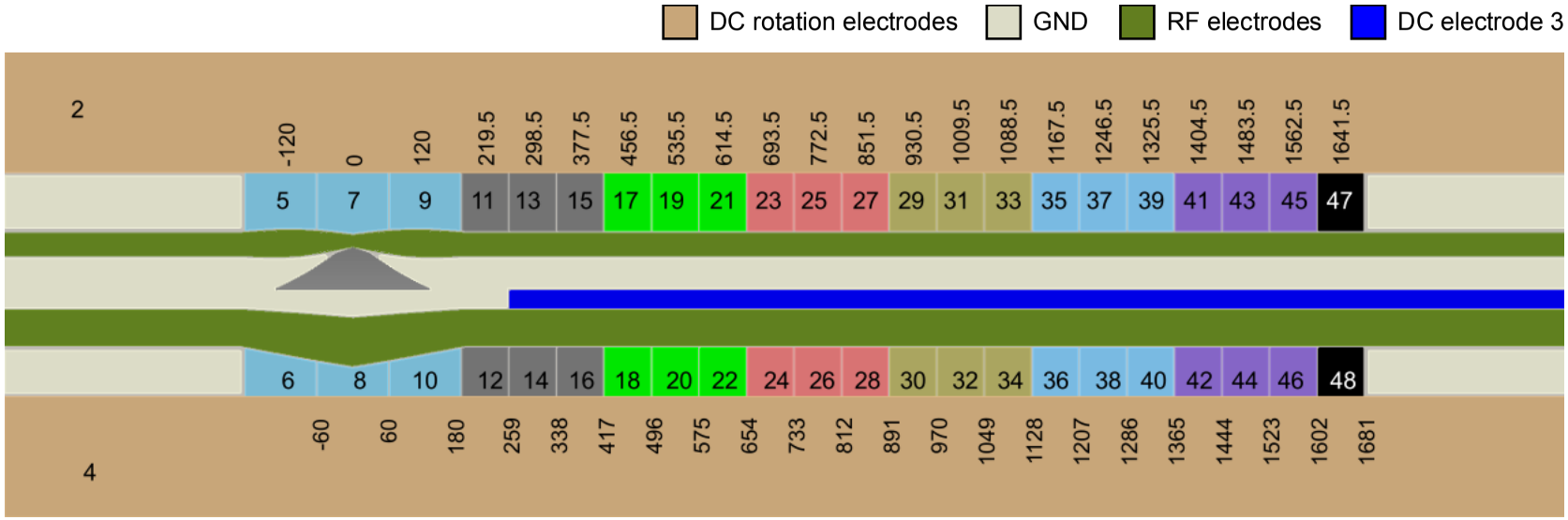

Figure A.1: Gen IIc electrode positions. All DC electrodes are numerically labeled for reference. The labels above the odd-numbered DC electrodes denote the center position (μm) of that electrode along $\hat{z}$. The labels below the even-numbered DC electrodes denote the position (μm) of the interface between two electrodes.

Table A.1: Mapping of Gen IIc DC electrodes to the CPGA pads $1-50$. The label GII_* is used to represent a DC electrode, e.g. electrode 3 is GII_3. Each DC electrode of the Gen IIc is wirebonded to a CPGA pad (Pad). That pad is then internally routed through the CPGA to a socket pin (Pin). These socket pins interface with an external socket for the application of DC voltages. The RF send is represented by RF and the RF return is represented by RF RET. In the MUSIQC 48 pin wiring standard, any excess pads may be mapped to existing control or ground lines. When this is the case, the entry in the Gen IIc DC column will be in parentheses.

Pad	Pin	Gen IIc DC	Pad	Pin	Gen IIc DC
1	B2	-	26	M2	-
2	B1	-	27	N2	-
3	C2	-	28	M3	-
4	C1	GII_15	29	N3	GII_18
5	D2	(GII_15)	30	M4	(GII_18)
6	D1	GII_13	31	N4	GII_20
7	E2	GII_11	32	M5	GII_22
8	E1	GII_9	33	N5	GII_24
9	F3	-	34	L6	(GII_26)
10	F2	GII_07	35	M6	GII_28
11	F1	GII_05	36	N6	GII_26
12	G2	RF RET	37	M7	-
13	G3	(GND)	38	L7	GND
14	G1	RF	39	N7	-
15	H1	GII_06	40	N8	GII_32
16	H2	GII_08	41	M8	GII_30
17	H3	-	42	L8	(GII_32)
18	J1	GII_10	43	N9	GII_34
19	J2	GII_12	44	M9	GII_36
20	K1	GII_14	45	N10	GII_38
21	K2	(GII_16)	46	M10	(GII_40)
22	L1	GII_16	47	N11	GII_40
23	M1	-	48	N12	-
24	L2	-	49	M11	-
25	N1	-	50	N13	-

Table A.2: Mapping of Gen IIc DC electrodes to the CPGA pads $51 - 100$. The label GII_* is used to represent a DC electrode, e.g. electrode 3 is GII_3. Each DC electrode of the Gen IIc is wirebonded to a CPGA pad (Pad). That pad is then internally routed through the CPGA to a socket pin (Pin). These socket pins interface with an external socket for the application of DC voltages. The RF send is represented by RF and the RF return is represented by RF RET. In the MUSIQC 48 pin wiring standard, any excess pads may be mapped to existing control or ground lines. When this is the case, the entry in the Gen IIc DC column will be in parentheses.

Pad	Pin	Gen IIc DC	Pad	Pin	Gen IIc DC
51	M12	-	76	B12	-
52	M13	-	77	A12	-
53	L12	-	78	B11	-
54	L13	GII_42	79	A11	GII_39
55	K12	(GII_42)	80	B10	(GII_39)
56	K13	GII_44	81	A10	GII_37
57	J12	GII_46	82	B9	GII_35
58	J13	GII_48	83	A9	GII_33
59	H11	-	84	C8	(GII_31)
60	H12	GII_04	85	B8	GII_29
61	H13	GII_03	86	A8	GII_31
62	G12	(GND)	87	B7	-
63	G11	-	88	C7	GND
64	G13	(GND)	89	A7	-
65	F13	-	90	A6	GII_25
66	F12	GII_02	91	B6	GII_27
67	F11	-	92	C6	(GII_25)
68	E13	GII_47	93	A5	GII_23
69	E12	GII_45	94	B5	GII_21
70	D13	GII_43	95	A4	GII_19
71	D12	(GII_41)	96	B4	(GII_17)
72	C13	GII_41	97	A3	GII_17
73	B13	-	98	A2	-
74	C12	-	99	B3	-
75	A13	-	100	A1	-

A.1 Motional Secular Frequencies of a Single Trapped Ion

A number of useful parameters can be extracted from a trapped ion's motional secular frequencies. Traditionally, GTRI has designed trapping waveforms with an axial secular frequency of $\omega_z = 2\pi \times 1$ MHz for a single trapped $^{40}Ca^{+}$ ion. Thus, if one "unit" of this waveform is applied, then a 1 MHz well will be formed. Since $\omega_z \propto \sqrt{V_{DC}}$, if two units of this waveform are applied, a 1.44 MHz well will be formed.

The radial motional frequency of an ion trapped in a RF quadrupole electric field is:

$$\omega_{RF} = \frac{eV_0}{\sqrt{2}\Omega_{RF} m R^2} \tag{A.1}$$

The RF drive voltage amplitude is V_0, Ω_{RF} is the angular frequency of the RF drive, and R is an effective distance. For the Gen IIc surface-electrode trap, $R = 145$ μm over the loading slot and $R = 133$ μm outside the load zone [67]. Upon the application of DC potentials, the radial motional frequencies will be modified. For the axial harmonic well, this is a consequence of Laplace's equation which requires the axially confining potential to be radially anti-confining. The application of a radial DC quadrupole will strengthen the RF pseudopotential along one secular axis and weaken it in the other. The net consequence are these modified, non-degenerate radial secular motional frequencies:

$$\begin{aligned} \omega_{r1}^2 &= \omega_{RF}^2 - (\omega_z^2 + \Delta\omega_r^2)/2 \\ \omega_{r2}^2 &= \omega_{RF}^2 - (\omega_z^2 - \Delta\omega_r^2)/2 \end{aligned} \tag{A.2}$$

The splitting of the radial modes is characterized by $\Delta\omega_r$ and the axial secular frequency is ω_z. If all three secular motional frequencies of a single ion are measured, the radial motional frequency due to RF drive alone and the splitting frequency can be calculated:

$$\begin{aligned} \omega_{RF}^2 &= \frac{\omega_{r1}^2 + \omega_{r2}^2 + \omega_z^2}{2} \\ \Delta\omega_r^2 &= \omega_{r2}^2 - \omega_{r1}^2 \end{aligned} \tag{A.3}$$

With ω_{RF} known, it is possible to calculate the peak RF voltage being applied to the trap. Additionally, the Matheiu parameters of trapping potential can be determined. In the case that $q \ll 1$ and $a \sim 0$, the secular frequencies for any axis i can be written in the following

form [63]:

$$\omega_i^2 = \left(a_i + \frac{q_i^2}{2}\right)\frac{\Omega_{RF}^2}{4} \tag{A.4}$$

The Matheiu parameter q is associated with the oscillating potential and thus ω_{RF}, while the a parameter is associated with the axial DC potential as well as the DC quadrupole term. With this in mind and comparing Eq. A.4 with Eq. A.2, one finds:

$$\begin{aligned} a_{r1} &= \frac{-2(\omega_z^2 + \Delta\omega_r^2)}{\Omega_{RF}^2} \\ a_{r2} &= \frac{-2(\omega_z^2 - \Delta\omega_r^2)}{\Omega_{RF}^2} \\ a_z &= \frac{4\omega_z^2}{\Omega_{RF}^2} \\ q_{r1} &= q_{r2} = \frac{2\sqrt{2}\omega_{RF}}{\Omega_{RF}} \\ q_z &= 0 \end{aligned} \tag{A.5}$$

APPENDIX B

ELECTRICAL CONNECTION DIAGRAMS

B.1 DC Electrical Connections

The DC electrical connections are split into four groups. Each group is color-coded and all connections, cables, and wire bundles, both internal and external, are marked either with colored heatshrink or by a dot of paint. Each color is associated with a quadrant of the CPGA (Table B.1) and each wire bundle is attached to the PCB at a specific header (Fig. B.1a). The numbering system at each header is known as the board label and directly corresponds to the CPGA pad, i.e. board label 1 is connected to CPGA pad 1, board label 2 is connected to CPGA pad 2, etc. CPGA pads 13, 38, 63, and 88 are directly tied to the PCB ground through the socket and thus connections for these pads do not exist in the wire bundles. As the PCB traces for quadrant 2 are on the opposite face of the board and approach the socket pins from the inside face of the socket, its board labeling is reversed with respect to the other headers.

For each quadrant, DC signals are delivered by a multi-part wire bundle as discussed in Section 2.2.5. The bundle consists of three sections: one section is heat sunk at 300 K, one at the first stage of the cryocooler (40 K), and one at the second stage of the cryocooler (4 K). The wire bundles are connectorized with 26-pin rectangular headers at all stages except the vacuum interface where Fischer connectors are used. The Fischer connector pin numbering is recorded in Fig. B.4 and the 26-pin connector for quadrant 1 and 2 is labeled in Fig. B.2. Due to an error in the fabrication of quadrant 3 and 4's wire bundles, the mapping between 26-pin connectors is not straight-through (Fig. B.3). On the room side of the Fischer connector, the DC voltages are provided via a D-sub 25 to Fischer cable. The mapping from the carrier pads to the room side D-sub 25 for each quadrant can be found in Tables B.2, B.3, B.4, and B.5. There is no path between pin 7 of the D-sub 25 connectors and the trap; it is used as the ground pin for the cable shielding. CPGA pad's 12 and 14 are for the

delivery of RF voltage.

Table B.1: CPGA quadrants.

Color	Quadrant	Carrier Pad
Yellow	1	1-25
White	2	26-50
Blue	3	51-75
Red	4	76-100

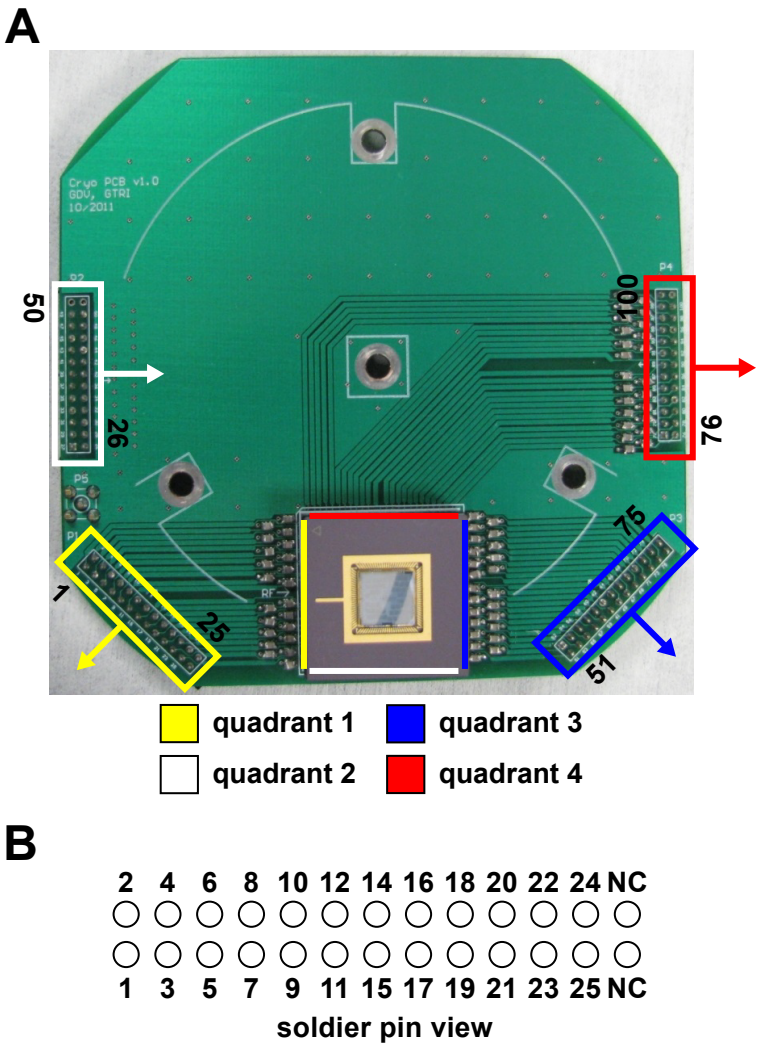

Figure B.1: PCB with DC quadrants. (a) DC voltages are supplied to the PCB via four polarized rectangular headers. Each header is color-coded and the orientation of the key is marked with an arrow. The numbers labeling each quadrant indicate the CPGA pad (Appendix A) that pin is connected to. A line of the appropriate color labels each quadrant of the CPGA. (b) The board labels for DC electrode quadrant 1 (NC = not connected). These indicate which carrier pad each header pin is connected to. The header pin numbering for quadrant 3 (4) is the same but with 50 (75) added to each label. The board numbering for quadrant 2 is reversed and 25 is added to each label. This is a solder pin (back) view which matches the side visible in part a. Note that pin 13 is skipped (see text for details).

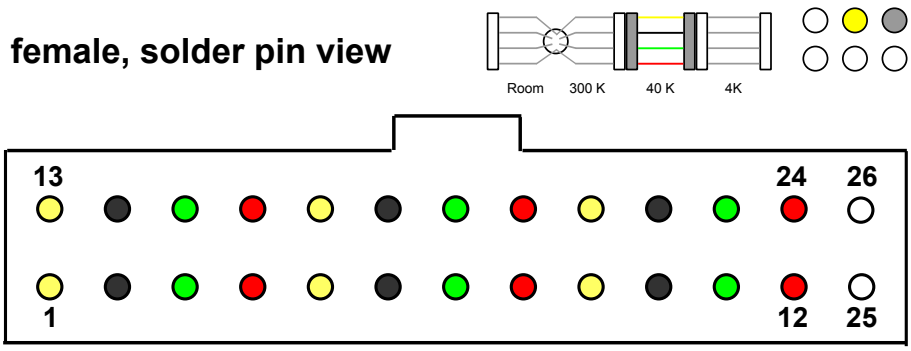

Figure B.2: 26-pin rectangular header numbering for quadrants 1 and 2. All connectors share the same straight-through mapping. Pin color represents the color of the Lakeshore quad-twist phosphor-bronze wire used.

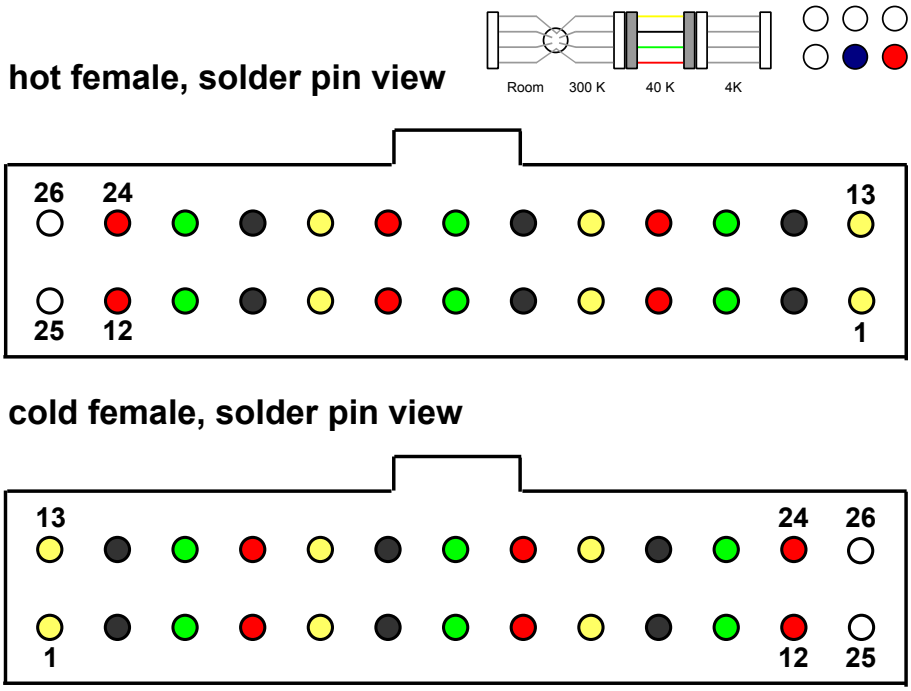

Figure B.3: 26-pin rectangular header numbering for quadrants 3 and 4. Due to an error between the Fischer connector and 26-pin connector in the 300 K section, a straight-through mapping is no longer possible and has been replaced with this mapping. The "hot" side represents the female connector on the 300 K to 40 K end of the 40 K section with the modified mapping. All other female connectors follow the "cold" side mapping. Male connectors are merely horizontally flipped with respect to female connectors. Pin color represents the color of the Lakeshore quad-twist phosphor-bronze wire used.

Table B.2: Electrical mapping of DC quadrant 1 (Yellow). CPGA pads (Pad) are mapped from the CPGA pin (Pin) and PCB headers (Board) through the 26-pin (26-pin) and Fischer connector (Fischer) to the room side D-sub 25 (DB25) connector. CPGA pad's 12 and 14 are for the delivery of RF voltage and thus are not labeled here. Socket pin 13 is grounded. NC = not connected.

Pad	Pin	Board	26-pin	Fischer	DB25
1	B2	1	13	13	1
2	B1	2	1	1	14
3	C2	3	14	14	2
4	C1	4	2	2	15
5	D2	5	15	15	3
6	D1	6	3	3	16
7	E2	7	16	16	4
8	E1	8	4	4	17
9	F3	9	17	17	5
10	F2	10	5	5	18
11	F1	11	18	18	6
-	-	-	6	6	19
13	G3	13	NC	NC	7
-	-	-	7	7	20
15	H1	15	19	19	8
16	H2	16	8	8	21
17	H3	17	20	20	9
18	J1	18	9	9	22
19	J2	19	21	21	10
20	K1	20	10	10	23
21	K2	21	22	22	11
22	L1	22	11	11	24
23	M1	23	23	23	12
24	L2	24	12	12	25
25	N1	25	24	24	13
NC	NC	NC	26	NC	NC

Table B.3: Electrical mapping of DC quadrant 2 (White). CPGA pads (Pad) are mapped from the CPGA pin (Pin) and PCB headers (Board) through the 26-pin (26-pin) and Fischer connector (Fischer) to the room side D-sub 25 (DB25) connector. Socket pin 38 is grounded. NC = not connected.

Pad	Pin	Board	26-pin	Fischer	DB25
26	M2	26	13	13	1
27	N2	27	1	1	14
28	M3	28	14	14	2
29	N3	29	2	2	15
30	M4	30	15	15	3
31	N4	31	3	3	16
32	M5	32	16	16	4
33	N5	33	4	4	17
34	L6	34	17	17	5
35	M6	35	5	5	18
36	N6	36	18	18	6
37	M7	37	6	6	19
38	L7	38	NC	NC	7
39	N7	39	7	7	20
40	N8	40	19	19	8
41	M8	41	8	8	21
42	L8	42	20	20	9
43	N9	43	9	9	22
44	M9	44	21	21	10
45	N10	45	10	10	23
46	M10	46	22	22	11
47	N11	47	11	11	24
48	N12	48	23	23	12
49	M11	49	12	12	25
50	N13	50	24	24	13
NC	NC	NC	26	NC	NC

Table B.4: Electrical mapping of DC quadrant 3 (Blue). CPGA pads (Pad) are mapped from the CPGA pin (Pin) and PCB headers (Board) through the 26-pin (26-pin) and Fischer connector (Fischer) to the room side D-sub 25 (DB25) connector. Socket pin 63 is grounded. NC = not connected.

Pad	Pin	Board	26-pin	Fischer	DB25
51	M12	51	13	13	1
52	M13	52	1	1	14
53	L12	53	14	14	2
54	L13	54	2	2	15
55	K12	55	15	15	3
56	K13	56	3	3	16
57	J12	57	16	16	4
58	J13	58	4	4	17
59	H11	59	17	17	5
60	H12	60	5	5	18
61	H13	61	18	18	6
62	G12	62	6	6	19
63	G11	63	NC	NC	7
64	G13	64	7	7	20
65	F13	65	19	19	8
66	F12	66	8	8	21
67	F11	67	20	20	9
68	E13	68	9	9	22
69	E12	69	21	21	10
70	D13	70	10	10	23
71	D12	71	22	22	11
72	C13	72	11	11	24
73	B13	73	23	23	12
74	C12	74	12	12	25
75	A13	75	24	24	13
NC	NC	NC	26	NC	NC

Table B.5: Electrical mapping of DC quadrant 4 (Red). CPGA pads (Pad) are mapped from the CPGA pin (Pin) and PCB headers (Board) through the 26-pin (26-pin) and Fischer connector (Fischer) to the room side D-sub 25 (DB25) connector. Socket pin 88 is grounded. NC = not connected.

Pad	Pin	Board	26-pin	Fischer	DB25
76	B12	76	13	13	1
77	A12	77	1	1	14
78	B11	78	14	14	2
79	A11	79	2	2	15
80	B10	80	15	15	3
81	A10	81	3	3	16
82	B9	82	16	16	4
83	A9	83	4	4	17
84	C8	84	17	17	5
85	B8	85	5	5	18
86	A8	86	18	18	6
87	B7	87	6	6	19
88	C7	88	NC	NC	7
89	A7	89	7	7	20
90	A6	90	19	19	8
91	B6	91	8	8	21
92	C6	92	20	20	9
93	A5	93	9	9	22
94	B5	94	21	21	10
95	A4	95	10	10	23
96	B4	96	22	22	11
97	A3	97	11	11	24
98	A2	98	23	23	12
99	B3	99	12	12	25
100	A1	100	24	24	13
NC	NC	NC	26	NC	NC

B.2 Thermometry + Misc Electrical Connections

A similar multi-part scheme is used for the electrical connections of the thermometry, heaters, the neutral oven source, and various miscellaneous accessories. There are two wire bundles labeled 1 and 2 which each begin with a room temperature D-sub 25 to Fischer cable (Fig. B.4 and B.5). The room temperature section then interfaces via a Fischer connection to a 300 K section (Figs. B.6 and B.7) that is in vacuum. The 40 K section consists of a D-sub 25 connector on one end and a number of small 2- and 4-pin connectors for various devices (Fig. B.8 and B.9) on the other. The final 4 K section has been eschewed. Currently, thermometry readout is performed by an 8-channel Lakeshore Model 218 temperature monitor and each wire bundle supports four thermometers. The thermometers are measured via a four-wire configuration and the connectors are typically wired symmetrically to avoid connector polarity issues. Note that pin 20 on thermometry + misc 2 is disconnected within the 40 K section.

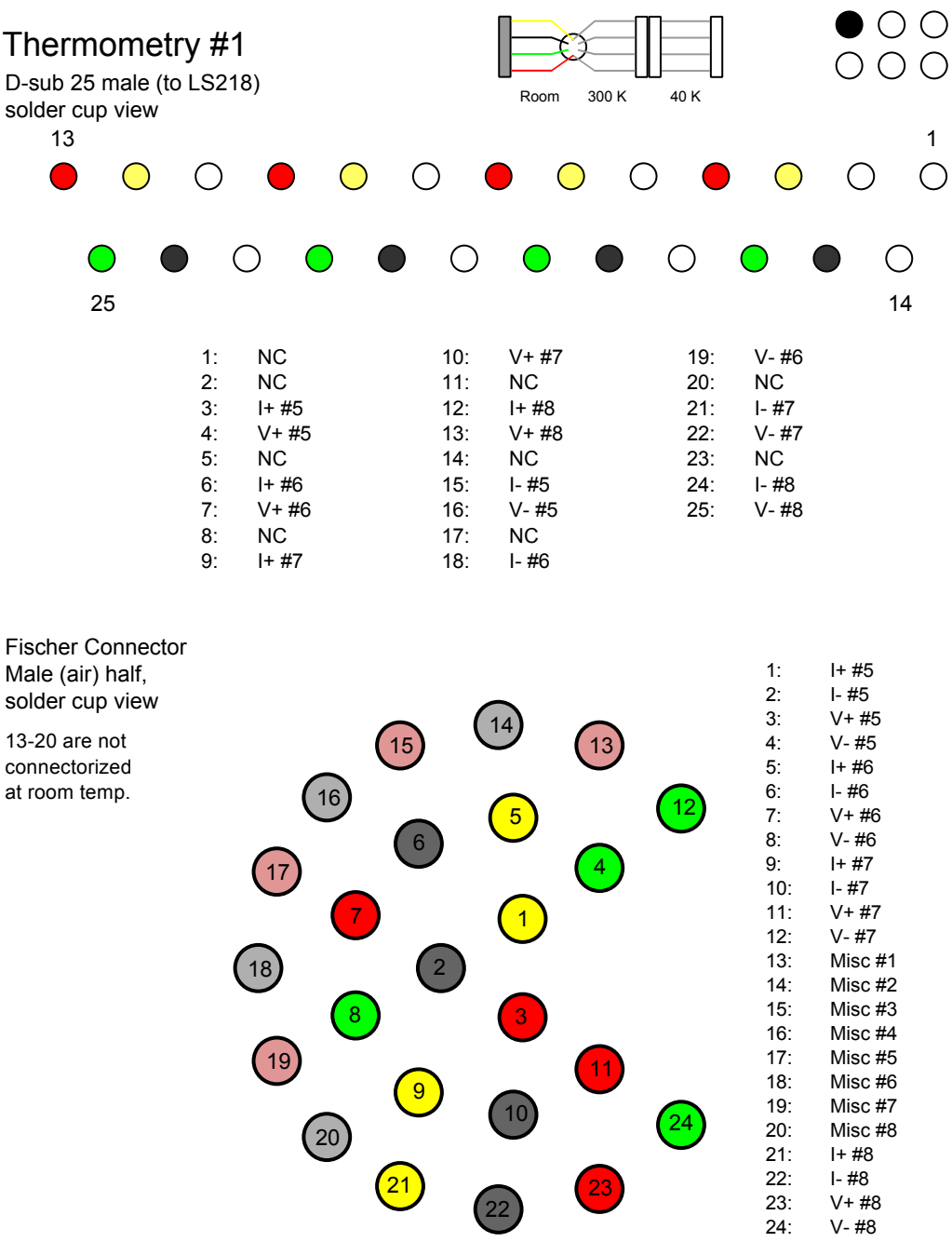

Figure B.4: Electrical mapping for thermometry + misc 1 - room temperature. The D-sub 25 is labeled according to the Lakeshore Model 218 temperature monitor's inputs. Misc connections are for future use. Pin color represents the color of the insulation used on the wires for pins 1-12 and 21-24.

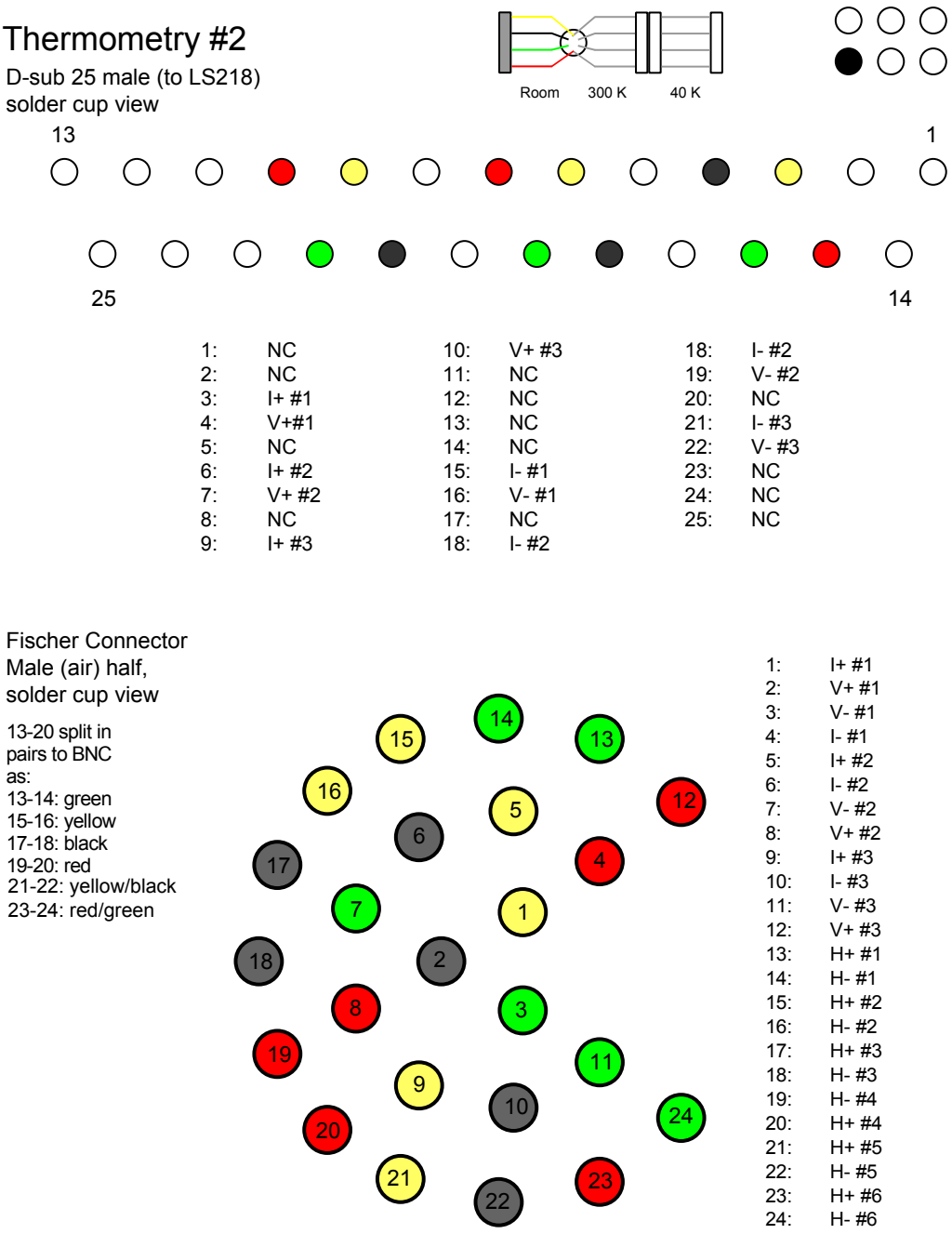

Figure B.5: Electrical mapping for thermometry + misc 2 - room temperature. The I and V connections correspond to the Lakeshore Model 218 temperature monitor's inputs. Connections labeled with an H represents heater and oven connections; though polarity is unimportant for these connections, it is labeled for future reference. Pin color corresponds to the wire insulation color.

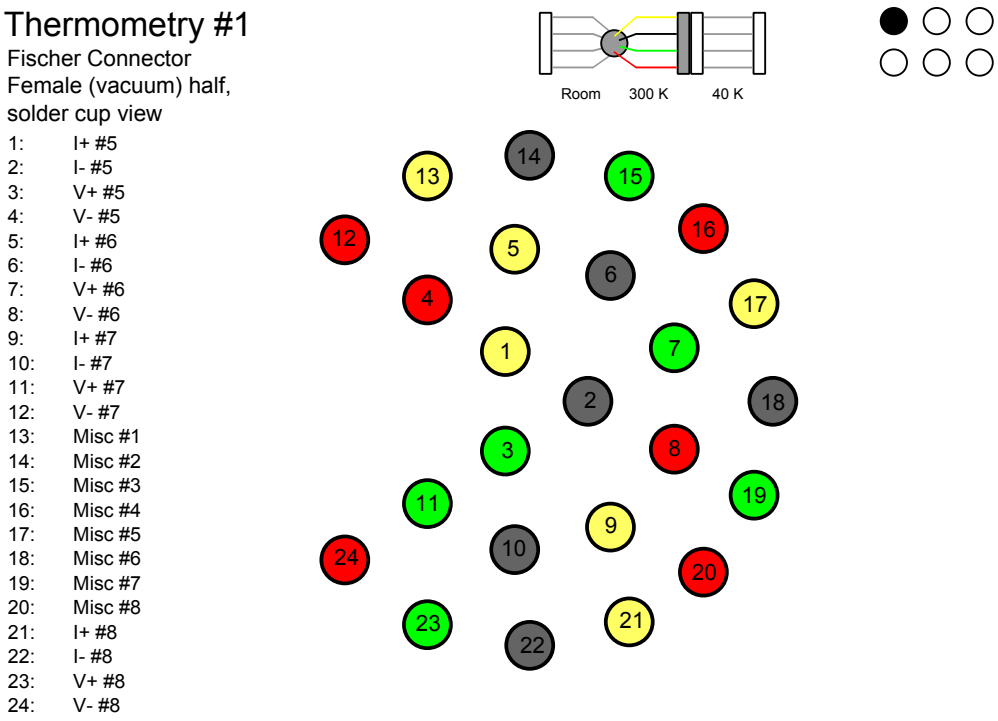

Pinout:
1-24: 32 AWG quad-twist phosphor-bronze

1:	I+ #5	9:	I+ #7	17:	Misc #5	25:	NC
2:	I- #5	10:	I- #7	18:	Misc #6	26:	NC
3:	V+ #5	11:	V+ #7	19:	Misc #7		
4:	V- #5	12:	V- #7	20:	Misc #8		
5:	I+ #6	13:	Misc #1	21:	I+ #8		
6:	I- #6	14:	Misc #2	22:	I- #8		
7:	V+ #6	15:	Misc #3	23:	V+ #8		
8:	V- #6	16:	Misc #4	24:	V- #8		

Figure B.6: Electrical mapping for thermometry + misc 1 - 300 K. Pin color represents the color of the Lakeshore quad-twist phosphor-bronze wire used.

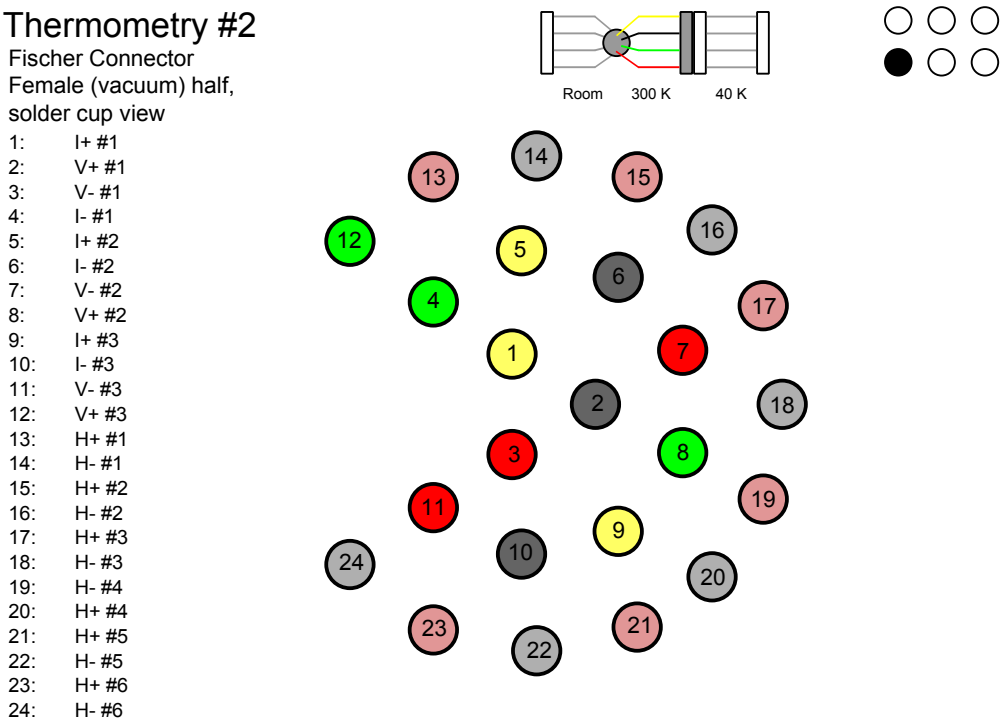

Figure B.7: Electrical mapping for thermometry + misc 2 - 300 K. Pin color represents the color of the Lakeshore quad-twist phosphor-bronze wire used for pins 1-12 and 21-24. Pink and grey pins are connected via copper magnet wire with clear insulation.

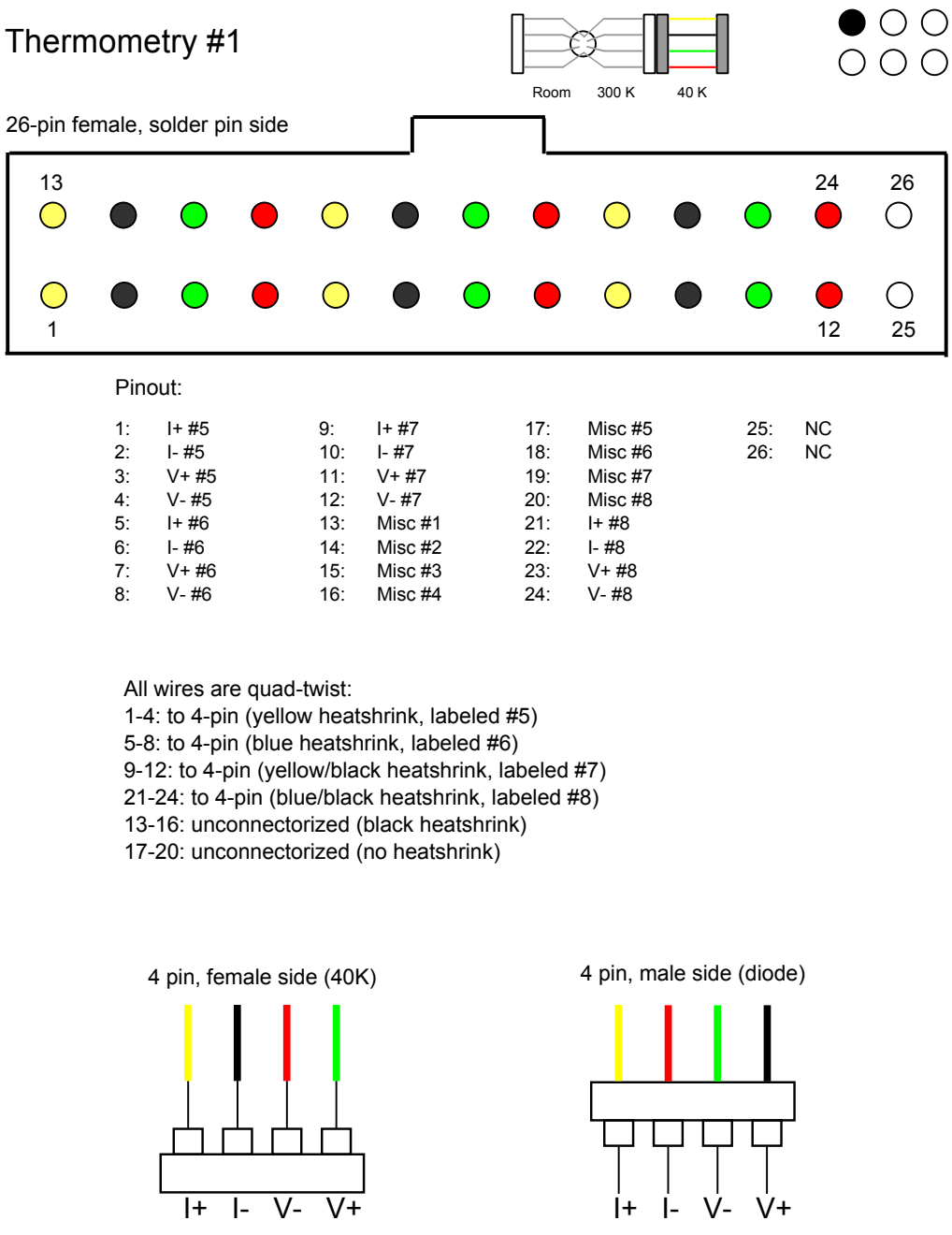

Figure B.8: Electrical mapping for thermometry + misc 1 - 40 K. Pin color represents the color of the Lakeshore quad-twist phosphor-bronze wire used.

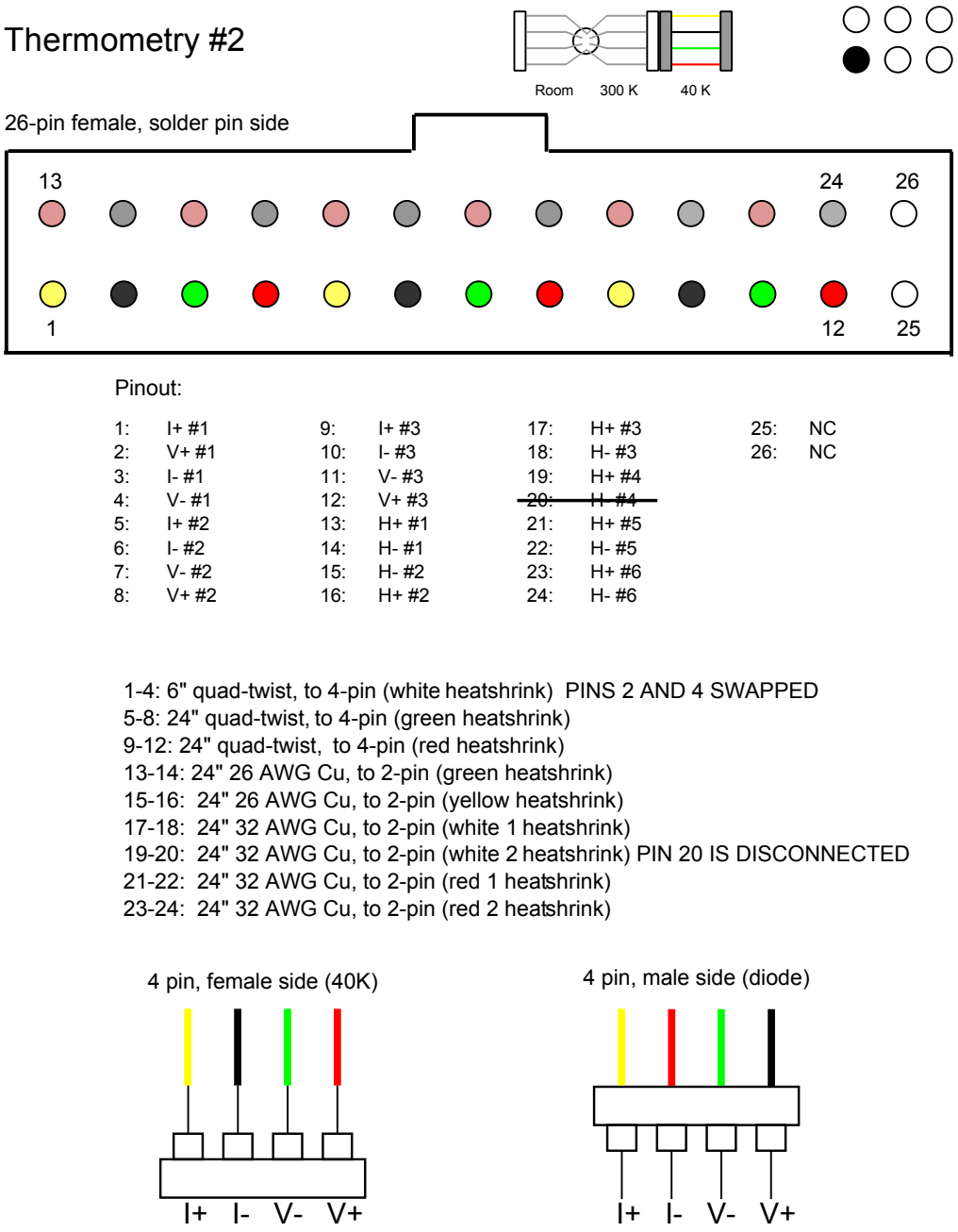

Figure B.9: Electrical mapping for thermometry + misc 2 - 40 K. Pin color represents the color of the Lakeshore quad-twist phosphor-bronze wire used. Pink and grey pins are connected via copper magnet wire with clear insulation. Note that pin 20 is damaged at the 26-pin connector.

APPENDIX C

CRYOHEAD MOTION TRIGGER CIRCUIT

In order to trigger both the CCD camera and experimental protocols on the cold-head motion, a motion triggering circuit was developed (Fig. C.1). This circuit includes a full-bridge strain gage, readout electronics, and three signal outputs: "Instr Amp Out", "Fast Trigger", and "Slow Trigger". The strain gage circuit is attached to a cantilever which maintains contact with the remote motor-cryocooler helium flex line. The motion of the cantilever due to the periodic pulsing of compressed helium through the system generates a voltage signal across the full-bridge strain gage circuit, $\Delta V = \Delta V_+ - \Delta V_-$, where ΔV_+ goes to the positive input of an instrumentation amplifier and ΔV_- goes to the negative input. This low noise signal is available at the circuit output "Instr Amp Out". It also continues to a Schmitt trigger which is typically calibrated to generate $+12\ V$ when at the top, flattest portion of the cantilever signal and no signal otherwise. This Schmitt trigger signal is used as the Gate voltage for an N-channel MOSFET. This first MOSFET generates a $+5\ V$ "Slow Trigger" signal that is typically used for triggering of the CCD camera and experiments. A 2 kHz, $+5\ V$ signal is generated by a relaxation oscillator. Through a series of three additional MOSFETs, this "Fast Trigger" output is only provided when the "Slow Trigger" signal is $+5\ V$. Note that $R8$ goes to the front panel and does not follow the convention of Table C.2.

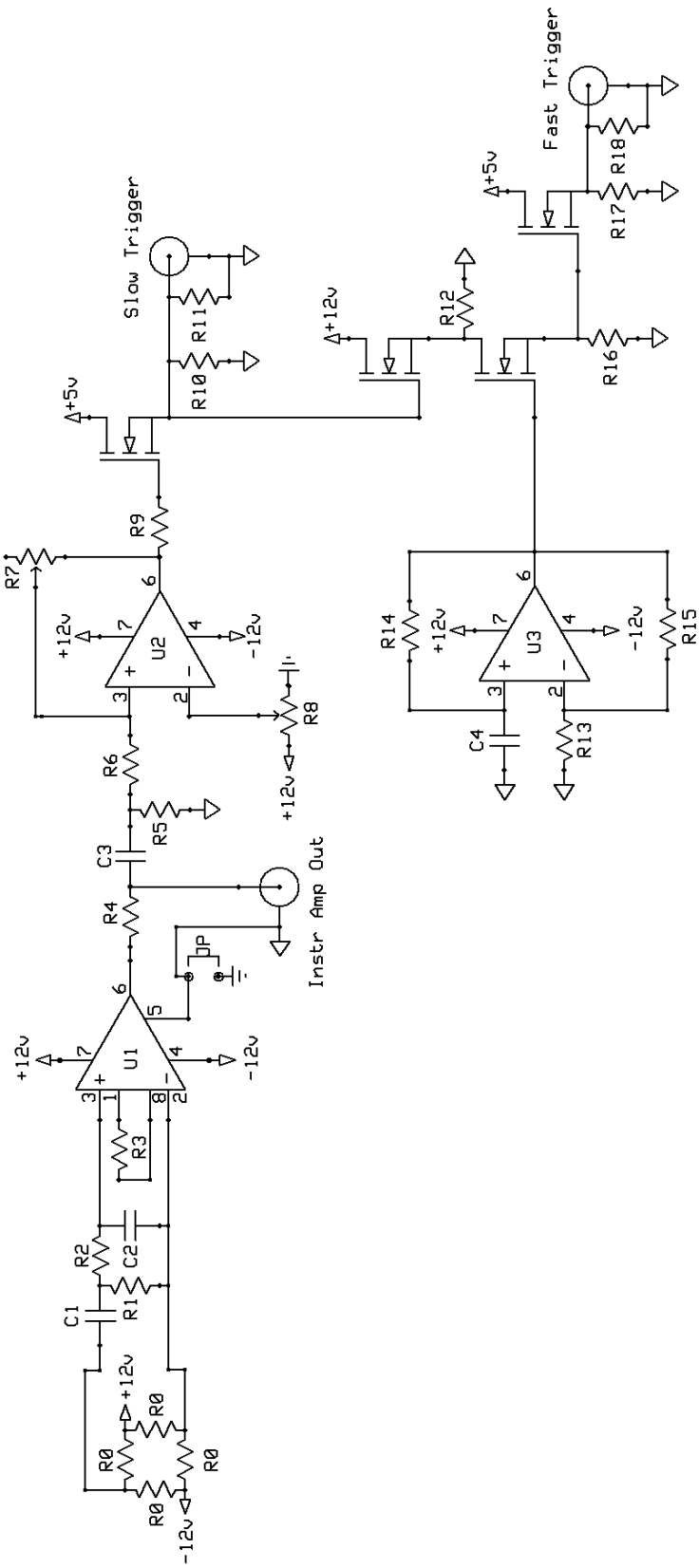

Figure C.1: Cryohead motion trigger circuit diagram.

Table C.1: Cryohead motion trigger circuit components. In the description column, devices are parenthetically labeled by their package type. Passive thru hole devices are labeled by TH.

Part #	Description	Label
Vishay Precision		
CEA-06-125UW-350	350 Ω strain gage	$R0$
Analog Devices AD620	Instrumentation amp (SOIC-8)	$U1$
Analog Devices OP07	Op amp (DIP8)	$U2, U3$
-	470 kΩ (TH)	$R1, R5, R13$
-	220 kΩ (TH)	$R2$
-	499 Ω (0805)	$R3$
-	200 kΩ (2010)	$R4$
-	1 kΩ (TH)	$R6, R9, R10, R12, R16, R17$
-	100 kΩ potentiometer	$R7$
-	20 kΩ potentiometer	$R8$
-	220 Ω (TH)	$R11, R18$
-	10 kΩ (TH)	$R13, R15$
-	10 μF (TH)	$C1, C3$
-	1 nF (TH)	$C2, C4$
Elpac WM063-1950	6.3 W 5V/12V/-12V PSU	-

Table C.2: Cryohead motion trigger wire colors. This table is useful for tracing the signal paths of the implemented circuit.

Wire color	Signal
Red	+5V,+12V
Black	-12V
Green	PSU COM
Blue	ΔV_+
White	ΔV_- (before U_1), Signal GND (after U_1)
Yellow	Slow trigger
Orange	Fast trigger

APPENDIX D

EXPERIMENTAL REALITIES

D.1 Vibrational and Thermal Properties of the Cryostat

Though the current cryogenic system has satisfactory vibrational and thermal properties, they are still far from ideal. The problem of the vibration isolation stage motion can be addressed with varying degrees of severity. The simplest approach is to break the mechanical connection between the G10 rods and the cryohead's room temperature flange. The G10 rods would then be attached directly to the aluminum mounting plate that sits on the top of the super structure. This approach is difficult to manifest as there is limited space within the OVC to introduce new mounting pieces for the G10 rods. Additionally, the cryohead would still be rigidly attached to the mounting plate and capable of transmitting vibrations into the superstructure and thus the OVC. Vibration measurements taken at the height of the ion trap by attaching a razor blade to the top OVC suggest that such vibrations would be minimal. The G10 rods could also be anchored to an adapter plate between two portions of the OVC; however, this would disturb the careful alignment of OVC interfaces with the cryocooler stages and the plates would have to be thin with narrow ledges to mount the rods to. Such a geometry suggests the adapter plates might lack the necessary stiffness to minimize vibrations.

If a more thorough refit is desired, the cryohead could be mechanically divorced from the superstructure while the vibration isolation system could be anchored to the aluminum mounting plate. In order to decouple the cryohead, it would be mounted to the strut channel "cloud" above the cryostat or the ceiling and a vibration reducing steel and rubber bellows assembly would be used as the interface between the superstructure's aluminum mounting plate and the cryohead. The vibration isolation platform would still be in direct contact with the mounting plate but the motion of the vibration isolation stage and cryohead would be significantly decoupled. This approach is problematic as it would require the cold-head

to be raised several inches, again disturbing the careful alignment between OVC interfaces and cryocooler stages. Additionally, the new position of the first stage would complicate the current heatsinking for the electrical connections and require careful consideration of how to properly modify the heat shield to maintain its functionality.

The most severe modification would be to replace the current vibration isolation system with a helium gas heat exchanger. Such a conversion would most likely require a considerable redesign of the current vacuum and electrical system, would increase the complexity of the system, and reduce the cooling power. However, it would provide a greatly reduced vibration amplitude; in Ref. [50], they report a <106 nm maximum displacement of their vibration isolation stage. Since the helium exchange gas can condense above the vibration isolation stage when the cryocooler power exceeds the heat load, it also provides an amount of thermal capacitance to help delay temperature fluctuations upon the introduction of new heat sources. This property is especially useful in an oven loaded system where the power radiated by the energized oven may temporarily outstrip the cooling power of the system. Due to the considerable modification of the cryostat that would be necessary, designing a new system centered around the helium gas heat exchanger would be more wise.

D.2 Thermally Dependent Loading Performance

Generally, the copper spacer block, PCB, and socket are maintained at 3.15, 4.10, and 6.88 K with $V_{rf} = 96\ V$. When the oven is energized, these temperatures rise due to the heat load on the components that are thermally anchored to the cryocooler's second stage. If the oven is energized for a sufficient amount of time that the socket temperature rises to 9 K, Doppler cooled chain stability is noticeably affected. Ions are presumably lost due to collisions with particles desorbing from nearby surfaces. When the socket temperature reaches 10 K, single ion loading becomes difficult, the oven must be turned off, and the second stage allowed to recool. For single ion experiments, this behavior is rarely problematic. However, it can be a hindrance when attempting to build long chains or when trying to load a surface-electrode trap for the first time. The most appropriate longterm solution for this would be to utilize a neutral source with a lower thermal load such as an ablation plume.

During the experiments of Chapter 4, regularly building $N = 5, 6$ chains was difficult as the increased loading time caused the socket temperature to rise significantly. The increased socket temperature compromised the Doppler cooled chain lifetime, causing loss of ions during the oven cooldown period prior to experimentation. This behavior may have been exacerbated by the relatively high Mathieu $q = 0.266$ used in these experiments to ensure fast single-ion loading. In order to minimize single-ion loading times and maximize chain survivability, q should be modulated as necessary. A high q is necessary to minimize load times during single-ion loading and chain building. However, reducing q will enhance chain survivability during oven cooldown and chain experiments. Such a system could be implemented by adjusting the RF drive voltage via the experimental computer. The voltage variable attenuator prior to the RF amplifier would serve this purpose.

D.3 Cryosorption of Contaminants onto the 50 K laser Windows

The excellent cryopumping of the system also has a disadvantage. As all surfaces attached to the cryocooler's first stage and the heat shield are at 50 K, they will all serve as cryopumps including the laser and fluorescence windows. During the chain lifetime experiments, these windows became sufficiently coated by adsorbates after a month that thin-film interference patterns could be observed. After $\sim$3 months, the windows had become further coated and small dark spots began to form on the adsorbate layers where the 397 nm and photoionization lasers passed through. As these spots did not form away from the laser, it seems likely that photon-activated chemistry or transport and further concentration of adsorbates took place. Over a seven month period, the ion fluorescence detected by the PMT deteriorated from 75 photons/ms with an ion-to-background ratio of 60 to 10 photons/ms with an ion-to-background ratio of 2 for the same 397 nm laser power and detuning. The photoionization laser power necessary for ion loading also increased.

This necessitated the opening of the cryostat and cleaning of all windows following the chain lifetime experiments. Though many of the adsorbates evaporated once the cryocooler was deactivated and the system reached room temperature, a non-uniform, semi-opaque film was left on the inner faces of the inner laser windows. In order to remove this film,

cleaning with isopropyl alcohol was required; neither cleaning with methanol nor acetone was sufficient to remove the initial material. When the windows were removed, excess Apiezon N thermal grease was found at the interface between the heat shield corner rods and the heat shield sides. The grease was especially prevalent at the height of the windows. As the vapor pressure of Apiezon N increases and the grease becomes much more fluid when heated, the windows may have received a light coating of grease during the sorb bake. This layer may have amplified adsorption during cooldown. No film of any kind was found on the fluorescence collection windows. After cleaning the windows, the trap was reinstalled and the system cooled to cryogenic temperatures. Following cleaning of the windows, the ion counts for the same 397 nm laser power had increased to 42 photons/ms with an ion-to-background ratio of 25 despite not carefully aligning the fluorescence lens stack to the ion to maximize collected fluorescence.

In the future, it may be possible to remove contaminants from the windows by allowing the cryocooler to return to room temperature without directly cleaning the windows or opening the OVC. If the cryosorbed contaminants consist of atmospheric gas species, they should desorb upon warming. As the ion trap will be undisturbed, laser alignment following the subsequent cooldown should be simple. If this method is not sufficient, the installation of thin film heating elements on the heat shield windows may be. Such heating elements would allow *in-situ* heating of the windows at cryogenic temperatures in an attempt to thermally desorb contaminants.

REFERENCES

[1] B. P. Lanyon, C. Hempel, D. Nigg, M. Müller, R. Gerritsma, F. Zähringer, P. Schindler, J. T. Barreiro, M. Rambach, G. Kirchmair, et al., "Universal Digital Quantum Simulation with Trapped Ions," *Science* **334**, 57 (2011).

[2] J. Chiaverini, R. B. Blakestad, J. Britton, J. D. Jost, C. Langer, D. Leibfried, R. Ozeri, and D. J. Wineland, "Surface-electrode architecture for ion-trap quantum information processing," *Quantum Inf. Comput.* **5**, 419 (2005).

[3] M. E. Poitzsch, J. C. Bergquist, W. M. Itano, and D. J. Wineland, "Cryogenic linear ion trap for accurate spectroscopy," *Rev. Sci. Instrum.* **67**, 129 (1996).

[4] L. Deslauriers, S. Olmschenk, D. Stick, W. K. Hensinger, J. Sterk, and C. Monroe, "Scaling and suppression of anomalous heating in ion traps," *Phys. Rev. Lett.* **97**, 103007 (2006).

[5] W. Paul, "Electromagnetic traps for charged and neutral particles," *Rev. Mod. Phys.* **62**, 531 (1990).

[6] W. Paul and H. Steinwedel, "Ein neues Massenspektrometer ohne Magnetfeld," *Z. Naturforsch. A* **8**, 448 (1953).

[7] R. E. March, "Quadrupole ion trap mass spectrometry: a view at the turn of the century," *Int. J. Mass Spectrom.* **200**, 285 (2000).

[8] D. J. Douglas, "Linear quadrupoles in mass spectrometry," *Mass Spectrom. Rev.* **28**, 937 (2009).

[9] R. F. Wuerker, H. Shelton, and R. V. Langmuir, "Electrodynamic Containment of Charged Particles," *J. Appl. Phys.* **30**, 441 (1959).

[10] D. J. Wineland, R. E. Drullinger, and F. L. Walls, "Radiation-Pressure Cooling of Bound Resonant Absorbers," *Phys. Rev. Lett.* **40**, 1639 (1978).

[11] G. B. Andresen, M. D. Ashkezari, M. Baquero-Ruiz, W. Bertsche, P. D. Bowe, E. Butler, C. L. Cesar, S. Chapman, M. Charlton, A. Deller, et al., "Trapped antihydrogen," *Nature* **468**, 673 (2010).

[12] J. W. Britton, B. C. Sawyer, A. C. Keith, C.-C. J. Wang, J. K. Freericks, H. Uys, M. J. Biercuk, and J. J. Bollinger, "Engineered two-dimensional Ising interactions in a trapped-ion quantum simulator with hundreds of spins," *Nature* **484**, 489 (2012).

[13] F. Diedrich, J. C. Bergquist, W. M. Itano, and D. J. Wineland, "Laser cooling to the Zero-Point Energy of Motion," *Phys. Rev. Lett.* **62**, 403 (1989).

[14] J. D. Prestage, G. J. Dick, and L. Maleki, "New ion trap for frequency standard applications," *J. Appl. Phys.* **66**, 1013 (1989).

[15] R. P. Feynman, "Simulating Physics with Computers," *Int. J. Theor. Phys.* **21**, 467 (1982).

[16] P. W. Shor, "Algorithms for quantum computation: discrete log and factoring," in *Proceedings of the 35th Annual Symposium on the Foundations of Computer Science* (IEEE Computer Society Press, 1994), pp. 124–134.

[17] J. I. Cirac and P. Zoller, "Quantum Computations with Cold Trapped Ions," *Phys. Rev. Lett.* **74**, 4091 (1995).

[18] D. Hanneke, J. P. Home, J. D. Jost, J. M. Amini, D. Leibfried, and D. J. Wineland, "Realization of a programmable two-qubit quantum processor," *Nature Phys.* **6**, 13 (2010).

[19] R. Islam, C. Senko, W. C. Campbell, S. Korenblit, J. Smith, A. Lee, E. E. Edwards, C.-C. J. Wang, J. K. Freericks, and C. Monroe, "Emergence and Frustration of Magnetic Order with Variable-Range Interactions in a Trapped Ion Quantum Simulator," *Science* **340**, 583 (2013).

[20] P. Maunz, S. Olmschenk, D. Hayes, D. N. Matsukevich, L.-M. Duan, and C. Monroe, "A Heralded Quantum Gate Between Remote Quantum Memories," *Phys. Rev. Lett.* **102**, 250502 (2009).

[21] T. Rosenband, D. B. Hume, P. O. Schmidt, C. W. Chou, A. Brusch, L. Lorini, W. H. Oskay, R. E. Drullinger, T. M. Fortier, J. E. Stainaker, et al., "Frequency Ratio of Al^+ and Hg^+ Single-Ion Optical Clocks; Metrology at the 17^{th} Decimal Place," *Science* **319**, 1808 (2008).

[22] T. Monz, P. Schindler, J. T. Barreiro, M. Chwalla, D. Nigg, W. A. Coish, M. Harlander, W. Hänsel, M. Hennrich, and R. Blatt, "14-qubit Entanglement: Creation and Coherence," *Phys. Rev. Lett.* **106**, 130506 (2011).

[23] V. Batteiger, S. Knünz, M. Herrmann, G. Saathoff, H. A. Schüssler, B. Bernhardt, T. Wilken, R. Holzwarth, T. W. Hänsch, and T. Udem, "Precision spectroscopy of the 3s-3p fine-structure doublet in Mg^+," *Phys. Rev. A* (2009).

[24] A. L. Wolf, J. Morgenweg, J. C. J. Koelemeij, S. A. van den Berg, W. Ubachs, and K. S. E. Eikema, "Direct Frequency Comb Spectroscopy of Trapped Ions," *Phys. Rev. Lett.* **102**, 223901 (2009).

[25] R. E. Drullinger, D. J. Wineland, and J. C. Bergquist, "High-resolution Optical Spectra of Laser Cooled Ions," *Appl. Phys.* **22**, 365 (1980).

[26] D. J. Larson, J. C. Bergquist, J. J. Bollinger, W. M. Itano, and D. J. Wineland, "Sympathetic Cooling of Trapped Ions: A Laser-Cooled Two-Species Nonneutral Ion Plasma," *Phys. Rev. Lett.* **57**, 70 (1986).

[27] T. Baba and I. Waki, "Cooling and Mass-Analysis of Molecules Using Laser-Cooled Atoms," *Jpn. J. Appl. Phys.* **35**, L1134 (1996).

[28] B. Roth, R. Blythe, H. Daerr, L. Patacchini, and S. Schiller, "Production of ultracold diatomic and triatomic molecular ions of spectroscopic and astrophysical interest," *J. Phys. B* **39**, S1241 (2006).

[29] S. Willitsch, M. T. Bell, A. D. Gingell, S. R. Procter, and T. P. Softley, "Cold reactive collision between laser-cooled ions and velocity-selected neutral molecules," *Phys. Rev. Lett.* **100**, 043203 (2008).

[30] P. F. Staanum, K. Hoejbjerre, R. Wester, and M. Drewsen, "Probing isotope effects in chemical reactions using single ions," *Phys. Rev. Lett.* **100**, 243003 (2008).

[31] S. Schiller and V. Korobov, "Tests of time independence of the electron and nuclear masses with ultracold molecules," *Phys. Rev. A* **71**, 032505 (2005).

[32] P. O. Schmidt, T. Rosenband, C. Langer, W. M. Itano, J. C. Bergquist, and D. J. Wineland, "Spectroscopy using quantum logic," *Science* **309**, 749 (2005).

[33] T. Rosenband, P. O. Schmidt, D. B. Hume, W. M. Itano, T. M. Fortier, J. E. Stalnaker, K. Kim, S. A. Diddams, J. C. J. Koelemeij, J. C. Bergqist, et al., "Observation of the $^1S_0 \rightarrow ^3P_0$ clock transition in $^{27}Al^+$," *Phys. Rev. Lett.* **98**, 220801 (2007).

[34] M. A. Nielsen and I. L. Chuang, *Quantum Computation and Quantum Information* (Cambridge University Press, 2000).

[35] C. Monroe and J. Kim, "Scaling the Ion Trap Quantum Processor," *Science* **339**, 1164 (2013).

[36] D. Kielpinski, C. Monroe, and D. J. Wineland, "Architecture for a large-scale ion-trap quantum computer," *Nature* **417**, 709 (2002).

[37] D. L. Moehring, P. Maunz, S. Olmschenk, K. C. Younge, D. N. Matsukevich, L.-M. Duan, and C. Monroe, "Entanglement of single-atom quantum bits at a distance," *Nature* **449**, 68 (2007).

[38] R. B. Blakestad, C. Ospelkaus, A. P. VanDevender, J. M. Amini, J. Britton, D. Leibfried, and D. J. Wineland, "High fidelity transport of trapped-ion qubits through an X-junction trap array," *Phys. Rev. Lett.* **102**, 153002 (2009).

[39] S. C. Doret, J. M. Amini, K. Wright, C. Volin, T. Killian, A. Ozakin, D. Denison, H. Hayden, C.-S. Pai, R. E. Slusher, et al., "Controlling trapping potentials and stray electric fields in a microfabricated ion trap through design and compensation," *New J. Phys.* **14**, 073012 (2012).

[40] W. K. Hensinger, S. Olmschenk, D. Stick, D. Hucul, M. Yeo, M. Acton, L. Deslauriers, C. Monroe, and J. Rabchuk, "T-junction ion trap array for two-dimensional ion shuttling, storage, and manipulation," *Appl. Phys. Lett.* **88**, 034101 (2006).

[41] K. Wright, J. M. Amini, D. L. Faircloth, C. Volin, S. C. Doret, H. Hayden, C.-S. Pai, D. W. Landgren, D. Denison, T. Killian, et al., "Reliable transport through a microfabricated X-junction surface-electrode ion trap," *New J. Phys.* **15**, 033004 (2013).

[42] J. H. Wesenberg, "Electrostatics of surface-electrode ion traps," *Phys. Rev. A* **78**, 063410 (2008).

[43] Q. A. Turchette, D. Kielpinski, B. E. King, D. Leibfried, D. M. Meekhof, C. J. Myatt, M. A. Rowe, C. A. Sackett, C. S. Wood, W. M. Itano, et al., "Heating of trapped ions from the quantum ground state," *Phys. Rev. A* **61**, 063418 (2000).

[44] D. J. Wineland, C. Monroe, W. M. Itano, D. Leibfried, B. E. King, and D. M. Meekhof, "Experimental Issues in Coherent Quantum-State Manipulation of Trapped Atomic Ions," *J. Res. Natl. Inst. Stand. Technol.* **103**, 259 (1998).

[45] D. T. C. Allcock, J. A. Sherman, D. N. Stacey, A. H. Burrell, M. J. Curtis, G. Imreh, N. M. Linke, D. J. Szwer, S. C. Webster, A. M. Steane, et al., "Implementation of a symmetric surface-electrode ion trap with field compensation using a modulated raman effect," *New J. Phys.* **12**, 053026 (2010).

[46] D. A. Hite, Y. Colombe, A. C. Wilson, K. R. Brown, U. Warring, R. Jördens, J. D. Jost, D. P. Pappas, D. Leibfried, and D. J. Wineland, "Reduction of anomalous heating in an *in-situ*-cleaned ion trap," *Phys. Rev. Lett.* **109**, 103001 (2012).

[47] J. Labaziewicz, Y. Ge, P. Antohi, D. Leibrandt, K. R. Brown, and I. L. Chuang, "Suppression of heating rates in cryogenic surface-electrode ion traps," *Phys. Rev. Lett.* **100**, 013001 (2008).

[48] G. Vittorini, K. Wright, K. R. Brown, A. W. Harter, and S. C. Doret, "Modular cryostat for ion trapping with surface-electrode ion traps," *Rev. Sci. Instrum.* **84**, 043112 (2013).

[49] K. Okada, M. Wada, T. Nakamura, I. Katayama, L. Boesten, and S. Ohtani, "Cryogenic Ion Trap for Minimization of Trapped Ion Loss," *Jpn. J. Appl. Phys.* **40**, 4221 (2001).

[50] P. B. Antohi, D. Schuster, G. M. Akselrod, J. Labaziewicz, Y. Ge, Z. Lin, W. S. Bakr, and I. L. Chuang, "Cryogenic ion trapping systems with surface-electrode traps," *Rev. Sci. Instrum.* **80**, 013103 (2009).

[51] K. R. Brown, C. Ospelkaus, Y. Colombe, A. C. Wilson, D. Leibfried, and D. J. Wineland, "Coupled quantized mechanical oscillators," *Nature* **471**, 196 (2011).

[52] J. M. Sage, A. J. Kerman, and J. Chiaverini, "Loading of a surface-electrode ion trap from a remote, precooled source," *Phys. Rev. A* **86**, 013417 (2012).

[53] D. Gandolfi, M. Niedermayr, M. Kumph, M. Brownnutt, and R. Blatt, "Compact radio-frequency resonator for cryogenic ion traps," *Rev. Sci. Instrum.* **83**, 084705 (2012).

[54] M. Schwarz, O. O. Versolato, A. Windberger, F. R. Brunner, T. Ballance, S. N. Eberle, J. Ullrich, P. O. Schmidt, A. K. Hansen, A. D. Gingell, et al., "Cryogenic linear Paul trap for cold highly charged ion experiments," *Rev. Sci. Instrum.* **83**, 083115 (2012).

[55] F. Pobell, *Matter and Methods at Low Temperatures* (Springer, 2007).

[56] Kenton R. Brown, private communication (2012).

[57] S. Charles Doret, private communication (2013).

[58] A. T. A. M. de Waele, "Basic Operation of Cryocoolers and Related Thermal Machines," *J. Low Temp. Phys.* **164**, 179 (2011).

[59] J. D. Siverns, L. R. Simkins, S. Weidt, and W. K. Hensinger, "On the application of radio frequency voltages to ion traps via helical resonators," *Appl. Phys. B* **107**, 921 (2012).

[60] R. G. DeVoe and C. Kurtsiefer, "Experimental study of anomalous heating and trap instabilities in a microscopic ^{137}Ba ion trap," *Phys. Rev. A* **65**, 063407 (2002).

[61] D. M. Lucas, A. Ramos, J. P. Home, M. J. McDonnell, S. Nakayama, J.-P. Stacey, S. C. Webster, D. N. Stacey, and A. M. Steane, "Isotope-selective photoionization for calcium ion trapping," *Phys. Rev. A* **69**, 012711 (2004).

[62] R. J. Hendricks, D. M. Grant, P. F. Herskind, A. Dantan, and M. Drewsen, "An all-optical ion-loading technique for scalable microtrap architectures," *Appl. Phys. B* **88**, 507 (2007).

[63] D. Leibfried, R. Blatt, C. Monroe, and D. Wineland, "Quantum dynamics of single trapped ions," *Rev. Mod. Phys.* **75**, 282 (2003).

[64] H. Häffner, C. F. Roos, and R. Blatt, "Quantum computing with trapped ions," *Physics Reports* **469**, 155 (2008).

[65] P. K. Ghosh, *Ion Traps* (Oxford University Press, 1995).

[66] R. J. Glauber, in *Laser Manipulation of Atoms and Ions*, edited by W. D. P. E. Arimondo and F. Strumia (Elsevier, 1993).

[67] Gen II ion traps: Trap overview, (2011), `http://quantum.gatech.edu/images/content/GTRI_GenII_Overview.pdf`.

[68] H. J. Metcalf and P. van der Straten, *Laser Cooling and Trapping* (Springer, 1999).

[69] J. Eschner, G. Morigi, F. Schmidt-Kaler, and R. Blatt, "Laser cooling of trapped ions," *J. Opt. Soc. Am. B* **20**, 1003 (2004).

[70] J. E. Goeders, Ph.D. thesis, Georgia Institute of Technology (2013).

[71] W. Nagourney, J. Sandberg, and H. Dehmelt, "Shelved Optical Electron Amplifier: Observation of Quantum Jumps," *Phys. Rev. Lett.* **56**, 2797 (1986).

[72] E. Peik, J. Abel, T. Becker, J. von Zanthier, and H. Walter, "Sideband cooling of ions in radio-frequency traps," *Phys. Rev. A* **60**, 439 (1999).

[73] S. C. Doret, "Transfer Cavity / Stabilized HeNe based Laser Frequency Stabilization," (2011), `http://quantum.gatech.edu/images/content/HeNe_transfer_cavity_lock.pdf`.

[74] E. D. Black, "An introduction to Pound-Drever-Hall laser frequency stabilization," *Am. J. Phys.* **69**, 79 (2001).

[75] G. Vidali, G. Ihm, Y.-J. Kim, and M. W. Cole, "Potentials of physical adsorption," *Surf. Sci. Rep.* **12**, 133 (1991).

[76] Cryomech, Inc., private communication (2012).

[77] Y. Ibaraki, U. Tanaka, and S. Urabe, "Detection of parametric resonance of trapped ions for micromotion compensation," *Appl. Phys. B* **105**, 219 (2011).

[78] S. Narayanan, N. Daniilidis, S. A. Möller, R. Clark, F. Ziesel, K. Singer, F. Schmidt-Kaler, and H. Häffner, "Electric field compensation and sensing with a single ion in a planar trap," *J. Appl. Phys.* **110**, 114909 (2011).

[79] M. Harlander, , M. Brownnutt, W. Hänsel, and R. Blatt, "Trapped-ion probing of light-induced charging effects on dielectrics," *New J. Phys.* **12**, 093035 (2010).

[80] S. X. Wang, G. H. Low, N. S. Lachenmyer, Y. Ge, P. F. Herskind, and I. L. Chuang, "Laser-induced charging of microfabricated ion traps," *J. Appl. Phys.* **110**, 104901 (2011).

[81] R. J. Epstein, S. Seidelin, D. Leibfried, J. H. Wesenberg, J. J. Bollinger, J. M. Amini, R. B. Blakestad, J. Britton, J. P. Home, W. M. Itano, et al., "Simplified motional heating rate measurements of trapped ions," *Phys. Rev. A* **76**, 033411 (2007).

[82] C. Roos, T. Zeiger, H. Rohde, H. C. Naegerl, J. Eschner, D. Leibfried, F. Schmidt-Kaler, and R. Blatt, "Quantum State Engineering on an Optical Transition and Decoherence in a Paul Trap," *Phys. Rev. Lett.* **83**, 4713 (1999).

[83] D. Hucul, M. Yeo, W. K. Hensinger, J. Rabchuk, S. Olmschenk, and C. Monroe, "On the transport of atomic ions in linear and multidimensional ion trap arrays," *Quantum Inf. Comput.* **8** (2008).

[84] A. Walther, F. Ziesel, T. Ruster, S. T. Dawkins, K. Ott, M. Hettrich, K. Singer, F. Schmidt-Kaler, and U. Poschinger, "Controlling Fast Transport of Cold Trapped Ions," *Phys. Rev. Lett.* **109**, 080501 (2012).

[85] R. Bowler, J. Gaebler, Y. Lin, T. R. Tan, D. Hanneke, J. D. Jost, J. P. Home, D. Leibfried, and D. J. Wineland, "Coherent Diabatic Ion Transport and Separation in a Multizone Trap Array," **109**, 080502 (2012).

[86] F. Splatt, M. Harlander, M. Brownnutt, F. Zähringer, R. Blatt, and W. Hänsel, "Deterministic reordering of $^{40}Ca^{+}$ in a linear segmented paul trap," *New J. Phys.* **11**, 103008 (2009).

[87] J. P. Home and A. M. Steane, "Electrode Configurations for Fast Separation of Trapped Ions," *Quantum Inf. Comput.* **6**, 289 (2006).

[88] N. Yu, W. Nagourney, and H. Dehmelt, "Demonstration of new Paul-Straubel trap for trapping single ions," *J. Appl. Phys.* **69**, 3779 (1991).

[89] K. Chen, S. T. Sullivan, W. G. Rellergert, and E. R. Hudson, "Measurement of the Coulomb Logarithm in a Radio-Frequency Paul trap," *Phys. Rev. Lett.* **110**, 173003 (2013).

[90] D. H. E. Dubin and T. M. O'Neil, "Trapped nonneutral plasmas, liquids, and crystals (the thermal equilibrium states)," *Rev. Mod. Phys.* **71**, 87 (1999).

[91] R. Blümel, J. M. Chen, E. Peik, W. Quint, W. Schleich, Y. R. Shen, and H. Walther, "Phase transitions of store laser-cooled ions," *Nature* **334**, 309 (1988).

[92] A. Drakoudis, M. Söllner, and G. Werth, "Instabilities of ion motion in a linear Paul trap," *Int. J. Mass Spectrom.* **252**, 61 (2006).

[93] D. J. Wineland, C. Monroe, W. M. Itano, B. E. King, D. Leibfried, D. M. Meekhof, C. Myatt, and C. Wood, "Experimental Primer on the Trapped Ion Quantum Computer," *Fortschr. Phys.* **46**, 363 (1998).

[94] E. R. Hudson, "Method for producing ultracold molecular ions," *Phys. Rev. A* **79**, 032716 (2009).

[95] R. Georgiadis and P. B. Armentrout, "Kinetic Energy Dependence of the Reactions of Ca^+ and Zn^+ with H_2, D_2, and HD: Effect of Empty versus Full d Orbitals," *J. Phys. Chem.* **92**, 7060 (1988).

[96] E. R. Fisher, J. L. Elkind, D. E. Clemmer, R. Georgiadis, S. K. Loh, N. Aristov, L. S. Sunderlin, and P. B. Armentrout, "Reactions of fourth-period metal cions (Ca^+-Zn^+) with O_2: Metal-oxide ion bond energies," *J. Chem. Phys.* **93**, 2676 (1990).

[97] E. Murad, "Abstraction reactions of Ca^+ and Sr^+ ions," *J. Chem. Phys.* **78**, 6611 (1983).

[98] F. G. Major and H. G. Dehmelt, "Exchange-Collision Technique for the rf Spectroscopy of Stored Ions," *Phys. Rev.* **170** (1968).

[99] Y. Moriwaki, M. Tachikawa, Y. Maeno, and T. Shimizu, "Collision Cooling of Ions Stored in Quadrupole Radio-Frequency Trap," *Jpn. J. Appl. Phys.* **31**, L1640 (1992).

[100] H. Schaaf, U. Schmeling, and G. Werth, "Trapped Ion Density Distribution in the Presence of He-Buffer Gas," *Appl. Phys.* **25**, 249 (1981).

[101] D. F. V. James, "Quantum dynamics of cold trapped ions with application to quantum computation," *Appl. Phys. B* **66**, 181 (1998).

[102] Jason Amini, private communication (2013).

[103] E. S. Meyer, I. F. Silvera, and B. L. Brandt, "Eddy current shielding and heating: Reduction of dissipation for very low-temperature experiments in the presence of magnetic field ripple," *Rev. Sci. Instrum.* **60**, 2964 (1989).

[104] J. T. Merrill, S. C. Doret, G. Vittorini, J. P. Addison, A. W. Harter, and K. R. Brown, "Optimized composite-sequence ion addressing in a surface-electrode ion trap," *In preparation* (2013).

[105] K. R. Brown, A. C. Wilson, Y. Colombe, C. Ospelkaus, A. M. Meier, E. Knill, D. Leibfried, and D. J. Wineland, "Single-qubit-gate error below 10^{-4} in a trapped ion," *Phys. Rev. A* **84**, 030303 (2011).

[106] S. X. Wang, J. Labaziewiez, Y. Ge, R. Shewmon, and I. L. Chuang, "Demonstration of a quantum logic gate in a cryogenic surface-electrode ion trap," *Phys. Rev. A* **81**, 062332 (2010).

[107] N. Deb, B. R. Heazlewood, M. T. Bell, and T. P. Softley, "Blackbody-mediated rotational laser cooling schemes in MgH^+, DCl^+, HCl^+, LiH and CsH," *Phys. Chem. Chem. Phys.* **15**, 14270 (2013).

[108] I. Vogelius, L. B. Madsen, and M. Drewsen, "Blackbody-Radiation-Assisted Laser Cooling of Molecular Ions," *Phys. Rev. Lett.* **89**, 173003 (2002).

[109] P. F. Staanum, K. Hoejbjerre, P. S. Skyt, A. K. Hansen, and M. Drewsen, "Rotational laser cooling of vibrationally and translationally cold molecular ions," *Nature Phys.* **6**, 271 (2010).

[110] T. Schneider, B. Roth, H. Duncker, I. Ernsting, and S. Schiller, "All-optical preparation of molecular ions in the rovibrational ground state," *Nature Phys.* **6**, 275 (2010).

[111] J. H. V. Nguyen, C. R. Viteri, E. G. Hohenstein, C. D. Sherrill, K. R. Brown, and B. Odom, "Challenges of laser-cooling molecular ions," *New. J. Phys.* **13**, 063023 (2011).

[112] D. Leibfried, "Quatum state preparation and control of single molecular ions," *New. J. Phys.* **14**, 023029 (2012).

[113] S. Ding and D. N. Matsukevich, "Quantum logic for control and manipulation of molecular ions using a frequency comb," *New J. Phys.* **14**, 023028 (2012).